Technische Universität München
Fluiddynamik komplexer Biosysteme

Modeling of semidilute entangled polymer solutions and numerical simulation of industrially relevant benchmark flows to study shear banding

Soroush Hooshyar

Vollständiger Abdruck der von der Fakultät Wissenschaftszentrum Weihenstephan für Ernährung, Landnutzung und Umwelt der Technischen Universität München zur Erlangung des akademischen Grades eines Doktors -Ingenieurs (Dr.-Ing.) genehmigten Dissertation.

Vorsitzender:	Prof. Dr.-Ing. Heiko Briesen
Prüfer der Dissertation:	1. Prof. Dr. Natalie Germann
	2. Prof. Dr.-Ing. Nikolaus A. Adams

Die Dissertation wurde am 04.06.2019 bei der Technischen Universität München eingereicht und durch die Fakultät Wissenschaftszentrum Weihenstephan für Ernährung, Landnutzung und Umwelt am 21.01.2020 angenommen.

Acknowledgements

I am thankful for how everything has been set that I stand where I am now. I hope all the people in my life know that I always have them in my heart, and I could show more appreciation if there were no limitations, like time. I can here express my gratitude only to who that directly helped me to continue the journey of this thesis.

When I came for the interview of this Ph.D. position, I was thinking on the campus whether I will become a member of TUM. When my supervisor called me and informed me that I am accepted, I realized that one of my biggest dreams is becoming true. The work was not clear for me in the beginning; she helped me a lot, particularly in the publication of our first and second papers. Her discipline was the most significant contribution. I cannot remember any day that she was not available. Professor Germann, I am grateful for all you have done for me.

I would like to express my gratitude to the members of the Fluid Dynamics of Complex Biosystems group. Special thank goes to Dr. Thomas Goudoulas, who supported me from the first day I attended the group. Furthermore, I want to thank Dr. Mohammadali Masoudian, who helped me a lot, especially in the simulations of the third paper.

I want to thank the language center of TUM, especially Ross Clark and Jeremiah Hendren. I participated in some of their English writing classes. Hopefully, their help has made this manuscript readable.

I am thankful to the people of Munich especially those who provided me a proper condition to concentrate on my path.

I want to thank my friends who have always understood my situation and always tried to encourage me.

I want to thank my father, mother, brother, and sister. Whatever I do, it is not enough to compensate what they have been going through that I fulfill my dreams. I can only dedicate this thesis to them.

Abstract

Non-Newtonian fluids can develop banded velocity and concentration profiles under strong shear deformations, which is known as shear banding. Although shear banding is a ubiquitous phenomenon observed in many soft materials such as polymer solutions and wormlike micelles, the mechanisms that induce it are not always the same. To study shear banding in semidilute entangled polymer solutions, we have developed a new thermodynamically consistent two-fluid model using the generalized bracket approach of non-equilibrium thermodynamics.

The two-fluid approach is an appropriate means for describing diffusional processes, such as Fickian diffusion and stress-induced migration. It is assumed in this framework that the local gradients in concentration and viscoelastic stress generate a nontrivial difference between the velocities of the constituents of the solution, which allows the phases to diffuse at different speeds.

The two-fluid system that we used consists of one component of polymeric constituents and a viscous solvent. Within the model, a Giesekus-type relaxation was added to the conformation tensor equation to describe the conformational dynamics of the polymers and to obtain an overshoot of the shear stress during the start-up of a simple shear flow, which triggers the formation of the shear bands. In addition, we included a second nonlinear relaxation term to capture the upturn of the flow curve of shear stress versus shear rate at high shear rates. This term is a non-equilibrium thermodynamic reformulation of the term used in the Rolie-Poly model that accounts for convective constraint release and includes chain stretch. Furthermore, a nonlocal stress-diffusive term was added to the time evolution equation of the polymer conformation to generate smooth and unique steady-state profiles. The advantage of our model is that the formulation of boundary conditions such as slip, no-slip, and those arising from the diffusive derivative terms are straightforward since the differential velocity is a state variable in our model. Due to the diffusional processes, the profile of the polymer number density is not uniform in our model. Furthermore, the model predicts the nonlinear rheological behavior without the need for a substantial solvent contribution.

We analyzed the model behavior in a cylindrical Couette flow, a Poiseuille channel flow, a 4:1 contraction flow, and a die swell flow. We also implemented the wall slip boundary condition in our two-fluid framework using the linear Navier slip model. The Couette and the Poiseuille flows are solved using a standard Chebyshev pseudospectral collocation method, and the calculations of the contraction and the die swell flows are done using the OpenFOAM finite volume package.

The results of the calculations confirm that the stress-induced migration is responsible for the shear band formation

in our model. We observed that the steady-state solution is unique with respect to the initial conditions, applied deformation history, and the value of the local diffusivity constant appearing in the time evolution equation for the differential velocity. However, the smaller the local diffusivity constant is, the longer it takes to reach the steady state. Interestingly, the value of the nonlocal diffusivity constant does not significantly affect the transient dynamics. The profile of the total velocity of the Poiseuille flow in the shear banding regime deviates from the typical parabolic diagram and forms a plug-like pattern, with a low shear rate band near the center and a high shear rate band near the walls. We observed a spurt in the profile of the flow rate at a critical value of the pressure gradient, which is in agreement with the experimental data of pressure-driven shear flows of entangled polymer solutions. Our model is a good candidate for simulations of industrial flows due to its simplicity and the results. For instance, we show how to control the extrusion instabilities of die swell flows, which depending on the application can be desired or not.

Zusammenfassung

Nicht-Newtonsche Fluide können unter starken Scherdeformationen bänderartige Geschwindigkeits- und Konzentrationsprofile ausbilden. Obwohl die Ausbildung von Scherbändern allgemein in vielen weichen Materialien wie beispielsweise Polymerlösungen und wurmartigen Mizellen auftritt, unterscheiden sich die hierfür verantwortlichen Mechanismen. Um die Scherbänder in halb-verdünnten, verschlauften Polymerlösungen genauer zu betrachten wurde ein neues thermodynamisch konsistentes Zwei-Fluid-Model entwickelt, welches auf einem verallgemeinerten, nicht-gleichgewichtsthermodynamischen Klamemransatz basiert.

Der Zwei-Fluid-Ansatz ist ein probates Mittel, um Diffusionsprozesse wie die Ficksche Diffusion und spannungsinduzierte Migration zu beschreiben. Bei dieser Theorie wird genommen, dass die lokalen Gradienten der Konzentration und der viskoelastischen Spannung eine nicht-triviale Differenz zwischen den Geschwindigkeiten der Lösungsbestandteilen generieren, was den Phasen eine Diffusion mit unterschiedlichen Geschwindigkeiten ermöglicht.

Das hier verwendete Zwei-Fluid System beinhaltet eine Spezies mit polymeren Bestandteilen und ein viskoses Lösungsmittel. Innerhalb des Modells wurde der Konformationstensorgleichung eine Giesekus-artige Relaxation hinzugefügt, um die Konformationsdynamik der Polymere zu beschreiben und eine Übersteigerung der Scherspannung zu Beginn der einfachen Scherströmung zu erhalten, was die Ausbildung von Scherbändern bewirkt. Zusätzlich wurde ein zweiter nicht-linearer Relaxationsterm einbezogen, welcher den Aufschwung der Strömungskurve im Scherspannung-Scherraten-Plot bei hohen Scherraten erfasst. Dieser Term ist eine nichtgleichgewichtsthermodynamische Reformulierung des im Rolie-Poly Modell benutzten Terms, welcher die convective-constraint-release und chain-stretch beinhaltet. Weiterhin wurde dem zeitlichen Evolutionsgleichung ein nicht-lokaler Spannungs-Diffusions-Term hinzugefügt, der ein gleichmäßiges und einzigartiges Gleichgewichtsprofil generiert. Der Vorteil den dieses Modell bringt, ist die eindeutige Formulierung der Randbedingungen wie slip, no-slip bzgl. der abgeleiteten Randbedingungen der Diffusionstermen, da hier die differentielle Geschwindigkeit eine Zustandsgröße ist. Das Profil der Polymeranzahldichte ist nicht uniform in unserem Modell, aufgrund diffusiver Prozesse. Weiterhin prognostiziert das Modell ein nicht-lineares rheologisches Verhalten ohne der Notwendigkeit einer wesentlichen Einwirkung des Lösungsmittels.

Wir untersuchten das Modellverhalten in einer zylindrischen Couette-Strömung, einer Poiseuille-Kanalströmung, einer 4:1 Kontraktionsströmung und einer Die-swell Strömung. Außerdem wurde unter Verwendung des linearen

Navier slip Modells, eine wall-slip Randbedingung in die zwei-Fluid Modellstruktur implementiert. Die Couette und Poiseuille-Strömungen wurden mittels einer standard Chebyshev-pseudospectral-Kollocation-Methode gelöst und die Berechnung der Kontraktion und die-swell-Strömungen in OpenFOAM mit Hilfe des finiten Volumen Programmpaketes durchgeführt.

Die Ergebnisse der Berechnungen bestätigen, dass die spannungsinduzierte Migration verantwortlich für die Ausbildung der Scherbänder in unserem Modell ist. Es wurde beobachtet, dass die Gleichgewichtslösung einzigartig ist unter Berücksichtigung der Anfangsbedingungen, angewandten Deformationsgeschichte und den Wert der lokalen Diffusivitätskonstanten, welche in der zeitlichen Evolutionsgleichung der differentiellen Geschwindigkeit vorkommt. Trotzdem zeigt sich, dass, je kleiner die locale Diffusionskonstante ist, desto länger dauert es, einen Gleichgewichtszustand zu erreichen. Interessanterweise beeinflusst der Wert der nicht-lokalen Diffusionskonstante die transienten Dynamiken nicht signifikant. Das Profil der Gesamtgeschwindigkeit der Poiseuille Strömung weicht im Scherbandregime vom typischen parabolischen Diagramm ab und bildet eine pfropfenartige Struktur mit einem niedrigen Scherratenband in der Nähe des Zentrums und ein hohes Scherratenband nahe der Wände. Wir beobachteten einen rasenten Anstieg im Profil der Flussrate an einem kritischen Wert des Druckgradienten, welches in Übereinstimmung mit den experimentellen Daten der druckgetriebenen Scherströmung von verschlauften Polymerlösungen ist. Unser Modell ist eine gute Wahl für Simulationen von industriell relevanten Strömungen aufgrund seiner Vereinfachungen und der Resultate. Beispielsweise zeigten wir, wie Extrusionsinstabilitäten in Die-swell-Strömungen kontrolliert werden, welche anwendungsabhängig gewollt oder ungewollt sein können.

Contents

1 Introduction

Non-Newtonian fluids have non-constant viscosity depending on different variables, which is in contrast to the Newtonian fluids. The properties of some of the non-Newtonian materials are between solid state and liquid state as shown in Fig. 1; therefore, they are also called viscoelastic materials, complex fluids, or soft materials. Examples of these materials are polymer solutions, wormlike micellar solutions, and colloidal-like systems, or specifically, we can mention paint, shampoo, ketchup, blood, DNA solutions, toothpaste, dough, wet cement, crude oil, cosmetics, asphalt, and glue. The flow phenomena of viscoelastic materials are assessed under a branch of physics called rheology.

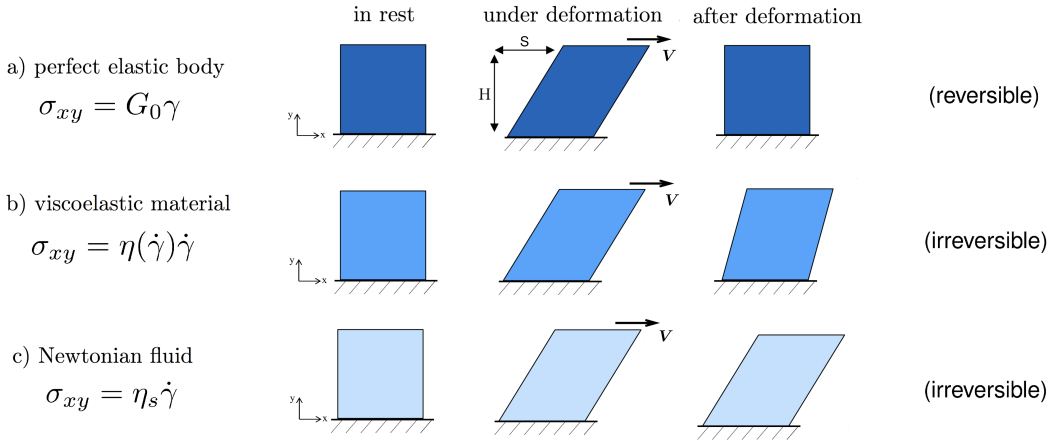

Figure 1: The deformation response of (a) perfect solid materials (e.g. rubber) described by the Hook's law $\sigma_{xy} = G_0\gamma$ with shear stress σ_{xy}, modulus of elasticity G_0, and strain $\gamma = S/H$ defined for small deformations as the ratio of the displacement S to the characteristic height H, (b) viscoelastic materials which are between solid and liquid states, and (c) Newtonian fluids (e.g. water) characterized by the Newton's law $\sigma_{xy} = \eta_s\dot{\gamma}$, with the constant viscosity η_s and shear rate defined as $\dot{\gamma} = \partial\gamma/\partial t = \partial \mathrm{v}_x/\partial y = \mathbf{V}/H$.

The viscoelastic properties may change with shear rate, time, pressure, and temperature due to the change in

the molecular structure of the material. Fig. 2 depicts the classification of materials according to the behavior of their viscosity with the applied shear rate. Newtonian fluids are characterized by constant viscosity, shear-thinning materials have viscosity that decreases with shear rate, and shear-thickening is the case in which the viscosity increases with shear rate.

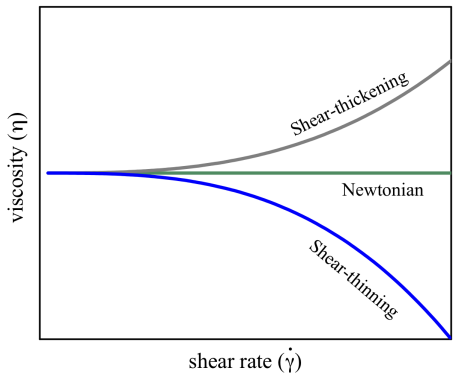

Figure 2: Different viscosity behaviors with shear rate.

Flow curve is a diagram that shows the relationship between shear stress σ_{xy} and shear rate $\dot{\gamma}$. This curve for semidilute polymer solutions, which show shear-thinning behavior, is linear for small and large shear rates, as shown in Fig. 3. The shear stress increases monotonically with the shear rate, where the slope depends on the molecular weight and the concentration of the polymer solution. To know the relationship between the shear stress and the shear rate, we need rheometric data or an equation describing this relationship. Such an equation is called constitutive model.

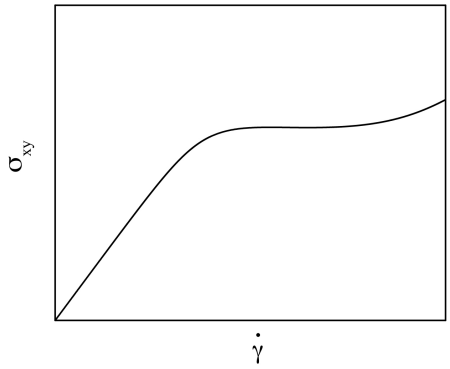

Figure 3: Representative flow curve of the shear stress versus the applied shear rate of a semidilute entangled polymer solution.

A simple shear flow is depicted in Fig. 4, where the lower plate is stationary and the upper one moves with a constant velocity $\boldsymbol{V}$. For small and large shear rates (Fig. 4(a)), the velocity increases linearly from zero at the bottom to the maximum at the top with slope equal to the applied shear rate $\dot{\gamma}$. In a flow like Fig. 4(b), the material responds with two shear rates $\dot{\gamma_1}$ and $\dot{\gamma_2}$; therefore, two linear velocity profiles are apparent. This phenomenon is called shear banding, and the linear velocity profiles are called shear bands. After entering the plateau-like shear-thinning regime of the flow curve, shear band formation can occur. The proportion of the flow from the higher band increases by increasing the shear rate until the homogeneous flow again covers the entire flow. In the literature, this type of shear banding that the bands are separated in the flow gradient direction is called shear/gradient banding or strain localization. In principal, more than two bands can be formed. This depends on flow geometry and deformation protocol. When different stresses coexist at an equal shear rate in the vorticity direction, the phenomenon is called vorticity banding, which is not of our interest in the current study. For more review of shear banding in soft materials, please refer to the literature (Fielding, 2007; Olmsted, 2008; Dhont and Briels, 2008; Manneville, 2008; Divoux et al., 2016; Germann, 2019). Shear banding has been observed in many soft materials such as colloidal-like systems, nematic liquid crystalline systems, wormlike micelles, semidilute entangled polymer solutions, and polymer melts. However, the mechanisms of shear banding for different materials are not always the same.

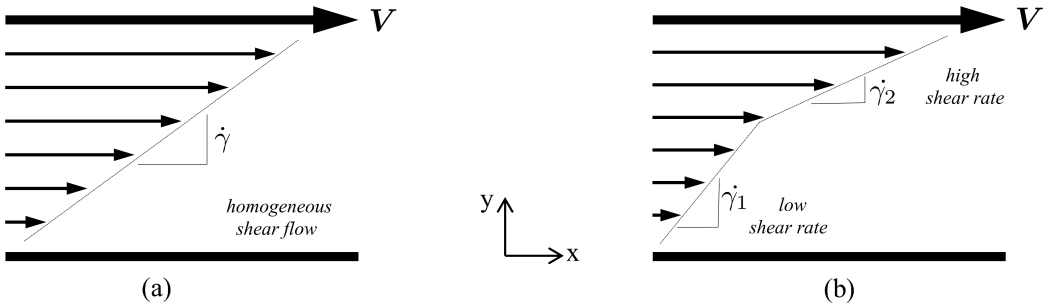

Figure 4: Velocity profile of a two-dimensional steady simple shear flow (a) under homogeneous flow conditions, and (b) in the presence of shear banding, where we note two bands of constant shear rates, with the high shear band located close to the moving wall.

Polymer solutions with thermodynamically good solvents are categorized in different concentration regimes suggested by De Gennes (1979) as dilute ($c < c^*$), semidilute ($c^* < c < c^{**}$), and concentrated ($c^{**} < c$). Here, the total concentration c denotes the ratio of the polymer weight to that of the solution. The concentrations c^* and c^{**} are respectively the overlap concentration and the crossover concentration from semidilute to concentrated regimes.

The overlap concentration is the case where the polymer molecules start to contact; i.e., the average distance between the molecules is in the order of the radius of gyration. These regimes are shown in Fig. 5. By increasing the concentration of the solutions, more intermolecular interactions occur and consequently the model to realistically describe the material should include more details. Shear banding occurs in the entangled regime (corresponding to the semidilute and the concentrated). It must be noted that the semidilute and concentrated regimes in Fig. 5 are assumed to be under shear which is the reason why the molecules are aligned with the flow. Our focus is on semidilute entangled polymer solutions, which have many applications such as nano-fiber production (Zettl et al., 2009), 3d printing (Schroeder, 2017), and fluid coating (De Ryck and Quéré, 1998).

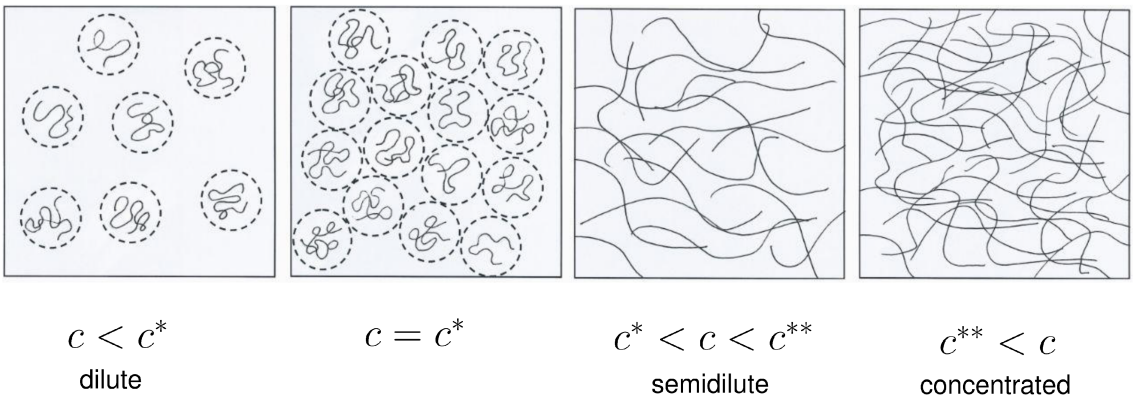

Figure 5: Different concentration regimes of polymer solutions. From left to right: dilute, at overlap, semidilute, and concentrated [modified from Bertola (2013), Fig. 2].

The macroscopic rheometric data are based on the bulk average information and ignore the structural characteristics; this leads to unreliable results in the presence of inhomogeneities like shear banding. Furthermore, experimental artifacts like edge fraction or methods to prevent it, alter the data (Li et al., 2013). Therefore, experiments need in-situ velocimetry techniques with higher resolution such as small angle neutron scattering (SANS) (Berret et al., 1994; Schmitt et al., 1994), nuclear magnetic resonance (NMR) (Mair and Callaghan, 1996; Britton and Callaghan, 1997; Callaghan and Gil, 2000), particle tracking velocimetry (PTV) (Hu and Lips, 2005; Wang et al., 2006), particle image velocimetry (PIV) (Goudoulas et al., 2017, 2018; Goudoulas and Germann, 2018), and optical coherence tomography (OCT) (Harvey and Waigh, 2011; Jaradat et al., 2012). Goudoulas and coworkers studied semidilute entangled polymer solutions of polyacrylamide (Goudoulas et al., 2017), DNA (Goudoulas et al., 2018), and polyethylene oxide (Goudoulas and Germann, 2018) using PIV and a setup

with reduced edge fraction. They observed that shear banding is independent of edge fraction and is a material property depending on the concentration and the molecular weight of the solution if the applied shear rate is sufficiently large. Their observation is in agreement with the phase diagram of Jaradat et al. (2012) shown in Fig. 6 obtained using OCT on concentrated solutions of high-molecular weight polyacrylamide solution at steady state. This phase diagram expresses that polymer solutions exhibit linear, shear banding, or wall slip behavior depending on their molecular weight and concentration. According to Jaradat et al. (2012), their data are reproducible and independent of the flow geometry used. However, such two-dimensional flow phases can only qualitatively help us to understand the impact of polymer concentration and molecular weight since other parameters such as the applied deformation rate and the geometry of the flow have significant impacts on the boundaries of these three regimes. Furthermore, Wang and coworkers confirmed that shear banding is a material property by PTV measurements of polybutadiene (Tapadia et al., 2006; Ravindranath and Wang, 2008b; Ravindranath et al., 2008; Boukany et al., 2015) and DNA (Boukany and Wang, 2009b). They have also proposed a phase diagram of the same three regimes, which is the function of shear rate and slip extrapolation length. Wang (2018) believes that the intermolecular connections of the polymer network starts to yield after a critical value of the deformation rate, which appears as wall slip.

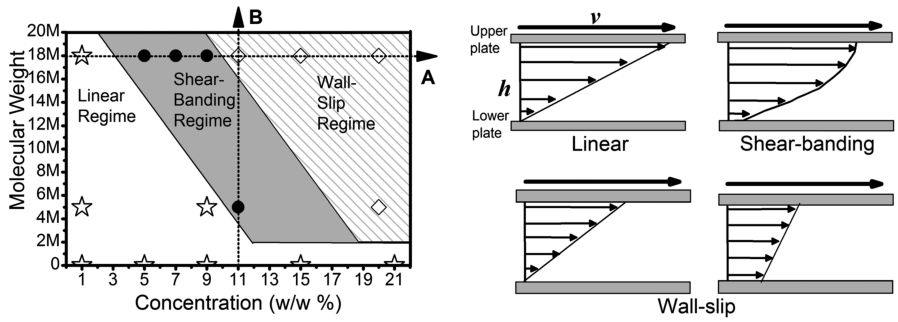

Figure 6: Phase diagram of concentrated high-molecular weight polyacrylamide solution with three distinct regimes: linear, shear banding, and wall slip [adopted from Jaradat et al. (2012), Fig. 6].

The goal of this thesis is to introduce a physically meaningful constitutive model that can describe shear banding in semidilute entangled polymer solutions. In addition, we numerically test the model in different industrially relevant flows shown in Fig. 7, namely a cylindrical Couette flow, a pressure-driven channel flow, a 4:1 contraction flow, and an extrusion flow. The derivation of the new model is explained in Sec. 2. We solve the model for the cylindrical Couette flow in Sec. 3. The solution of the pressure-driven channel flow is given in Sec. 4. The contraction flow is presented in Sec. 5. The extrusion flow is described in Sec. 6. And finally, Sec. 7 summarizes this thesis and discusses some possible improvements.

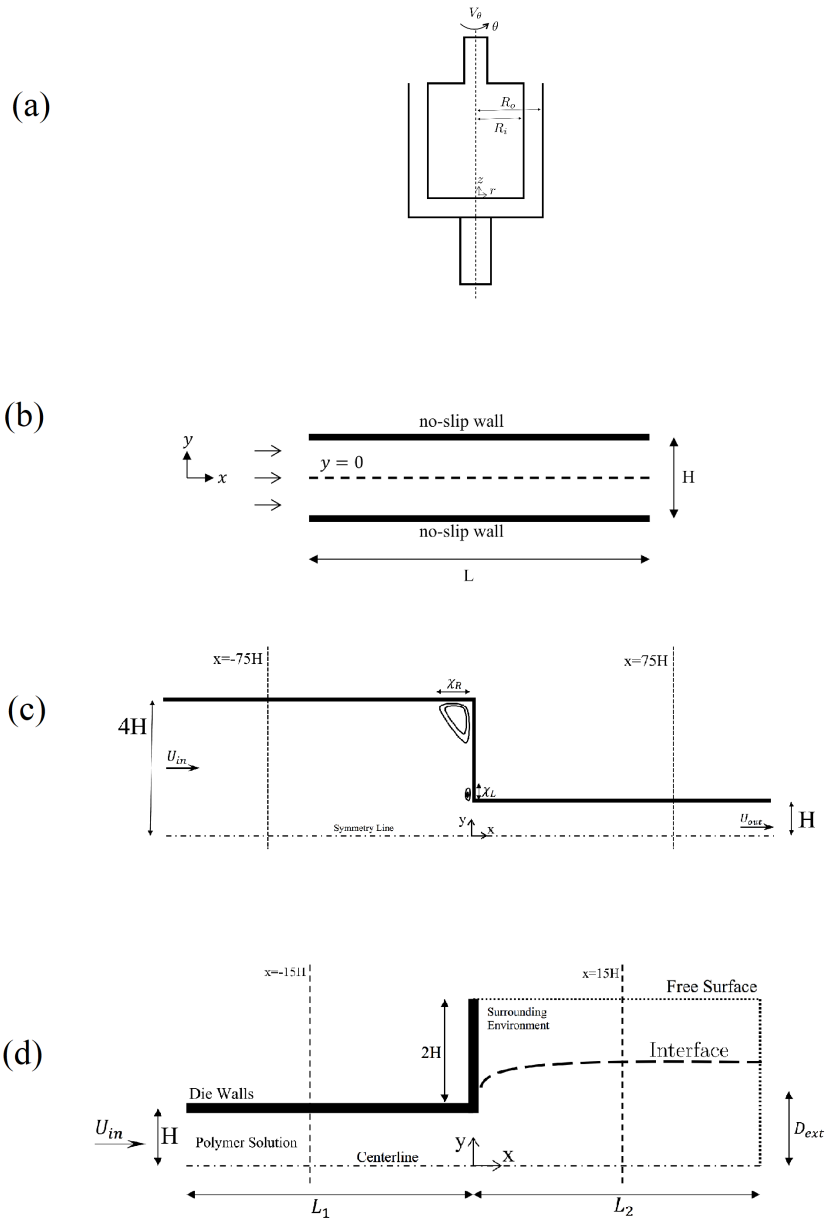

Figure 7: Schematic sketches of (a) the cylindrical Couette flow, (b) the rectilinear channel flow, (c) the 4:1 contraction flow, and (d) the extrusion flow.

2 Non-equilibrium thermodynamic polymer model

2.1 Background

The first step to model the behavior of the polymer solutions is to know their structure. Fig. 8 helps us to have an idea about the shape of linear polymer molecules in which we are interested, described by different levels of simplifications according to the desired features of the molecules. In general, the models should compromise between important physical properties and computational cost.

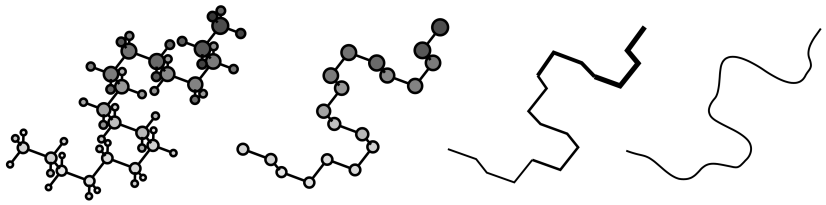

a atomistic model **b** main-chain atoms **c** bonds only **d** thread model

Figure 8: Simplification of chain conformation. (a) is the complete structure of the chain, (b) includes only the atoms on the backbone, (c) shows only the bonds between the atoms, and (d) is a smoothed line of thread representing the conformation [adopted from Teraoka (2002), Fig. 1.4].

Before introducing our model, it is worth going over the earlier constitutive models, especially those related to our model. A constitutive equation is needed to predict the relationship between shear stress and shear rate since this relationship for the shear rates higher than a critical value is not linear and not known for many of the viscoelastic fluids. The microscopic state of such fluids (polymer chains) does not respond instantaneously to an imposed deformation, which is a feature shared with purely elastic solids. This is observed as a delayed relaxation of the

stress. The equation of the momentum balance is as follows:

$$\rho \frac{\partial \mathbf{v}}{\partial t} = -\rho \mathbf{v} \cdot \boldsymbol{\nabla} \mathbf{v} - \boldsymbol{\nabla} p + \boldsymbol{\nabla} \cdot \boldsymbol{\sigma}. \tag{1}$$

Here, $\mathbf{v}$ denotes total velocity vector, ρ total mass density of the polymer solution, p pressure, t time, and $\boldsymbol{\sigma}$ the total stress that we need a constitutive equation to describe it. This relationship is the Newton's law if the material is a Newtonian (purely viscous) fluid:

$$\boldsymbol{\sigma} = 2\eta_s \boldsymbol{D}, \tag{2}$$

where $\boldsymbol{D} = \frac{1}{2}[\boldsymbol{\nabla} \mathbf{v} + (\boldsymbol{\nabla} \mathbf{v})^T]$ is the velocity gradient tensor equivalent to the symmetric part of the velocity gradient, and η_s is the viscosity of the fluid.

The scalar Maxwell model developed by *James Clerk Maxwell* (Maxwell, 1867) considers that each polymeric chain in Fig. 5 is a set of a damper and a spring connected in series similar to Fig. 9 to account for viscosity and elasticity, respectively. The spring represents the elastic polymer, which is denoted by letter p in the following, and the damper represents the viscous solvent, which is denoted by letter s in the following. We would obtain the Voigt model if the spring and the damper were connected in parallel. In the series configuration, the total stress equals the stress on the solvent and the stress on the polymer, and the total strain is the sum of the strains of the solvent and the polymer. Therefore, we can write $\sigma^{tot} = \sigma^s = \sigma^p = \sigma$ and $\gamma^{tot} = \gamma^s + \gamma^p$. After derivation with respect to time and by considering Newton's law $\sigma^s = \eta_s \dot{\gamma}^s$ and the Hook's law $\sigma^p = E\gamma^p \Rightarrow \dot{\sigma^p} = E\dot{\gamma^p}$, we derive $\dot{\gamma}^{tot} = \dot{\gamma}^s + \dot{\gamma}^p = \sigma^s/\eta_s + \dot{\sigma}^p/E \Rightarrow \eta_s \dot{\gamma}^{tot} = \sigma^s + \eta_s/E\ \dot{\sigma}^p = \sigma + \tau'\ \dot{\sigma}$. Here, the relaxation time is defined as $\tau' = \eta_s/E$, and $\dot{\sigma}$ denotes the time derivative of the stress. The scalar Maxwell model is given in Eq. (3).

$$\sigma + \tau' \dot{\sigma} = \eta_s \dot{\gamma}^{tot}. \tag{3}$$

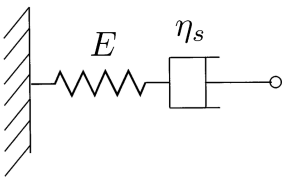

Figure 9: Schematic of the Maxwell model consisted of a damper with constant viscosity η_s and a spring with modulus of elasticity E connected in series.

Upper-convected Maxwell (UCM) model proposed by *James Gardner Oldroyd* in 1950 is the tensorial formulation of the Maxwell model. It obeys material objectivity and thus allows for three-dimensional flow analysis. It is considered in Oldroyd-B model that the total stress $\boldsymbol{\sigma} = \boldsymbol{\sigma}^s + \boldsymbol{\sigma}^p$ consists of solvent viscous stress $\boldsymbol{\sigma}^s$, and so-called extra stress $\boldsymbol{\sigma}^p$ which is the viscoelastic contribution of the polymer to the total stress. Furthermore, zero shear viscosity $\eta_0 = \eta_s + \eta_p$ is defined as the sum of the polymer viscosity η_p and the solvent viscosity η_s. The upper-convected time derivative is defined as Eq. (5) which describes the convected rate of change in time of a contravariant second-order tensor $\boldsymbol{\sigma}^p$. Eq. (4) gives the constitutive relation of the Oldroyd-B model. The Johnson-Segalman model would be derived by replacing the upper-convected derivative by the Gordon-Schowalter derivative (Gordon and Schowalter, 1972), which accounts for non-affine motion. The Oldroyd-B model reduces to the UCM model if there is no contribution from the solvent viscosity to the momentum Eq. (1); i.e. $\boldsymbol{\sigma}^s = 0$. The UCM model is only appropriate for small shear rates since it cannot predict shear-thinning and stress overshoot phenomena, and second normal stress difference is zero during start-up. These limitations are overcome by Giesekus model.

$$\boldsymbol{\sigma}^p + \tau' \overset{\nabla}{\boldsymbol{\sigma}}^p = 2\eta_p \boldsymbol{D}. \tag{4}$$

$$\overset{\nabla}{\boldsymbol{\sigma}}^p = \frac{\partial}{\partial t}\boldsymbol{\sigma}^p + \mathbf{v}\cdot\boldsymbol{\nabla}\boldsymbol{\sigma}^p - ((\boldsymbol{\nabla}\mathbf{v})^T\cdot\boldsymbol{\sigma}^p + \boldsymbol{\sigma}^p\cdot(\boldsymbol{\nabla}\mathbf{v})). \tag{5}$$

The Giesekus model developed by Giesekus (1982) is defined in Eq. (6). Here, α is the mobility (drag) factor associated with the anisotropic hydrodynamic interactions between the molecules of the polymer in the solvent. The model is derived from the idea that the tensorial drag coefficient depends on the configuration of the polymer molecules. The Giesekus model is equivalent to the one mode Leonov model (Leonov, 1976). The Giesekus model can capture the nonlinear behavior of the viscoelastic materials thanks to the quadratic nonlinearity in the formulation. This model can predict shear-thinning effects, stress overshoot in start-up single shear flow, and first and second normal stress differences. For $\alpha = 0$, the model reduces to the Oldroyd-B model.

$$\boldsymbol{\sigma}^p + \tau' \overset{\nabla}{\boldsymbol{\sigma}}^p + \alpha\frac{\tau'}{\eta^p}(\boldsymbol{\sigma}^p.\boldsymbol{\sigma}^p) = 2\eta_p \boldsymbol{D}. \tag{6}$$

Rouse linear entangled polymers (Rolie-Poly) model is introduced by Likhtman and Graham (2003), which is derived from a refined version of the tube model theory (Graham et al., 2003). The tube model is developed by Doi and Edwards (1988) and is based on the polymer model of De Gennes (1971). This model considers the polymeric

chains to be confined in a tube as shown in Fig. 10, where the tube is formed by surrounding chains. The mechanism of relaxation of the polymer chain is reptation, in which the chain crawls along the tube until completely leaves it.

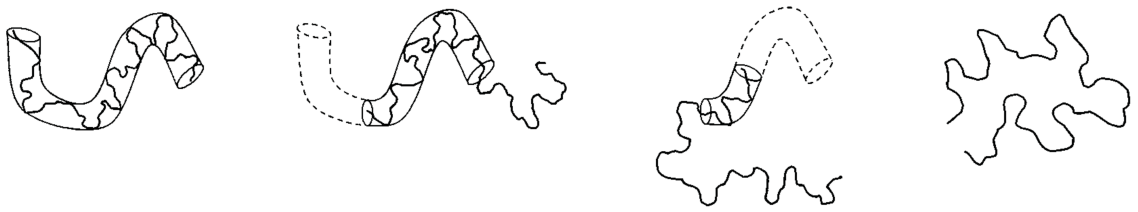

Figure 10: Illustration of tube mechanism [modified from Morrison (2001), Fig. 9.16].

The Rolie-Poly model includes chain stretch, contour length fluctuations, reptation, and convective constraint release (CCR). This model is given in Eq. (7). The parameters ϵ' and q' control respectively the strength of CCR and the suppression of CCR with chain stretch (Holroyd et al., 2017). The amount of CCR can completely remove or reduce the nonmonotonicity of the flow curve. CCR can predict the increase of the stress at higher shear rates as it reduces the alignment of the neighbor chains as a result of the retraction after the stretching. This model consists of an orientation relaxation time τ' and a Rouse relaxation time τ''.

$$\overset{\nabla^p}{\boldsymbol{\sigma}} - \mathbf{v}\cdot\boldsymbol{\nabla}\boldsymbol{\sigma}^p = -\frac{1}{\tau'}\left(\boldsymbol{\sigma}^p - \boldsymbol{I}\right) - \frac{2\left(1-\sqrt{3/\mathrm{tr}\boldsymbol{\sigma}^p}\right)}{\tau''}\left(\boldsymbol{\sigma}^p + \epsilon'\left(\frac{\mathrm{tr}\boldsymbol{\sigma}}{3}\right)^{q'}\left(\boldsymbol{\sigma}^p - \boldsymbol{I}\right)\right). \tag{7}$$

The most intensively studied systems that form shear bands are wormlike micelles, which are flexible cylindrical self-assemblies of surfactant molecules in a solution. Wormlike micelles are also called living polymers because they not only relax through the same processes as polymers, including reptation and Rouse-like motion, but also break and reform reversibly. Shear banding is thought to arise in these systems from the dynamic breakage and recombination processes of the micellar species (Zhou et al., 2008; Germann et al., 2014). During the past decade, a few multi-species models taking these continuous processes into account have been developed using arguments from kinetic theory (Vasquez et al., 2007) and non-equilibrium thermodynamics (Grmela et al., 2010; Germann et al., 2013). For a constitutive model to predict shear banding in semidilute wormlike micellar solutions, the flow curve of the shear stress versus the applied shear rate must be nonmonotonic for a steady homogeneous flow. However, solutions along the decreasing part of this curve are known to be mathematically unstable. The flow, therefore, separates into zones with different shear rates that coexist at identical values of stress. The experimentally observed stress plateau in the region of shear banding can be recovered by including stress diffusion in the constitutive

equation (Zhou et al., 2008, 2010). Stress diffusion also guarantees a unique stress selection and, furthermore, smooths the transition region between the shear bands (Zhou et al., 2008, 2012).

In contrast, the shear stress of semidilute entangled polymer solutions is typically a monotonically increasing function of the shear rate. One disadvantage of the early reptation models for entangled polymers, such as the Doi and Edwards (1988) model, is that they cannot predict a monotonic flow curve in the absence of a large solvent contribution. This is because the mechanism of CCR of the entanglements due to flow and chain stretch are missing in the description. A famous differential approximation of the Doi-Edwards model that includes these features is the Rolie-Poly model. In a numerical study, Adams and Olmsted (2009) showed that the Rolie-Poly model can predict transient shear banding, provided the slope of the monotonic flow curve is small enough. As steady state is achieved, the velocity profile eventually smooths out. In addition to this limitation, shear banding is obtained for much larger entanglement numbers than those found in experiments. Moreover, the high-shear branch cannot be correctly described without violating certain physical criteria used to define the effect of chain stretch on CCR (Adams et al., 2011). By performing a linear stability analysis within a highly general framework that encompasses the most widely used models for the rheology of shear-banding materials, Moorcroft and Fielding (2013) provided a fluid-universal criterion for the onset of shear banding. The theoretical results were supported by the numerical predictions of the Rolie-Poly and Giesekus models (Moorcroft and Fielding, 2014). They showed that materials that undergo a stress overshoot during the start-up of a simple shear flow have a tendency to shear band. Moreover, they found that such models are not capable of predicting steady-state bands if the flow curve is strictly monotonic. In summary, one-fluid models fail to describe polymer systems that display shear bands at steady state and, therefore, their applicability seems to be limited.

Several experimental studies have reported that high-molecular weight polymers can form spatially inhomogeneous concentration profiles when they are subjected to shear flow (Dill and Zimm, 1979; Metzner et al., 1979; MacDonald and Muller, 1996). Dill and Zimm (1979) presented a new method for the separation of large DNA molecules from small ones by radial migration. In their study, they showed that when DNA molecules are sheared in a flow field between a pair of concentric cylinders or cones, they can effectively be separated. This is because the centripetal velocity toward the axis of the apparatus is a power-law function of molecular weight. In addition, Metzner et al. (1979) detected migration effects across streamlines in Poiseuille flows of polymer solutions that fall between the dilute and semidilute concentration range. Their experimental apparatus consisted of a tube that communicates with a concentric cavity filled with the same fluid and whose inlets and outlets are connected via a loop for recirculation.

After the solution was recirculated for a long time, a significant increase of polymer concentration in the stagnant cavity was found. Finally, MacDonald and Muller (1996) performed long-term shearing measurements on a dilute polystyrene solution in a cone-and-plate geometry and used a gel permeation chromatography technique to measure the polymer concentration as a function of the radial position. The large increase in polymer concentration near the apex of the cone and the depletion of the polymer near the edge was related to the shear-induced migration of the polymeric constituents.

The concentration inhomogeneities was explained in a theory by Helfand and Fredrickson (1989), which involves coupling between the concentration fluctuations and the shear stress. The Fickian diffusion reduces the concentration in the regions with higher stress to keep the momentum balance. However, reform of the polymer molecules leads to the further concentration increase in the lower stress region. This diffusional process is called stress-induced migration. The steady state is reached when the Fickian diffusion and the stress-induced migration are balanced.

The two-fluid approach is an appropriate means for describing diffusion processes in complex fluids. This method has predominantly been used in the past to study enhanced concentration fluctuations in wormlike micellar solutions (Fielding and Olmsted, 2003a), polymer solutions (Helfand and Fredrickson, 1989; Milner, 1991; Clarke and McLeish, 1998; Fielding and Olmsted, 2003a), and polymer melts (Doi and Onuki, 1992) near the critical point of phase separation, leading to an observed increase in turbidity. This approach assumes that local gradients in the concentration and - if accounted for - viscoelastic stress generate a nontrivial velocity difference between the constituents of the mixture, which allows them to diffuse at different speeds. To the best of our knowledge, Goveas and Fredrickson (1999) were the first researchers to use a two-fluid model to predict shear banding in a polymeric material. They considered a bidisperse polymer melt and used the UCM model to calculate the viscoelastic stress of each polymer component. In the 1990s, Beris and Edwards (1994) developed a two-fluid description using the generalized bracket approach of non-equilibrium thermodynamics. Almost a decade later, Apostolakis et al. (2002) used this description to investigate shear-induced migration effects in a dilute polymer solution. Unfortunately, they implemented the two-fluid approach in an ad-hoc manner. In the resulting model, the differential velocity only appears in the time evolution equation for polymer conformation. To account for diffusion in the concentration equation, they added second-order gradient terms to this equation. If the differential velocity is assumed to vanish in the radial direction, the flow problem can be closed by imposing a no-flux condition on the polymer concentration at the solid walls and a global constraint of total mass conservation.

Cromer et al. (2013a) hypothesized that shear banding is triggered by diffusion, and for the first time, predicted steady-state banding with a monotonic constitutive curve for the polymer solutions. Inspired by the kinetic theory developed by Goveas and Fredrickson (1999), these authors recently developed a two-fluid model for shear-banding polymer solutions (Cromer et al., 2013b). Their model was obtained by considering only one type of polymer dissolved in a viscous solvent and replacing the Johnson-Segalman model with the Rolie-Poly model. Because this model accounts for chain stretch and CCR, the polymer stress can be predicted more reliably under rapid deformations. In contrast to Apostolakis et al. (2002), they introduced diffusive terms in the time evolution equation for the polymer concentration in a consistent manner. To ensure that the polymer concentration remains conserved, they had to impose a no-flux condition at the solid boundaries. The remaining boundary conditions were constructed so that the differential velocity vanishes at the boundaries (Cromer et al., 2013b, 2014). Their model can predict important features, such as the independency of the solution from the deformation history and initial condition, the occurrence of a banded steady state if the flow is ramped quickly enough from rest, the characteristic long-lived transients of shear-banding fluids, and elastic recoil after fast deformations. By means of a linear stability analysis, Cromer et al. (2014) showed that in opposition to Fickian diffusion, shear-induced migration can force polymers to increase their concentration gradients, thereby creating a shear banding instability for a certain range of parameters. Furthermore, they found that the ratio of the polymer correlation length to the channel width determines the number of bands in planar shear flow. Subsequently, Cromer et al. (2014) incorporated thermal noise in their two-fluid framework through a canonical Langevin approach to investigate concentration fluctuations in semidilute entangled polymer solutions under extensional flow. To prevent divergence in extensional flow, they modified the Rolie-Poly model with a finitely extensible nonlinear elastic-type chain stretch limitation. For the first time, the finite-wavelength concentration fluctuation amplification observed experimentally by van Egmond and Fuller (1993) could be predicted. In summary, these recent studies highlight the importance of accounting for diffusional effects. They confirm that a reliable time evolution equation for the conformation/extra stress tensor is required in order to be able to correctly predict phenomena that are related to the coupling between polymer stress and concentration.

Germann et al. (2014) improved the two-fluid framework for viscoelastic fluids developed by Beris and Edwards (1994) using the generalized bracket approach of non-equilibrium thermodynamics. This new formulation is advantageous because the total mass is conserved by the time evolution equations themselves. Consequently, it can easily be applied to viscoelastic systems comprising more than two phases. In addition, it is no longer necessary to impose a no-flux condition on the polymer concentration in order to prevent the outflow of material through the system boundaries. As in all other previous approaches, the differential velocity was considered to be

an intermediate variable, which complicates the specifications of the additional boundary conditions arising from the higher-order diffusive terms. To overcome this difficulty, the same authors suggested treating the differential velocity as a state variable (Germann et al., 2016). Consequently, the additional boundary conditions arising from the derivative diffusive terms can be imposed directly with respect to this new state variable. For instance, no-slip and no-flux boundary conditions translate into the requirements that the tangential and normal components, respectively, of the differential velocity must vanish at the boundaries.

We modified the two-fluid approach developed by Germann et al. (2014, 2016) to describe shear banding in semidilute entangled polymer solutions. In the time evolution equation for the conformation tensor, a nonlinear Giesekus relaxation is used to capture the overshoot occurring during a rapid start-up of a simple shearing flow, shear-thinning behavior, and nontrivial first and second normal stress differences. We believe that the Giesekus relaxation is an appropriate choice, as it was originally derived from dumbbell kinetic theory using hydrodynamic drag and Brownian motion to account for the interactions between the polymeric constituents in a concentrated solution or melt. In addition, we included a second nonlinear relaxation term to describe the monotonic growth of the shear stress at large shear rates. This term is similar to the one used in the Rolie-Poly model accounting for CCR and chain stretch (Likhtman and Graham, 2003). We also added a nonlocal stress diffusion to have smooth and unique banded profiles. The new model is based on the hypothesis that the coupling between stress and concentration of the polymer generates steady-state shear banding.

2.2 Model derivation

The first step to derive a viscoelastic model by generalized bracket approach (Beris and Edwards, 1994) is to specify the state variables, which describe the state of the system. The polymer number density $n_p = (\rho_p/M_p)N_A$ is defined to represent the number of constitutive particles per unit volume, where ρ_p is the polymer mass density, M_p is the polymer molecular weight, and N_A is the Avogadro constant. It must be noted that throughout this thesis, by total concentration c (as defined in Sec. 1) we mean the weight ratio of the polymer to the solution, and by concentration n_p we mean the polymer number density. Furthermore, we define conformation density tensor $\mathbf{c}$, and structural tensorial parameter density $\mathbf{C} = n_p\mathbf{c}$. The conformation is defined as the instantaneous shape of a polymer molecule, regarding the fact that the polymer constituents change their shape continuously in the solution (Teraoka, 2002). The elastic strain of the solution is represented by the conformational state of the polymer molecule. The conformation density tensor is the average second moment of the end-to-end vector of a polymer chain, which is shown in Fig. 11.

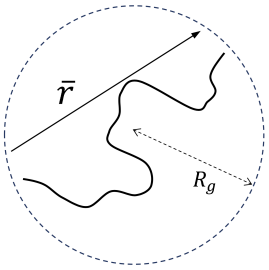

Figure 11: Schematic of the end-to-end vector $\bar{r}$ of a polymer chain with radius of gyration R_g.

We consider the total system to be close, isothermal, and incompressible. The system consists of one component of polymeric constituents and one component of viscous solvent. The following variables are defined: polymer mass density ρ_p, polymer velocity field $\mathbf{v}^p$, polymer momentum density $\mathbf{m}^p = \rho_p\mathbf{v}^p$, polymer molecular weight M_p, polymer number density n_p, and polymer conformation density tensor $\mathbf{c}$. Furthermore, we define solvent mass density ρ_s, solvent velocity field $\mathbf{v}^s$, solvent molecular weight M_s, solvent number density n_s, and solvent momentum density $\mathbf{m}^s = \rho_s\mathbf{v}^s$. The total mass of the polymeric solution is $\rho = \rho_p + \rho_s$.

Within the bracket formalism of non-equilibrium thermodynamics (Beris and Edwards, 1994), the system dynamics are described by the master equation

$$\frac{dF}{dt} = \{[F, H]\} = \{F, H\} + [F, H]\,, \tag{8}$$

where $\{[F, H]\}$ is the generalized bracket, F is an arbitrary function of the state variables of the system and H is the Hamiltonian or the total system energy. The Poisson bracket $\{\,\cdot\,,\,\cdot\,\}$ and the dissipation bracket $[\,\cdot\,,\,\cdot\,]$ represent the reversible and irreversible contributions, respectively, to the system dynamics. We consider the total system energy to be characterized by the kinetic energy H_k and the elastic potential energy H_e:

$$H = H_k + H_e\,, \tag{9}$$

defined by

$$H = \int_\Omega \frac{1}{2}\left(\frac{\mathbf{m}^p \cdot \mathbf{m}^p}{\rho_p} + \frac{\mathbf{m}^s \cdot \mathbf{m}^s}{\rho_s}\right) \mathrm{d}^3x + \int_\Omega \frac{1}{2}\left\{K \mathrm{tr}\mathbf{C} - n_p k_B T \ln \det\left(\frac{K\mathbf{C}}{n_p k_B T}\right)\right\} \mathrm{d}^3x. \tag{10}$$

Here, Ω is the flow domain, K is the Hookean spring constant associated with the polymer, k_B is the Boltzmann constant, and T is the absolute temperature. The first term on the right-hand side of Eq. (10) represents contributions of the polymeric constituents and the solvent to the kinetic energy and the second term represents the elastic free energy associated with the Hookean dumbbells of the polymers. For simplicity, we do not consider any dependence of the total system energy on gradients in the state variables.

Differentiating the Hamiltonian with respect to the momentum densities of the polymer and the solvent yields

$$\delta H/\delta \mathbf{m}^p = \mathbf{m}^p/\rho_p = \mathbf{v}^p, \tag{11}$$

and

$$\delta H/\delta \mathbf{m}^s = \mathbf{m}^s/\rho_s = \mathbf{v}^s. \tag{12}$$

Differentiation of $F = F(\rho_s, \rho_p, \mathbf{m}^s, \mathbf{m}^p, \mathbf{c})$ with respect to time gives:

$$\frac{dF}{dt} = \frac{\delta F}{\delta \rho_p} \cdot \frac{\delta \rho_p}{\delta t} + \frac{\delta F}{\delta \rho_s} \cdot \frac{\delta \rho_s}{\delta t} + \frac{\delta F}{\delta \mathbf{m}^p} \cdot \frac{\delta \mathbf{m}^p}{\delta t} + \frac{\delta F}{\delta \mathbf{m}^s} \cdot \frac{\delta \mathbf{m}^s}{\delta t} + \frac{\delta F}{\delta \mathbf{c}} \cdot \frac{\delta \mathbf{c}}{\delta t}. \tag{13}$$

We can write the Poisson bracket for the set of state variables ρ_p, ρ_s, $\mathbf{m}^p$, $\mathbf{m}^s$, and $\mathbf{c}$, according to its definition as follows (Beris and Edwards, 1994):

$$\begin{aligned}
\{F, H\} = &- \int_\Omega \left\{ \frac{\delta F}{\delta \rho_p} \nabla_\beta \left(\frac{\delta H}{\delta m_\beta^p} \rho_p \right) - \frac{\delta H}{\delta \rho_p} \nabla_\beta \left(\frac{\delta F}{\delta m_\beta^p} \rho_p \right) \right\} \mathrm{d}^3 x \\
&- \int_\Omega \left\{ \frac{\delta F}{\delta \rho_s} \nabla_\beta \left(\frac{\delta H}{\delta m_\beta^s} \rho_s \right) - \frac{\delta H}{\delta \rho_s} \nabla_\beta \left(\frac{\delta F}{\delta m_\beta^s} \rho_s \right) \right\} \mathrm{d}^3 x \\
&- \int_\Omega \left\{ \frac{\delta F}{\delta m_\gamma^p} \nabla_\beta \left(\frac{\delta H}{\delta m_\beta^p} m_\gamma^p \right) - \frac{\delta H}{\delta m_\gamma^p} \nabla_\beta \left(\frac{\delta F}{\delta m_\beta^p} m_\gamma^p \right) \right\} \mathrm{d}^3 x \\
&- \int_\Omega \left\{ \frac{\delta F}{\delta m_\gamma^s} \nabla_\beta \left(\frac{\delta H}{\delta m_\beta^s} m_\gamma^s \right) - \frac{\delta H}{\delta m_\gamma^s} \nabla_\beta \left(\frac{\delta F}{\delta m_\beta^s} m_\gamma^s \right) \right\} \mathrm{d}^3 x \\
&- \int_\Omega \left\{ \frac{\delta F}{\delta C_{\alpha\beta}} \nabla_\gamma \left(\frac{\delta H}{\delta m_\gamma^p} C_{\alpha\beta} \right) - \frac{\delta H}{\delta C_{\alpha\beta}} \nabla_\gamma \left(\frac{\delta F}{\delta m_\gamma^p} C_{\alpha\beta} \right) \right\} \mathrm{d}^3 x \\
&- \int_\Omega C_{\alpha\gamma} \left(\frac{\delta H}{\delta C_{\alpha\beta}} \nabla_\gamma \frac{\delta F}{\delta m_\beta^p} - \frac{\delta F}{\delta C_{\alpha\beta}} \nabla_\gamma \frac{\delta H}{\delta m_\beta^p} \right) \mathrm{d}^3 x \\
&- \int_\Omega C_{\beta\gamma} \left(\frac{\delta H}{\delta C_{\alpha\beta}} \nabla_\gamma \frac{\delta F}{\delta m_\alpha^p} - \frac{\delta F}{\delta C_{\alpha\beta}} \nabla_\gamma \frac{\delta H}{\delta m_\alpha^p} \right) \mathrm{d}^3 x \,.
\end{aligned} \tag{14}$$

If we substitute Eq. (11)-(13) in Eq. (14), the time evolution equations for the state variables without any dissipation become

$$\frac{\partial \rho_p}{\partial t} = -\nabla_\alpha \left(v_\alpha^p \rho_p \right) , \tag{15}$$

$$\frac{\partial \rho_s}{\partial t} = -\nabla_\alpha \left(v_\alpha^s \rho_s \right) , \tag{16}$$

$$\frac{\partial}{\partial t} \left(\rho_p v_\alpha^p \right) = -\nabla_\beta \left(v_\beta^p \rho_p v_\alpha^p \right) - m_\beta^p \nabla_\alpha \left(\frac{\delta H}{\delta m_\beta^p} \right) - \rho_p \nabla_\alpha \left(\frac{\delta H}{\delta \rho_p} \right) - C_{\beta\gamma} \nabla_\alpha \left(\frac{\delta H}{\delta C_{\beta\gamma}} \right) + \nabla_\beta \sigma_{\beta\alpha}^p \,, \tag{17}$$

$$\frac{\partial}{\partial t} \left(\rho_s v_\alpha^s \right) = -\nabla_\beta \left(v_\beta^s \rho_s v_\alpha^s \right) - \rho_s \nabla_\alpha \left(\frac{\delta H}{\delta \rho_s} \right) - m_\beta^s \nabla_\alpha \left(\frac{\delta H}{\delta m_\beta^s} \right) , \tag{18}$$

$$\frac{\partial C_{\alpha\beta}}{\partial t} = -\nabla_\gamma \left(v_\gamma^p C_{\alpha\beta} \right) + C_{\gamma\alpha} \nabla_\gamma v_\beta^p + C_{\gamma\beta} \nabla_\gamma v_\alpha^p \,, \tag{19}$$

where $\boldsymbol{\sigma}^p$ denotes the extra stress associated with the polymer, which is defined as

$$\sigma^p_{\alpha\beta} \equiv 2C_{\alpha\gamma}\frac{\delta H}{\delta C_{\gamma\beta}} = KC_{\alpha\beta} - n_p k_B T \delta_{\alpha\beta}\,. \tag{20}$$

New set of variables are defined to include the incompressibility constraint corresponding to a constant total mass density (Beris and Edwards, 1994). Let the mass average velocity be defined as

$$\mathbf{v} \equiv \frac{\rho_p}{\rho}\mathbf{v}^p + \frac{\rho_s}{\rho}\mathbf{v}^s, \tag{21}$$

and the differential velocity be defined as

$$\boldsymbol{\Delta}\mathbf{v} \equiv \mathbf{v}^p - \mathbf{v}^s\,. \tag{22}$$

Correspondingly, the total momentum density is given as

$$\mathbf{m} \equiv \mathbf{m}^p + \mathbf{m}^s, \tag{23}$$

and the differential momentum density is given as

$$\boldsymbol{\Delta}\mathbf{m} \equiv \frac{\rho_s}{\rho}\mathbf{m}^p - \frac{\rho_p}{\rho}\mathbf{m}^s\,. \tag{24}$$

Differentiating the kinetic part of the Hamiltonian provided above yields

$$\delta H_k/\delta\mathbf{m} = \delta H/\delta\mathbf{m} = \mathbf{v}, \tag{25}$$

and

$$\delta H_k/\delta(\boldsymbol{\Delta}\mathbf{m}) = \delta H/\delta(\boldsymbol{\Delta}\mathbf{m}) = \boldsymbol{\Delta}\mathbf{v}. \tag{26}$$

As in the Newtonian case, the time evolution equation of the total momentum density can be obtained by adding

those of the individual phase momentum densities. That is, if we add Eqs. (17) and (18) and then use the continuity Eqs. (15) and (16), we obtain the following time evolution equation for the total momentum density:

$$\rho\frac{\partial v_\alpha}{\partial t} = -\rho v_\beta \nabla_\beta v_\alpha - \nabla_\alpha p + \nabla_\beta \sigma^p_{\beta\alpha}\,, \tag{27}$$

where the thermodynamic pressure is defined as usual as

$$p = -h + \rho_p\frac{\delta H}{\delta \rho_p} + m^p_\beta\frac{\delta H}{\delta m^p_\beta} + \rho_s\frac{\delta H}{\delta \rho_s} + m^s_\beta\frac{\delta H}{\delta m^s_\beta} + C_{\beta\gamma}\frac{\delta H}{\delta C_{\beta\gamma}}\,. \tag{28}$$

Here, h represents the total local free energy density, defined as $H = \int_\Omega h\,\mathrm{d}^3x$. The viscoelasticity that appears in Eq. (27) is a dissipative contribution in the form of the divergence of the extra stress on the right-hand side. Similarly, adding the continuity Eqs. (15) and (16) together obtains

$$\frac{\partial \rho}{\partial t} = -\nabla_\alpha\left(v_\alpha \rho\right)\,. \tag{29}$$

If we further assume that the total mass density of the polymeric solution remains, like that of most fluids, nearly constant, this equation simplifies to the well-known divergence-free constraint

$$\nabla_\alpha v_\alpha = 0\,. \tag{30}$$

Consequently, it is no longer necessary to calculate the pressure via Eq. (29). The pressure here is simply a projector operator of the velocity derivative in divergence-free space. The continuity equation for the incompressible mixture has the form

$$\boldsymbol{\nabla}\cdot\mathbf{v} = 0\,. \tag{31}$$

The time evolution equation of the total velocity is given by

$$\rho \frac{\partial \mathbf{v}}{\partial t} = \; - \rho \mathbf{v} \cdot \boldsymbol{\nabla} \mathbf{v} - \boldsymbol{\nabla} p + \boldsymbol{\nabla} \cdot \boldsymbol{\sigma} \, . \tag{32}$$

Eq. (32) is the Cauchy momentum balance, where p represents the pressure and $\boldsymbol{\sigma}$ the total stress tensor. The total stress is obtained from Eq. (43), which consists of the Cauchy stress from the solvent and the extra stress associated with the polymer constituents.

The time evolution equation for the polymer number density has the following form:

$$\frac{\partial n_p}{\partial t} = \; - \boldsymbol{\nabla} \cdot \left(\mathbf{v}^p \, n_p \right) \, , \tag{33}$$

where the left-hand side and the term on the right-hand side constitute the material derivative. This equation accounts for the fact that the number density is allowed to vary locally.

If we subtract Eqs. (17) from (18), multiply the first by ρ_s/ρ_p and the second by ρ_p/ρ_s, and then make use of the continuity Eqs. (15) and (16), we obtain a time evolution equation for the differential velocity. By ignoring all inertial terms that are proportional to the square of the differential velocity, this equation becomes

$$\begin{aligned} \frac{\rho_p \rho_s}{\rho} \frac{\partial \Delta v_\alpha}{\partial t} = & - \frac{\rho_p \rho_s}{\rho} v_\beta \nabla_\beta \Delta v_\alpha + \frac{\rho_s}{\rho} \left\{ - m^p_\beta \nabla_\alpha \left(\frac{\delta H}{\delta m^p_\beta} \right) - \rho_p \nabla_\alpha \left(\frac{\delta H}{\delta \rho_p} \right) - C_{ij} \boldsymbol{\nabla} \left(\frac{\delta H}{\delta C_{ij}} \right) + \boldsymbol{\nabla} \cdot \boldsymbol{\sigma}^p \right\} \\ & - \frac{\rho_p}{\rho} \left\{ - \rho_s \nabla_\alpha \left(\frac{\delta H}{\delta \rho_s} \right) - m^s_\beta \nabla_\alpha \left(\frac{\delta H}{\delta m^s_\beta} \right) \right\} . \end{aligned} \tag{34}$$

In the above equation, the higher-order inertial terms have been ignored to obtain a simplified expression of the substantial derivative. We believe that the first-order approximation is justified for slow flows. As polymers in semidilute solutions have low inertia because of their small volume fraction, they follow the motion of the ambient solvent quickly under the action of large drag forces.

Next, we proceed with the irreversible contributions using the dissipation bracket. A term accounting for the viscous

drag between the polymer constituents and the viscous solvent must be included in the system dynamics, i.e.,

$$[F,H] = -\int_{\Omega} Z_{\alpha\beta} \frac{\delta F}{\delta\left(\Delta m_{\alpha}\right)} \frac{\delta H}{\delta\left(\Delta m_{\beta}\right)} \mathrm{d}^3 x\,, \tag{35}$$

where the drag coefficient tensor $Z_{\alpha\beta}$ is approximated by an isotropic tensor $G_0/D\delta_{\alpha\beta}$, where $G_0 = n_p^0 k_B T$ is the modulus of elasticity evaluated at the linear viscoelastic limit and D is the scalar diffusivity. In addition, we can describe the viscous dissipation as follows:

$$[F,H] = -\int_{\Omega} \frac{\eta_s}{2} \left\{ \nabla_{\alpha} \left(\frac{\delta F}{\delta m_{\beta}^s} \right) + \nabla_{\beta} \left(\frac{\delta F}{\delta m_{\alpha}^s} \right) \right\} \left\{ \nabla_{\alpha} \left(\frac{\delta H}{\delta m_{\beta}^s} \right) + \nabla_{\beta} \left(\frac{\delta H}{\delta m_{\alpha}^s} \right) \right\} \mathrm{d}^3 x\,, \tag{36}$$

where η_s denotes the Newtonian solvent viscosity. The final form of the time evolution equation for the differential velocity is given by

$$\frac{\rho_p \rho_s}{\rho} \left(\frac{\partial}{\partial t} + \mathbf{v} \cdot \boldsymbol{\nabla} \right) (\boldsymbol{\Delta v}) = \frac{\rho_s}{\rho} \left\{ -\boldsymbol{\nabla} \left(n_p k_B T \right) + \boldsymbol{\nabla} \cdot \boldsymbol{\sigma}^p \right\} - \frac{\rho_p}{\rho} \{ -\boldsymbol{\nabla} \left(n_s k_B T \right) + \eta_s \boldsymbol{\nabla}^2 \mathbf{v}^s \} - \frac{G_0}{D} \boldsymbol{\Delta v}\,, \tag{37}$$

where the local diffusivity constant D controls the diffusion between the solvent and the polymer. At the diffusionless limit, i.e., if we let $D \to 0$, we obtain $\boldsymbol{\Delta v} \to 0$. Fickian diffusion is described by the spatial gradients of the number densities associated with the polymer and the solvent. The divergence of $\boldsymbol{\sigma}^p$ accounts for the stress-induced migration diffusion. The fact that the differential velocity is a state variable in our model is advantageous since the boundary conditions can be directly imposed with respect to this variable. For instance, if we assume no slip occurs along the solid walls, we simply have to force the tangential component of the differential velocity to vanish there. Furthermore, no material flux is enforced by requiring the normal component of the differential velocity to vanish. This mathematical treatment is now possible because the Laplacian of the differential velocity implicitly appears on the right-hand side of Eq. (37). In summary, by considering the differential velocity as state variable, the additional boundary conditions can be formulated in a mathematically correct and straightforward way. This will be especially important when considering slip along the walls and flows in more complicated geometries. It must be noted that the components of the variable $\boldsymbol{\Delta v}$ are zero at the steady state.

To reduce numerical errors in the calculation of an inhomogeneous flow, we use $\mathbf{c}$ as the unknown variable in the

final model rather than $\mathbf{C}$. Ignoring the entropy correction terms leads to

$$[F, H_m] = -\int_\Omega \Lambda^1_{\alpha\beta\gamma\varepsilon} \frac{\delta F}{\delta C_{\alpha\beta}} \frac{\delta H_m}{\delta C_{\gamma\varepsilon}} d^3x - \int_\Omega \Lambda^2_{\alpha\beta\gamma\varepsilon} \frac{\delta F}{\delta C_{\alpha\beta}} \frac{\delta H_m}{\delta C_{\gamma\varepsilon}} d^3x \,, \tag{38}$$

where $\Lambda^1_{\alpha\beta\gamma\varepsilon}$ and $\Lambda^2_{\alpha\beta\gamma\varepsilon}$ are general fourth-order relaxation tensors. The first integral on the right-hand side of Eq. (38) accounts for a nonlinear Giesekus relaxation, where its phenomenological relaxation matrix is given by

$$\Lambda^1_{\alpha\beta\gamma\varepsilon} = \frac{1}{2\lambda_1 K}[(1-\alpha)(C_{\alpha\gamma}\delta_{\beta\varepsilon} + C_{\beta\gamma}\delta_{\alpha\varepsilon} + C_{\alpha\varepsilon}\delta_{\beta\gamma} + C_{\beta\varepsilon}\delta_{\alpha\gamma}) + 2\alpha\frac{K}{k_B T}(c_{\alpha\gamma}C_{\beta\varepsilon} + c_{\alpha\varepsilon}C_{\beta\gamma})] \,. \tag{39}$$

Here, λ_1 can be identified as the reptation time, and α is the mobility factor, which relates to the anisotropic relaxation of the polymer chains. At $\alpha = 0$, we recover the Maxwellian relaxation. As the upturn of the shear stress at high shear rates can only be described using a nonlinear relaxation term taking the extension of the polymeric constituents into account, we selected the following phenomenological relaxation matrix:

$$\Lambda^2_{\alpha\beta\gamma\varepsilon} = \frac{\left[\mathrm{tr}(\frac{K}{k_B T}\mathbf{c}) - 3\right]^q}{2\lambda_2 K}(C_{\alpha\gamma}\delta_{\beta\varepsilon} + C_{\beta\gamma}\delta_{\alpha\varepsilon} + C_{\alpha\varepsilon}\delta_{\beta\gamma} + C_{\beta\varepsilon}\delta_{\alpha\gamma}) \,, \tag{40}$$

where λ_2 is the Rouse relaxation time.

Below a critical value of the shear stress versus shear rate slope, the solution may not be smooth, even if the flow curve is monotonic. There are several ways to avoid this type of discontinuity. The standard approach is to add stress diffusion to the time evolution equation of the conformation/extra stress tensor (Fielding and Olmsted, 2003b). Another approach is to include a square-gradient approximation in the mixing free energy to account for size effects (Cromer et al., 2013b). This type of regularization is weakly nonlocal, i.e., only neighboring points are notably affected by this modification, and it has made no significant difference in our case. Therefore, we follow the standard approach and construct a new expression for stress diffusion using the generalized bracket approach of non-equilibrium thermodynamics. The new expression is based on the one used by Beris and Edwards (1994) to account for stress diffusion in one-fluid models:

$$\begin{aligned}[F, H_m] = &-\int_\Omega B_{\alpha\beta}\left(\nabla_\gamma\left(C_{\gamma\lambda}\frac{\delta F}{\delta C_{\lambda\alpha}}\right)\right)\left(\nabla_\varepsilon\left(C_{\varepsilon\kappa}\frac{\delta H}{\delta C_{\kappa\beta}}\right)\right) d^3x \\ &-\int_\Omega B_{\alpha\beta}\left(\nabla_\gamma\left(C_{\gamma\lambda}\frac{\delta H}{\delta C_{\lambda\alpha}}\right)\right)\left(\nabla_\varepsilon\left(C_{\varepsilon\kappa}\frac{\delta F}{\delta C_{\kappa\beta}}\right)\right) d^3x \,,\end{aligned} \tag{41}$$

where $B_{\alpha\beta}$ is a second-order transport coefficient. For simplicity, we only consider isotropic transport coefficients, which leads to $B_{\alpha\beta} = 2D_{nonloc}\delta_{\alpha\beta}$. To obtain an expression that satisfies material objectivity, however, it is necessary to supplement the expression with the second term on the right-hand side of Eq. (41). We finally obtain the time evolution equation for the polymer conformation, which is the constitutive equation of the system, as

$$\begin{aligned}\frac{\partial \mathbf{c}}{\partial t} = & -\mathbf{v}^p \cdot \boldsymbol{\nabla}\mathbf{c} + \mathbf{c}\cdot\boldsymbol{\nabla}\mathbf{v}^p + \left(\boldsymbol{\nabla}\mathbf{v}^p\right)^T \cdot \mathbf{c} - \frac{1}{\lambda_1}\left[(1-\alpha)\,\mathbf{I} + \alpha\frac{K}{k_BT}\mathbf{c}\right] \cdot \left(\mathbf{c} - \frac{K}{k_BT}\mathbf{I}\right) \\ & + \frac{1}{\lambda_2}\left[\mathrm{tr}(\frac{K}{k_BT}\mathbf{c}) - 3\right]^q \left(\mathbf{c} - \frac{K}{k_BT}\mathbf{I}\right) + D_{nonloc}\left(\mathbf{c}\cdot\boldsymbol{\nabla}\left(\boldsymbol{\nabla}\cdot\boldsymbol{\sigma}^p\right) + \left[\boldsymbol{\nabla}\left(\boldsymbol{\nabla}\cdot\boldsymbol{\sigma}^p\right)\right]^T \cdot \mathbf{c}\right) . \end{aligned} \tag{42}$$

The partial time derivative on the left-hand side and the first three terms on the right-hand side constitute the upper-convected time derivative of the conformation tensor. The fourth term involving parameter α accounts for the Giesekus relaxation. This term takes into account hydrodynamic drag and Brownian motion. Furthermore, it accounts for shear-thinning behavior and nontrivial first and second normal stress differences. As this relaxation generates an overshoot during the start-up of a simple shearing flow, shear band formation can be triggered. The relationship between the mobility tensor and the conformation tensor is linear in this term. The fifth term, involving prefactor $[K/(k_BT)\mathrm{tr}\mathbf{c}) - 3]^q$, is a second nonlinear relaxation term. This term has been added to generate the upturn of the flow curve at high shear rates. The prefactor depends on the trace of the conformation tensor because it is a relative measure of polymer stretch. This term vanishes at the linear viscoelastic limit. Note that this term resembles the term used in the Rolie-Poly model accounting for CCR and chain stretch (Likhtman and Graham, 2003). The Rolie-Poly model was not considered here to describe the conformational dynamics, as the CCR term of this model cannot be derived within the framework of non-equilibrium thermodynamics. Leygue et al. (2001) developed an expression for CCR using the generalized bracket approach of non-equilibrium thermodynamics. However, like the Marrucci-Grego-Ianniruberto model (Leygue et al., 2001), this model does not consider chain stretching. Moreover, because of the strain measure used, it cannot be easily incorporated in the two-fluid approach of Germann et al. (2014, 2016). Parameter D_{nonloc}, appearing in the last term of Eq. (42), controls the smoothness of the profiles.

The above set of time evolution Eqs. (31)-(33), (37), and (42) is closed by an explicit expression for the total stress

$$\boldsymbol{\sigma} = \boldsymbol{\sigma}^p + \eta_s \left[\boldsymbol{\nabla} \mathbf{v}^s + (\boldsymbol{\nabla} \mathbf{v}^s)^T \right] = n_p \left(K\mathbf{c} - k_B T \mathbf{I} \right) + \eta_s \left[\boldsymbol{\nabla} \mathbf{v}^s + (\boldsymbol{\nabla} \mathbf{v}^s)^T \right] , \tag{43}$$

where the first term accounts for the extra stress as the viscoelastic contribution of the polymer and the second term accounts for the stress associated with the viscous solvent. The phase velocities appearing in the time evolution equations can be calculated from the total average velocity and the differential velocity as follows:

$$\mathbf{v}^p = \mathbf{v} + \frac{\rho_s}{\rho} \boldsymbol{\Delta} \mathbf{v} \,, \tag{44}$$

$$\mathbf{v}^s = \mathbf{v} - \frac{\rho_p}{\rho} \boldsymbol{\Delta} \mathbf{v} \,. \tag{45}$$

In the equilibrium state of rest ($\mathbf{v} = 0$ and $\boldsymbol{\Delta} \mathbf{v} = 0$), we can obtain the analytical solution of $n_p = n_p^0$ and $\mathbf{c} = (k_B T / K) \, \mathbf{I}$.

2.3 Dimensionless model equations

We work with dimensionless quantities. The spatial position is scaled by the characteristic height, $\tilde{\mathbf{x}} = \mathbf{x}/H$, time is scaled by the characteristic relaxation time, $\tilde{t} = t/\lambda_1$, pressure is scaled by the plateau modulus, $\tilde{p} = p/G_0$, the total stress is scaled as $\tilde{\boldsymbol{\sigma}} = \boldsymbol{\sigma}/G_0$, and the conformation tensor associated with the polymer is scaled as $\tilde{\mathbf{c}} = (K/k_BT)\mathbf{c}$. The polymer and solvent number densities are normalized using the values at the equilibrium state as $\tilde{n}_p = n_p/n_p^0$ and $\tilde{n}_s = n_s/n_s^0$, respectively. The dimensionless parameters with respect to these scalings are: the elasticity number $E = G_0\lambda_1^2/(\rho H^2)$, which is the reciprocal of the Reynolds number; the ratio of the molecular weight of the solvent to that of the polymer $\chi = M_s/M_p$; the viscosity ratio $\beta = \eta_s/\eta_0$, where $\eta_0 = \eta_s + \eta_p = G_0\lambda_1$ is the zero shear viscosity; and the ratio of the two characteristic relaxation times $\varepsilon = \lambda_1/\lambda_2$. By assuming an initially uniform polymer number density in the flow field, the total polymer number density can be calculated as $\mu = \tilde{n}_p^0/(\tilde{n}_p^0 + \chi\tilde{n}_s^0)$. The nondimensional diffusion coefficients are defined as $\tilde{D} = D\lambda_1/H^2$ and $\tilde{D}_{nonloc} = D_{nonloc}\lambda_1/H^2$. The nondimensionalized form of the model Eqs. (31)-(33), (37), (42)-(45) are respectively:

$$\widetilde{\boldsymbol{\nabla}}\cdot\widetilde{\mathbf{v}} = 0\,, \tag{46}$$

$$E^{-1}\frac{\partial\widetilde{\mathbf{v}}}{\partial\widetilde{t}} = -E^{-1}\widetilde{\mathbf{v}}\cdot\widetilde{\boldsymbol{\nabla}}\widetilde{\mathbf{v}} - \widetilde{\boldsymbol{\nabla}}\widetilde{p} + \widetilde{\boldsymbol{\nabla}}\cdot\widetilde{\boldsymbol{\sigma}}\,, \tag{47}$$

$$\frac{\partial\widetilde{n}_p}{\partial\widetilde{t}} = -\widetilde{\boldsymbol{\nabla}}\cdot\left(\widetilde{\mathbf{v}}^p\widetilde{n}_p\right)\,, \tag{48}$$

$$\begin{aligned} E^{-1}\frac{\chi\widetilde{n}_s\widetilde{n}_p}{\left(\widetilde{n}_p+\chi\widetilde{n}_s\right)^2}\left(\frac{\partial}{\partial\widetilde{t}}+\widetilde{\mathbf{v}}\cdot\widetilde{\boldsymbol{\nabla}}\right)\left(\widetilde{\boldsymbol{\Delta}\mathbf{v}}\right) &= \frac{\chi\widetilde{n}_s}{\widetilde{n}_p+\chi\widetilde{n}_s}\left\{-\widetilde{\boldsymbol{\nabla}}\widetilde{n}_p + \widetilde{\boldsymbol{\nabla}}\cdot\widetilde{\boldsymbol{\sigma}}^p\right\} \\ &\quad - \frac{\widetilde{n}_p}{\widetilde{n}_p+\chi\widetilde{n}_s}\{-\widetilde{\boldsymbol{\nabla}}\widetilde{n}_s + \beta\widetilde{\boldsymbol{\nabla}}^2\widetilde{\mathbf{v}}^s\} - \widetilde{D}\widetilde{\boldsymbol{\Delta}\mathbf{v}}\,, \end{aligned} \tag{49}$$

$$\begin{aligned} \frac{\partial\widetilde{\mathbf{c}}}{\partial\widetilde{t}} &= -\widetilde{\mathbf{v}}^p\cdot\widetilde{\boldsymbol{\nabla}}\widetilde{\mathbf{c}} + \widetilde{\mathbf{c}}\cdot\widetilde{\boldsymbol{\nabla}}\widetilde{\mathbf{v}}^p + (\widetilde{\boldsymbol{\nabla}}\widetilde{\mathbf{v}}^p)^T\cdot\widetilde{\mathbf{c}} - [(1-\alpha)\mathbf{I} + \alpha\widetilde{\mathbf{c}}](\widetilde{\mathbf{c}}-\mathbf{I}) + \varepsilon(\mathrm{tr}\widetilde{\mathbf{c}}-3)^q(\widetilde{\mathbf{c}}-\mathbf{I}) \\ &\quad + \tilde{D}_{nonloc}\left(\widetilde{\mathbf{c}}\cdot\widetilde{\boldsymbol{\nabla}}\left(\widetilde{\boldsymbol{\nabla}}\cdot\widetilde{\boldsymbol{\sigma}}^p\right) + \left[\widetilde{\boldsymbol{\nabla}}\left(\widetilde{\boldsymbol{\nabla}}\cdot\widetilde{\boldsymbol{\sigma}}^p\right)\right]^T\cdot\widetilde{\mathbf{c}}\right)\,, \end{aligned} \tag{50}$$

$$\widetilde{\boldsymbol{\sigma}} = \widetilde{\boldsymbol{\sigma}}^p + \beta\left[\widetilde{\boldsymbol{\nabla}}\widetilde{\mathbf{v}}^s + \left(\widetilde{\boldsymbol{\nabla}}\widetilde{\mathbf{v}}^s\right)^T\right] = \widetilde{n}_p(\widetilde{\mathbf{c}}-\mathbf{I}) + \beta\left[\widetilde{\boldsymbol{\nabla}}\widetilde{\mathbf{v}}^s + \left(\widetilde{\boldsymbol{\nabla}}\widetilde{\mathbf{v}}^s\right)^T\right]\,, \tag{51}$$

$$\widetilde{\mathbf{v}}^p = \widetilde{\mathbf{v}} + \frac{\chi\widetilde{n}_s}{\widetilde{n}_p+\chi\widetilde{n}_s}\widetilde{\boldsymbol{\Delta}\mathbf{v}}\,, \tag{52}$$

$$\widetilde{\mathbf{v}}^s = \widetilde{\mathbf{v}} - \frac{\widetilde{n}_p}{\widetilde{n}_p+\chi\widetilde{n}_s}\widetilde{\boldsymbol{\Delta}\mathbf{v}}. \tag{53}$$

2.4 Influence of the model parameters

To determine the values of the model parameters, we first consider the special case of steady homogeneous shear flow shown in Fig. 12. The gap width of the channel, H, is considered as the characteristic length.

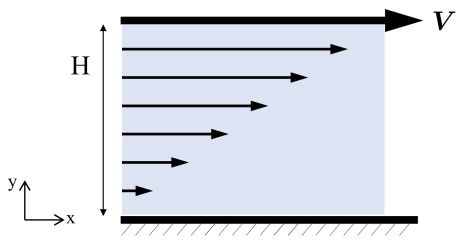

Figure 12: Schematic of a steady homogeneous shear flow.

Homogeneous shear flow can be obtained by assuming the shear rate $\tilde{\dot{\gamma}} = \partial \tilde{\mathrm{v}}_{\mathrm{x}}/\partial \tilde{\mathrm{y}}$ across the gap to be constant. Under this condition, the differential velocity is identically zero; furthermore, the new model reduces to the standard Giesekus model for $\varepsilon = 0$. As the values of the model parameters are typically determined under homogeneous flow conditions, this type of flow is of relevance. After eliminating the zero terms, the governing set of algebraic flow equations for the homogeneous flow in the Cartesian coordinate system becomes as below:

$$\tilde{\sigma}_{xx} = \tilde{n}_p \left(\tilde{c}_{xx} - 1\right), \tag{54}$$

$$\tilde{\sigma}_{yy} = \tilde{n}_p \left(\tilde{c}_{yy} - 1\right), \tag{55}$$

$$\tilde{\sigma}_{xy} = \tilde{n}_p \tilde{c}_{xy} + \beta \tilde{\dot{\gamma}}, \tag{56}$$

$$2\tilde{c}_{xy}\tilde{\dot{\gamma}} = (1 - \alpha + \alpha\tilde{c}_{xx})(\tilde{c}_{xx} - 1) + \alpha\tilde{c}_{xy}\tilde{c}_{xy} + \epsilon \left(\tilde{c}_{xx} + \tilde{c}_{yy} + \tilde{c}_{zz} - 3\right)^q (\tilde{c}_{xx} - 1), \tag{57}$$

$$2\tilde{c}_{yy}\tilde{\dot{\gamma}} = (1 - \alpha + \alpha\tilde{c}_{yy})(\tilde{c}_{yy} - 1) + \alpha\tilde{c}_{xy}\tilde{c}_{xy} + \epsilon \left(\tilde{c}_{xx} + \tilde{c}_{yy} + \tilde{c}_{zz} - 3\right)^q (\tilde{c}_{yy} - 1), \tag{58}$$

$$\tilde{c}_{xy}\tilde{\dot{\gamma}} + \tilde{c}_{yy}\tilde{\dot{\gamma}} = (1 - \alpha + \alpha\tilde{c}_{yy})\tilde{c}_{xy} + \alpha\tilde{c}_{xy}(\tilde{c}_{xx} - 1) + \epsilon \left(\tilde{c}_{xx} + \tilde{c}_{yy} + \tilde{c}_{zz} - 3\right)^q \tilde{c}_{xy}. \tag{59}$$

These equations were solved using Newton's method with lower upper triangular decomposition (Press et al., 1992). The parameter values of the new model were determined by manually fitting the model to the flow curve obtained for a 10 wt/wt% (1.6 M) shear-banding polybutadiene solution (Cheng and Wang, 2012). The parameters of the

new model that have an influence on the shape of the flow curve and thus are determined by the fitting process are mobility factor $\alpha = 0.73$, ratio of the characteristic relaxation times $\varepsilon = 0.0025$, power-law parameter $q = 1.46$, and viscosity ratio $\beta = 10^{-5}$. We compare the flow curves predicted by the new model and its limiting case, i.e. the Giesekus model, with experimental data (Cheng and Wang, 2012). Fig. 13 displays the absolute value of the shear stress as a function of the Weissenberg number $Wi = \tilde{\dot{\gamma}} = \lambda_1 V/H$. The Weissenberg number is the dimensionless applied deformation rate and expresses the ratio of the elastic to viscous stresses. As the Giesekus relaxation dominates over the CCR-like term at small and medium shear rates, the predictions of the two models coincide in this flow regime. Because of the presence of the CCR-like term, our model can capture the upturn of the curve without the need for a solvent contribution. Additionally, it is worth mentioning that the CCR-like term accounts for nontrivial normal stress differences at large shear rates. In summary, the results confirm that the CCR-like term, which incorporates a power-law prefactor accounting for polymer stretch, is a good choice.

Fig. 14 shows the effects of the mobility factor α, ratio of the characteristic relaxation times ε, and the power-law parameter q on the behavior of the homogeneous flow curve. We find that the slope after the plateau is affected by the value of α (see Fig. 14(a)). For all values of α used in this study, the flow curve is monotonic. The upward slope of the plateau is the result of the coupling between the flow and the concentration, and shows that the bands have different concentrations. Increasing the value of α decreases the slope. Fig. 14(b) illustrates that parameter ε determines where the upturn of the shear stress occurs. As this parameter, i.e., the relative importance of the CCR-like term, is increased, the upturn is shifted to smaller shear rates. Fig. 14(c) shows that the slope of the shear stress is determined by power-law parameter q at large shear rates. Increasing the value of q leads to an increase in the slope. This parameter determines the influence of chain stretch, as the trace of the conformation tensor is a relative measure of this quantity.

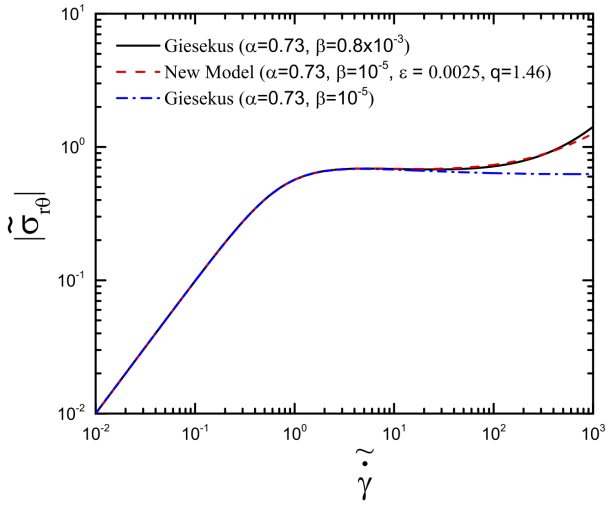

Figure 13: Influence of the CCR-like term on the homogeneous flow curve.

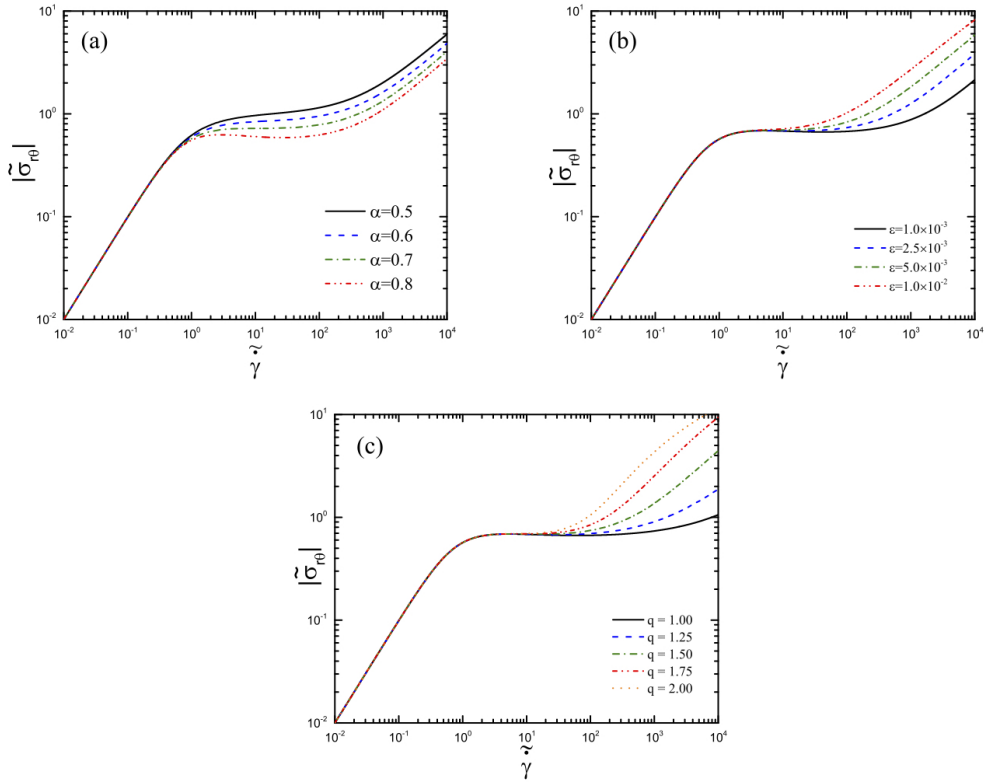

Figure 14: Effects of (a) α with $q = 1.46$ and $\varepsilon = 0.0025$, (b) ε with $\alpha = 0.73$ and $q = 1.46$, and (c) q with $\alpha = 0.73$ and $\varepsilon = 0.0025$ on the homogeneous flow curve. Parameter β was kept fixed at 10^{-5}.

3 Benchmark case no. 1: cylindrical Couette flow

3.1 Introduction

In a Couette flow, the material is between two plates which move with a relative velocity. Simple shear flow is a special case where only one component of the relative velocity vector is nonzero. In the start-up Couette flow, the relative velocity suddenly jumps from rest to the final value. The start-up flow is useful to study rheological phenomena since the molecular processes do not have enough time relative to the flow to relax, consequently they undergo microstructural changes. The dynamics in the molecular scale and inhomogeneities appear as an overshoot in the stress profile versus time in the start-up flow.

The cylindrical Couette flow also known as Taylor Couette flow is the case in which the material is placed between two coaxial cylinders rotating with relative angular velocity. The cylindrical Couette flow is a typical benchmark problem to study the behavior of viscoelastic materials. However, parallel plate configuration of the Couette flow is more intriguing due to advantages such as no curvature effect or less rod climbing. Callaghan and Gil (2000) is the only experimental work using cylindrical Couette flow for polymer solutions. They used NMR velocimetry and observed that semidilute solutions of polyacrylamide in water show shear banding.

3.2 Flow problem and nondimensionalization

In this section, we analyze the behavior of the new model in shear flow. We consider the flow in the annular gap between two concentric cylinders shown in Fig. 15. The inner cylinder rotates in the counterclockwise direction while the outer cylinder is kept stationary. The characteristic height is given as $H = R_o - R_i$, where R_o and R_i represent the radii of the outer and inner cylinders, respectively. The dimensionless curvature $q^* = (R_o - R_i)/R_i$ specifies the relative position of the cylinders. The cylindrical coordinate system was used as the reference frame with r, θ, and

z for the radial, azimuthal, and axial coordinates, respectively. Normalized coordinate $\tilde{r}^* = (r - R_i)/(R_o - R_i)$ is employed to indicate the location in the gap.

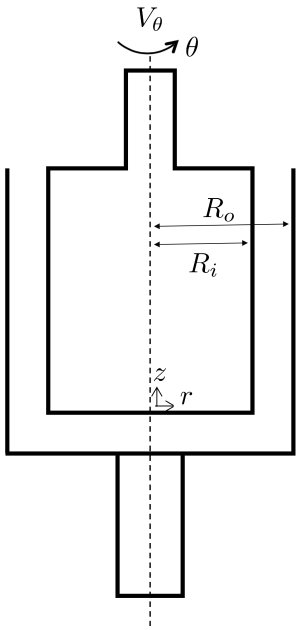

Figure 15: Schematic of the cylindrical Couette flow.

The parameters that could not be determined by fitting the steady homogeneous flow curve were estimated for the inhomogeneous flow calculations as follows. To avoid long running times, a moderate local diffusivity constant $(\tilde{D} = 10^{-3})$ was used. A moderate value of $\tilde{D}_{nonloc} = 10^{-3}$ was selected to remove the sharp kink in the banded profiles. Because inertial effects were not the main focus of this work, we simply set $E^{-1} = 10^{-5}$. The dimensionless curvature was specified as $q^* = 0.04$, which is a typical value for cylindrical Couette experiments. To observe pronounced bands, we used a large value of the molecular weight ratio of $\chi = 0.1$. As in Cheng and Wang (2012), the total initial concentration corresponded to $\mu = 0.1$.

In the following, we work with dimensionless quantities. The spatial position is scaled by the characteristic height, $\tilde{\mathbf{r}} = \mathbf{r}/H$; time is scaled by the characteristic relaxation time, $\tilde{t} = t/\lambda_1$; pressure is scaled by the plateau modulus, $\tilde{p} = p/G_0$; extra stress is scaled as $\tilde{\boldsymbol{\sigma}} = \boldsymbol{\sigma}/G_0$; and the conformation tensor associated with the polymer is scaled as $\tilde{\mathbf{c}} = (K/k_BT)\mathbf{c}$. The dimensionless parameters with respect to these scalings are the elasticity number, $E = G_0\lambda_1^2/(\rho H^2)$; the ratio of the molecular weight of the solvent to that of the polymer, $\chi = M_s/M_p$; the viscosity

ratio, $\beta = \eta_s/\eta_0$, where $\eta_0 = G_0\lambda_1$ is the zero shear viscosity; and the ratio of the two characteristic relaxation times, $\varepsilon = \lambda_1/\lambda_2$. By assuming an initially uniform polymer concentration in the flow field, the total polymer concentration can be calculated as $\mu = \tilde{n}_p^0/(\tilde{n}_p^0 + \chi\tilde{n}_s^0)$. The nondimensional diffusion coefficients are defined as $\tilde{D} = D\lambda_1/H^2$ and $\tilde{D}_{nonloc} = D_{nonloc}\lambda_1/H^2$. The nondimensionalized form of the model Eqs. (32)-(33), (37), (42)-(45) can be found in Sec. 2.3.

3.3 Numerical method

The cylindrical coordinate system is more suitable to be used for a cylindrical Couette flow. If we write the model Eqs. (32)–(33), (37), and (42)–(45) in the cylindrical coordinate system and eliminate the zero terms, we obtain:

The Cauchy momentum balance

$$E^{-1}\frac{\partial\tilde{\mathrm{v}}_\theta}{\partial\tilde{t}} = \frac{2}{\tilde{r}}\tilde{\sigma}^p_{r\theta} + \frac{\partial\tilde{\sigma}^p_{r\theta}}{\partial\tilde{r}} + \beta(\frac{\partial^2\tilde{\mathrm{v}}^s_\theta}{\partial\tilde{r}^2} + \frac{1}{\tilde{r}}\frac{\partial\tilde{\mathrm{v}}^s_\theta}{\partial\tilde{r}} - \frac{\tilde{\mathrm{v}}^s_\theta}{\tilde{r}^2}), \tag{60}$$

the time evolution equation of the polymer number density

$$\frac{\partial\tilde{n}_p}{\partial\tilde{t}} = -\tilde{\mathrm{v}}^p_r\frac{\partial\tilde{n}_p}{\partial\tilde{r}} - \tilde{n}_p\frac{\tilde{\mathrm{v}}^p_r}{\tilde{r}} - \tilde{n}_p\frac{\partial\tilde{\mathrm{v}}^p_r}{\partial\tilde{r}}, \tag{61}$$

the time evolution equations of the differential velocity

$$\begin{aligned} E^{-1}\frac{\chi\tilde{n}_s\tilde{n}_p}{(\tilde{n}_p+\chi\tilde{n}_s)^2}\left(\frac{\partial\widetilde{\Delta\mathrm{v}}_r}{\partial\tilde{t}} - \frac{\tilde{\mathrm{v}}_\theta}{\tilde{r}}\widetilde{\Delta\mathrm{v}}_\theta\right) =& \frac{\chi\tilde{n}_s}{\tilde{n}_p+\chi\tilde{n}_s}\left\{-\frac{\partial\tilde{n}_p}{\partial\tilde{r}} + \frac{\tilde{\sigma}^p_{rr}}{\tilde{r}} + \frac{\partial\tilde{\sigma}^p_{rr}}{\partial\tilde{r}} - \frac{\tilde{\sigma}^p_{\theta\theta}}{\tilde{r}}\right\} \\ &+ \frac{\tilde{n}_p}{\tilde{n}_p+\chi\tilde{n}_s}\left\{\frac{\partial\tilde{n}_s}{\partial\tilde{r}} + \beta(\frac{\partial^2\tilde{\mathrm{v}}^s_r}{\partial\tilde{r}^2} + \frac{1}{\tilde{r}}\frac{\partial\tilde{\mathrm{v}}^s_r}{\partial\tilde{r}} - \frac{\tilde{\mathrm{v}}^s_r}{\tilde{r}^2})\right\} - \tilde{D}\widetilde{\Delta\mathrm{v}}_r, \end{aligned} \tag{62}$$

$$\begin{aligned} E^{-1}\frac{\chi\tilde{n}_s\tilde{n}_p}{(\tilde{n}_p+\chi\tilde{n}_s)^2}\left(\frac{\partial\widetilde{\Delta\mathrm{v}}_\theta}{\partial\tilde{t}} + \frac{\tilde{\mathrm{v}}_\theta}{\tilde{r}}\widetilde{\Delta\mathrm{v}}_r\right) =& \frac{\chi\tilde{n}_s}{\tilde{n}_p+\chi\tilde{n}_s}\left\{\frac{2}{\tilde{r}}\tilde{\sigma}^p_{r\theta} + \frac{\partial\tilde{\sigma}^p_{r\theta}}{\partial\tilde{r}}\right\} \\ &+ \frac{\tilde{n}_p}{\tilde{n}_p+\chi\tilde{n}_s}\beta(\frac{\partial^2\tilde{\mathrm{v}}^s_\theta}{\partial\tilde{r}^2} + \frac{1}{\tilde{r}}\frac{\partial\tilde{\mathrm{v}}^s_\theta}{\partial\tilde{r}} - \frac{\tilde{\mathrm{v}}^s_\theta}{\tilde{r}^2}) - \tilde{D}\widetilde{\Delta\mathrm{v}}_\theta, \end{aligned} \tag{63}$$

the time evolution equations of the polymer conformation

$$\begin{aligned}\frac{\partial \tilde{c}_{rr}}{\partial \tilde{t}} =& -\tilde{\mathrm{v}}_r^p \frac{\partial \tilde{c}_{rr}}{\partial \tilde{r}} + 2\tilde{c}_{rr}\frac{\partial \tilde{\mathrm{v}}_r^p}{\partial \tilde{r}} - (1-\alpha+\alpha\tilde{c}_{rr})(\tilde{c}_{rr}-1) - \alpha\tilde{c}_{r\theta}\tilde{c}_{r\theta} \\ &+ \epsilon\left(\tilde{c}_{rr}+\tilde{c}_{\theta\theta}+\tilde{c}_{zz}-3\right)^q(\tilde{c}_{rr}-1) - 2\widetilde{D}_{nonloc}\tilde{c}_{r\theta}\left[\frac{1}{\tilde{r}}\frac{\partial \tilde{\sigma}_{r\theta}^p}{\partial \tilde{r}} + \frac{2}{\tilde{r}^2}\frac{\partial \tilde{\sigma}_{r\theta}^p}{\partial \tilde{r}}\right] \\ &+ 2\widetilde{D}_{nonloc}\tilde{c}_{rr}\left[\frac{\partial^2 \tilde{\sigma}_{rr}^p}{\partial \tilde{r}^2} + \frac{1}{\tilde{r}}\left(\frac{\partial \tilde{\sigma}_{rr}^p}{\partial \tilde{r}} - \frac{\partial \tilde{\sigma}_{\theta\theta}^p}{\partial \tilde{r}}\right) - \frac{1}{\tilde{r}^2}\left(\tilde{\sigma}_{rr}^p - \tilde{\sigma}_{\theta\theta}^p\right)\right],\end{aligned} \tag{64}$$

$$\begin{aligned}\frac{\partial \tilde{c}_{\theta\theta}}{\partial \tilde{t}} =& -\tilde{\mathrm{v}}_r^p \frac{\partial \tilde{c}_{\theta\theta}}{\partial \tilde{r}} - 2\tilde{c}_{r\theta}\frac{\tilde{\mathrm{v}}_\theta^p}{\tilde{r}} + 2\tilde{c}_{r\theta}\frac{\partial \tilde{\mathrm{v}}_\theta^p}{\partial \tilde{r}} + 2\tilde{c}_{\theta\theta}\frac{\tilde{\mathrm{v}}_r^p}{\tilde{r}} - (1-\alpha+\alpha\tilde{c}_{\theta\theta})(\tilde{c}_{\theta\theta}-1) - \alpha\tilde{c}_{r\theta}\tilde{c}_{r\theta} \\ &+ \epsilon\left(\tilde{c}_{rr}+\tilde{c}_{\theta\theta}+\tilde{c}_{zz}-3\right)^q(\tilde{c}_{\theta\theta}-1) \\ &+ 2\widetilde{D}_{nonloc}\tilde{c}_{r\theta}\left[\frac{\partial^2 \tilde{\sigma}_{r\theta}^p}{\partial \tilde{r}^2} + \frac{2}{\tilde{r}}\frac{\partial \tilde{\sigma}_{r\theta}^p}{\partial \tilde{r}} - \frac{2}{\tilde{r}^2}\tilde{\sigma}_{r\theta}^p\right] + 2\widetilde{D}_{nonloc}\tilde{c}_{\theta\theta}\left[\frac{1}{\tilde{r}}\frac{\partial \tilde{\sigma}_{rr}^p}{\partial \tilde{r}} + \frac{1}{\tilde{r}^2}\left(\tilde{\sigma}_{rr}^p - \tilde{\sigma}_{\theta\theta}^p\right)\right],\end{aligned} \tag{65}$$

$$\begin{aligned}\frac{\partial \tilde{c}_{r\theta}}{\partial \tilde{t}} =& -\tilde{\mathrm{v}}_r^p \frac{\partial \tilde{c}_{r\theta}}{\partial \tilde{r}} - \tilde{c}_{rr}\frac{\tilde{\mathrm{v}}_\theta^p}{\tilde{r}} + \tilde{c}_{rr}\frac{\partial \tilde{\mathrm{v}}_\theta^p}{\partial \tilde{r}} + \tilde{c}_{r\theta}\frac{\tilde{\mathrm{v}}_r^p}{\tilde{r}} + \tilde{c}_{r\theta}\frac{\partial \tilde{\mathrm{v}}_r^p}{\partial \tilde{r}} - (1-\alpha+\alpha\tilde{c}_{rr})\tilde{c}_{r\theta} - \alpha\tilde{c}_{r\theta}(\tilde{c}_{\theta\theta}-1) \\ &+ \epsilon\left(\tilde{c}_{rr}+\tilde{c}_{\theta\theta}+\tilde{c}_{zz}-3\right)^q(\tilde{c}_{r\theta}) + \widetilde{D}_{nonloc}\tilde{c}_{rr}\left[\frac{\partial^2 \tilde{\sigma}_{r\theta}^p}{\partial \tilde{r}^2} + \frac{2}{\tilde{r}}\frac{\partial \tilde{\sigma}_{r\theta}^p}{\partial \tilde{r}} - \frac{2}{\tilde{r}^2}\tilde{\sigma}_{r\theta}^p\right] \\ &+ \widetilde{D}_{nonloc}\tilde{c}_{r\theta}\left[\frac{\partial^2 \tilde{\sigma}_{rr}^p}{\partial \tilde{r}^2} + \frac{1}{\tilde{r}}\left(2\frac{\partial \tilde{\sigma}_{rr}^p}{\partial \tilde{r}} - \frac{\partial \tilde{\sigma}_{\theta\theta}^p}{\partial \tilde{r}}\right)\right] - \widetilde{D}_{nonloc}\tilde{c}_{\theta\theta}\left[\frac{1}{\tilde{r}}\frac{\partial \tilde{\sigma}_{r\theta}^p}{\partial \tilde{r}} + \frac{2}{\tilde{r}^2}\frac{\partial \tilde{\sigma}_{r\theta}^p}{\partial \tilde{r}}\right],\end{aligned} \tag{66}$$

the explicit expressions of the extra stress

$$\tilde{\sigma}_{rr} = \tilde{n}_p\left(\tilde{c}_{rr}-1\right), \tag{67}$$

$$\tilde{\sigma}_{\theta\theta} = \tilde{n}_p\left(\tilde{c}_{\theta\theta}-1\right), \tag{68}$$

$$\tilde{\sigma}_{r\theta} = \tilde{n}_p\tilde{c}_{r\theta} + \beta\left(\frac{\partial \tilde{\mathrm{v}}_\theta^s}{\partial \tilde{r}} - \frac{\tilde{\mathrm{v}}_\theta^s}{\tilde{r}}\right), \tag{69}$$

and the equations of the phase velocities

$$\tilde{\mathrm{v}}_r^p = \frac{\chi\tilde{n}_s}{\tilde{n}_p+\chi\tilde{n}_s}\widetilde{\Delta\mathrm{v}}_r, \tag{70}$$

$$\tilde{\mathrm{v}}_\theta^p = \tilde{\mathrm{v}}_\theta + \frac{\chi\tilde{n}_s}{\tilde{n}_p+\chi\tilde{n}_s}\widetilde{\Delta\mathrm{v}}_\theta, \tag{71}$$

$$\tilde{\mathrm{v}}_r^s = -\frac{\tilde{n}_p}{\tilde{n}_p+\chi\tilde{n}_s}\widetilde{\Delta\mathrm{v}}_r, \tag{72}$$

$$\tilde{\mathrm{v}}_\theta^s = \tilde{\mathrm{v}}_\theta - \frac{\tilde{n}_p}{\tilde{n}_p+\chi\tilde{n}_s}\widetilde{\Delta\mathrm{v}}_\theta. \tag{73}$$

The boundary conditions are specified as follows. The temporal evolution of the azimuthal velocity at the inner wall is specified by (Zhou et al., 2008)

$$\tilde{\mathrm{v}}_\theta(r^* = 0, \tilde{t}) = Wi \tanh(\tilde{a}\tilde{t}) \,, \tag{74}$$

where $\tilde{a}$ is the dimensionless ramp rate of the rheometer. To avoid long running times, a fast ramp rate $(\tilde{a} = 100)$ was used. Typically, $\tilde{a}$ lies in the range of $O(10^0$–$10^2)$. Note that the azimuthal velocity at the inner cylinder corresponds to the apparent shear rate across the gap at steady state (Zhou et al., 2008), i.e., $\tilde{\dot{\gamma}}_{app} = Wi$. The outer cylinder is assumed to be stationary; therefore, we set $\widetilde{v}_\theta(r^* = 1) = 0$. No flow through the walls is specified by setting the normal components of the total and differential velocities equal to zero $(\widetilde{v}_r = \widetilde{\Delta v}_r = 0)$. To specify no-slip along the walls, the tangential component of the differential velocity must vanish at the boundaries $(\widetilde{\Delta v}_\theta = 0)$.

The flow problem was solved using the numerical procedure employed in Germann et al. (2011, 2014, 2016). We used a Chebyshev pseudospectral collocation method (Voigt et al., 1994; Peyret, 2002) with $N_1 = 200$ collocation points for spatial discretization and a second-order Crank-Nicolson scheme (Richtmyer and Morton, 1967) with an adaptive time step for temporal discretization. The advantage of this scheme is since both the known and unknown values are used, the cost and stability are compromised between the explicit and implicit methods. The nonlinear system of the discretized algebraic equations was iteratively solved at each time step by using an inverse-based multilevel incomplete lower upper (ILU) preconditioned Newton-Krylov solver (Germann et al., 2011). The Newton method is used to linearize the coupled equation; the Krylov subspace-based method was applied to solve the resulting system iteratively. The key feature of the inverse-based multilevel ILU preconditioner is that the magnitude of the preconditioned coefficient matrix perturbations with respect to the identity matrix can be controlled by adjusting the magnitude of the inverse triangular factors during the construction of the coefficient matrix. The theoretical details of this special ILU preconditioner can be found in Bollhöfer and Saad (2006) and Bollhöfer et al. (2008).

To check the convergence of the numerical calculations, we repeated the simulation obtained for $Wi = 10$ with $N_2 = 150$ and $N_3 = 250$ collocation points. For each grid of collocation points, the solution was computed at 100 different radial positions that were equally spaced across the cylindrical gap. The error between the state variables computed on grids $N_1 = 200$ and those computed on grids N_2 and N_3 was never larger than 8.23×10^{-6}. If the values were larger than unity, the relative error was considered, otherwise, the absolute error was taken into account (Ascher and Greif, 2011).

3.4 Results

Figs. 16(a) and (b) display the effect of the Weissenberg number on the steady-state profiles of the total azimuthal velocity and polymer number density, respectively. The velocity profile shows two distinct shear bands for the range $3 \lessapprox Wi \lessapprox 63$. Increasing the Weissenberg number moves the kink separating the two bands from the rotating inner wall to the stationary outer wall. Because of the two-fluid coupling between flow and concentration, the profile of the polymer number density is also banded. Note that the total mass/number density of the polymeric solution is assumed to be constant, whereas the individual mass/number densities are allowed to vary. This is in contrast to the predictions obtained for one-fluid polymer models, which do not take diffusional effects into account. Moreover, we find that the curvature of the cylindrical Couette geometry justifies the curved profile of the polymer number density.

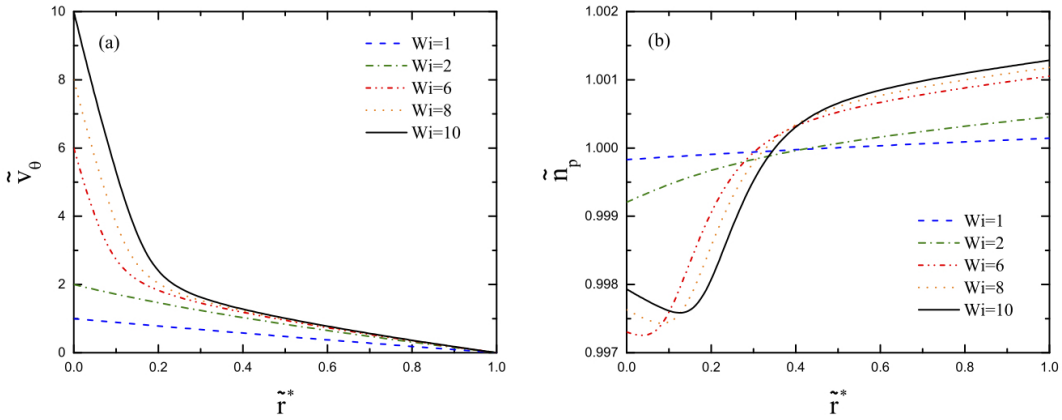

Figure 16: Profiles of the (a) velocity and (b) polymer number density calculated for different Weissenberg numbers. The values of the other model parameters used in the calculation are $\alpha = 0.73$, $\varepsilon = 2.5 \times 10^{-3}$, $q = 1.46$, $\beta = 10^{-5}$, $E^{-1} = 10^{-5}$, $\tilde{D} = \tilde{D}_{nonloc} = 10^{-3}$, $\chi = 0.1$, and $\mu = 0.1$.

Steady-state profiles of the nontrivial stress components are shown across the cylindrical gap in Figs. 17(a)-(c) for different values of the Weissenberg number. The magnitudes of these components are larger for greater Weissenberg numbers. As required by the relatively small gap and the Cauchy momentum balance in Eq. (32), the absolute value of the shear stress reduces linearly from the inner rotating wall to the outer stationary wall (see Fig. 17(a)). The profiles of the $rr-$ and $\theta\theta$-components of the stress tensor are given in Figs. 17(b) and (c),

respectively. As expected, the $\theta\theta$-component is much larger in magnitude than the rr-component. In the nonlinear regime, the strong nonlinearities in these two profiles are related to shear banding. Furthermore, we note that the zz-component is identically zero. Daprà and Scarpi (2015) analytically solved the Giesekus model for steady cylindrical Couette flow and investigated the spatial behavior of the nontrivial stress components in the gap. In their work, the value of α was restricted to $\alpha < 0.5$, as the Giesekus model does not have a real physical solution outside this range for high Weissenberg numbers (Yoo and Choi, 1989; Schleiniger and Weinacht, 1991). By adding a large solvent contribution or a second nonlinear relaxation term, this limitation can be overcome.

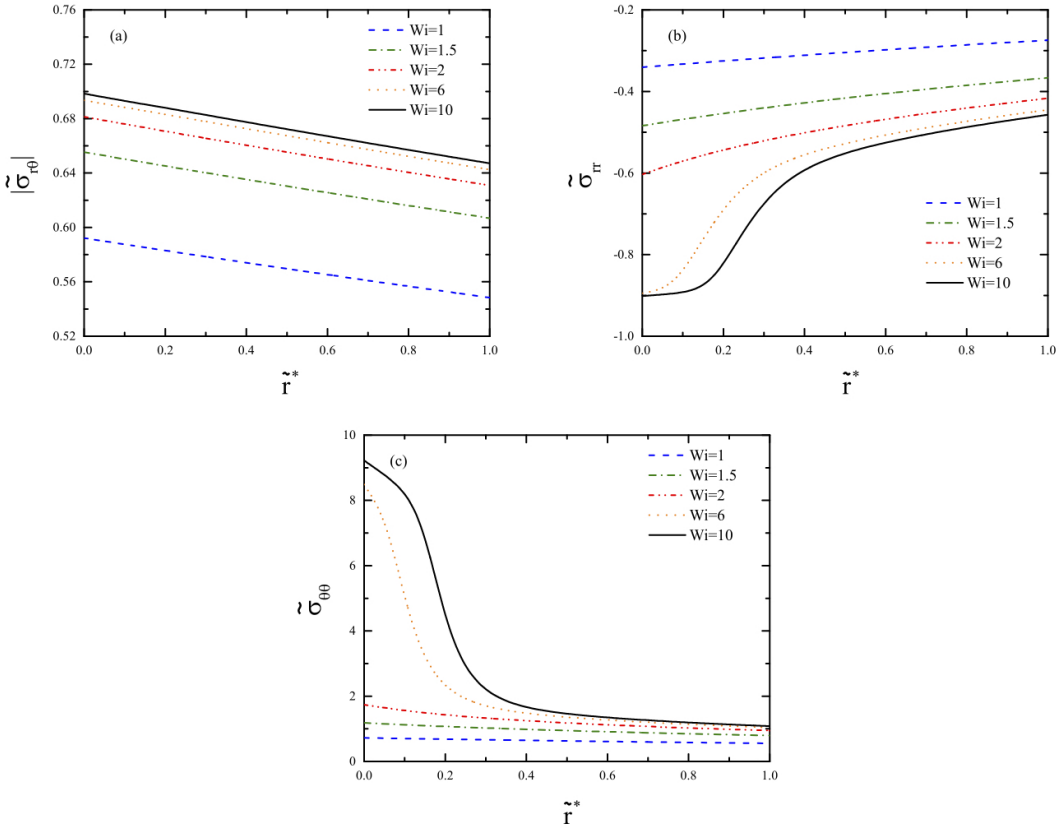

Figure 17: Profiles of the (a) shear stress, (b) radial stress, and (c) tangential stress across the cylindrical gap calculated for different values of the Weissenberg number. The other model parameters are the same as those given in the caption of Fig. 16.

Fig. 18(a) and (b) display the profiles of the first and second normal stress differences, respectively, across the gap width for different Weissenberg numbers. As the first normal stress differences is defined as $N_1 = \tilde{\sigma}_{\theta\theta} - \tilde{\sigma}_{rr}$, Fig. 18(a) is obtained by subtracting the results shown in Fig. 17(b) from those shown in Fig. 17(c). Furthermore, as the zz-component is identically zero, the results of the second normal stress difference, $N_2 = \tilde{\sigma}_{rr} - \tilde{\sigma}_{zz}$, are exactly the same as those depicted in Fig. 17(b).

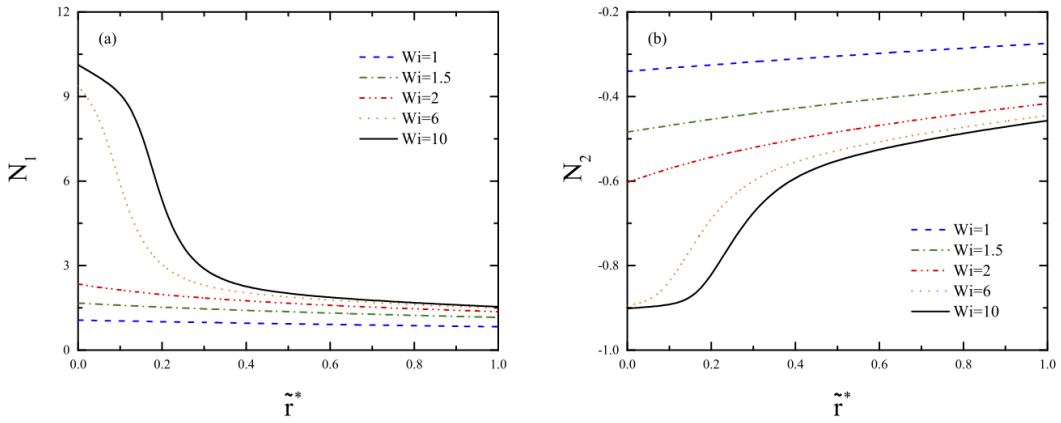

Figure 18: Profiles of the (a) first and (b) second normal stress differences across the cylindrical gap calculated for different values of the Weissenberg number. The other model parameters are the same as those given in the caption of Fig. 16.

Fig. 19 shows the influence of the stress-induced migration on the steady-state profile of the polymer number density. The calculation was performed with and without the term accounting for stress-induced migration. The horizontal line indicates that without this term, the polymer number density is nearly constant across the cylindrical gap. Stress-induced migration is clearly responsible for the formation of the shear bands. As we used homogeneous initial conditions, standard Fickian diffusion has no significant effect.

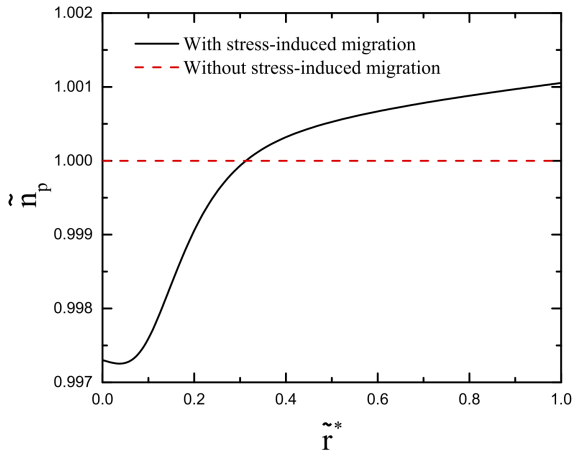

Figure 19: Number density of the polymer calculated for the model with and without the term corresponding to stress-induced migration. The values of the model parameters used in the calculation are $\alpha = 0.73$, $\varepsilon = 2.5 \times 10^{-3}$, $q = 1.46$, $\beta = 10^{-5}$, $E^{-1} = 10^{-5}$, $\tilde{D} = \tilde{D}_{nonloc} = 10^{-3}$, $\chi = 0.1$, $\mu = 0.1$, and $Wi = 6$.

Fig. 20 displays the effects of the total polymer concentration and ratio of the solvent molecular weight to the polymer molecular weight on the steady-state profile of the polymer number density. As expected from experiments (Wang et al., 2011; Jaradat et al., 2012), Fig. 20(a) shows that increasing the total polymer concentration causes the shear bands to be more pronounced. This is because the polymer concentration appears in the expression for the extra stress provided in Eq. (43). Consequently, larger polymer concentrations cause a greater extra stress and thus more shear-induced migration. At this early stage of the work, we did not consider any functional dependencies of the material parameters. Laboratory experiments will have to be conducted in a future study to work out some of these scaling laws, such as the effect of the polymer concentration on mobility factor α.

Fig. 20(b) shows that increasing the molecular weight ratio leads to more pronounced shear bands. However, experimental data show the opposite trend (Wang et al., 2011; Jaradat et al., 2012). This discrepancy can be explained by the fact that as the parameters determining the shape of the flow curve are fixed, the results displayed in Fig. 20(b) only provide information about the impact of the molecular weight ratio on the diffusional processes. Experimental studies on shear banding have observed values for χ of $O(10^{-5})$ (Jaradat et al., 2012). To observe pronounced effects, we decided to continue with the rather large value of $\chi = 0.1$.

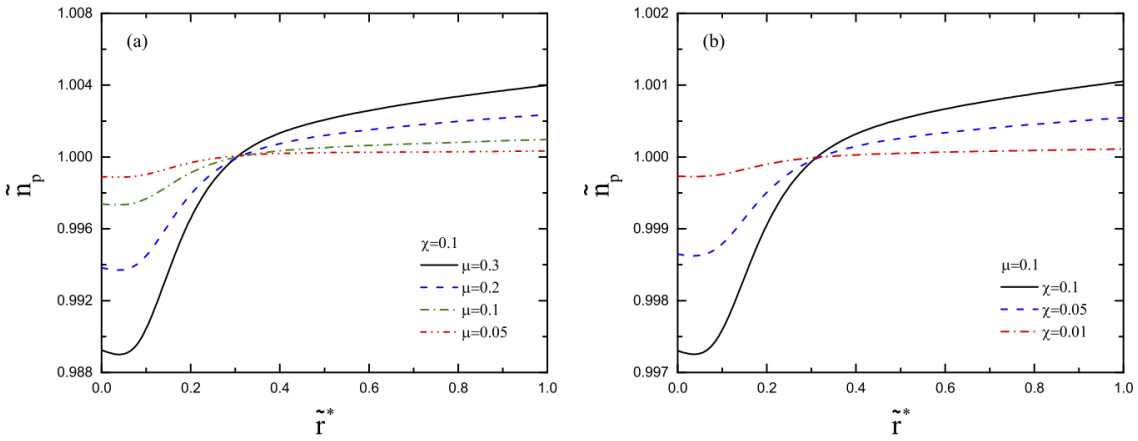

Figure 20: Influences of the (a) total polymer concentration and (b) molecular weight ratio on the number density of the polymer. The other model parameters are the same as those given in the caption of Fig. 19.

Fig. 21 displays the influence of the local diffusivity constant. The steady-state profile of the polymer number density (see Fig. 21(a)) was found to be independent of the local diffusivity constant. As opposed to Cromer et al.'s model (Cromer et al., 2013a), our model predicts a steady-state solution whose smoothness is not affected by this parameter. In Fig. 21(b), we display the transient evolution of the absolute value of the wall shear stress. For a sufficiently high ramp rate, the nonlinear Giesekus relaxation generates an overshoot that triggers shear band formation. A smaller value for the diffusivity constant increases the time to reach steady state. As the flow curve is monotonic and the shear stress is determined by Cauchy momentum balance Eq. (32), the local diffusivity constant does not have a significant effect on the shear stress. However, some differences can be observed in the microstructural quantities (see Figs. 21(c) and (d)). For $\tilde{D} = 0.001$ shown in Fig. 21(c), up to $\tilde{t} = 50$, the transient profiles of the polymer number density intersect at a unique position in the gap where the shear bands separate. Thereafter, nonlocal stress diffusion pushes the kink toward the outer cylinder.

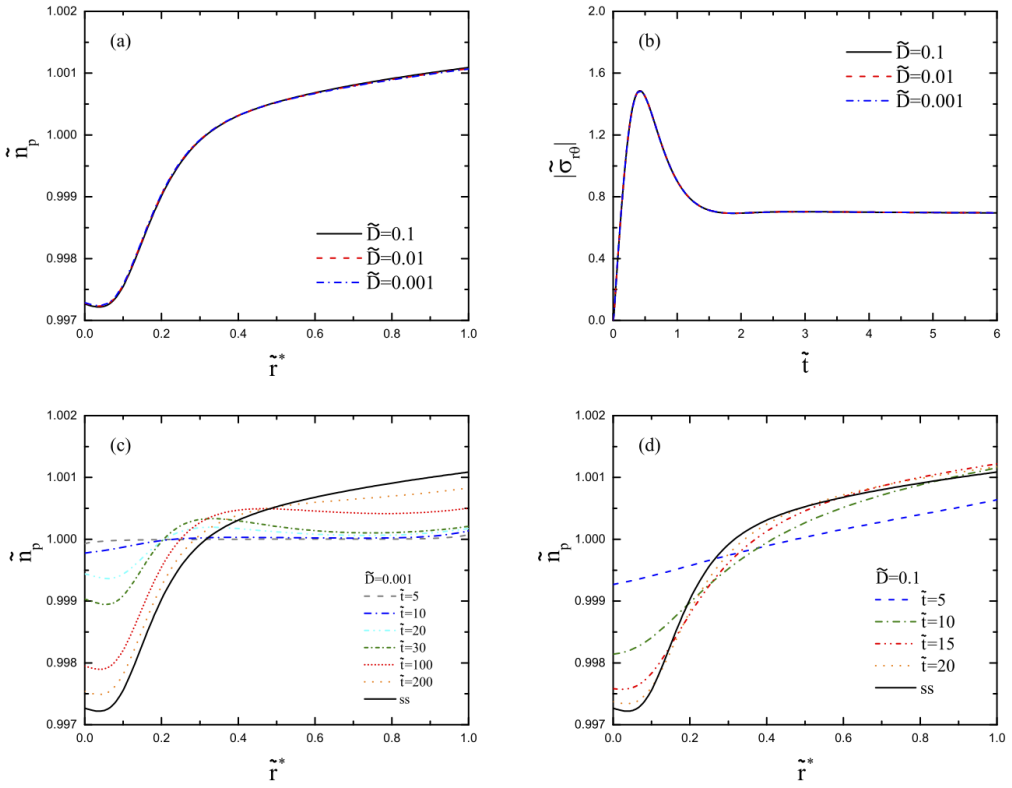

Figure 21: Effect of the local diffusivity constant on (a) the steady-state profile of the polymer number density, (b) the temporal behavior of the absolute value of the shear stress at the inner wall, and (c) and (d) the temporal behavior of the polymer number density profile in the cylindrical gap. The other model parameters are the same as those given in the caption of Fig. 19.

Fig. 22 shows the temporal evolution of the radial component of the differential velocity in the cylindrical gap width. We find that this component increases to a maximum and then decreases to zero as steady state is achieved. Note that the azimuthal component is of much smaller magnitude and therefore does not have an effect on the computational results. The profile of the radial component is different to predictions of a two-fluid model for shear-banding wormlike micelles (Germann et al., 2016). As this model is based on the assumption that the wormlike micelles form shear bands as a result of their dynamic breakage, the radial velocity develops a local extremum at the transition region of the shear bands.

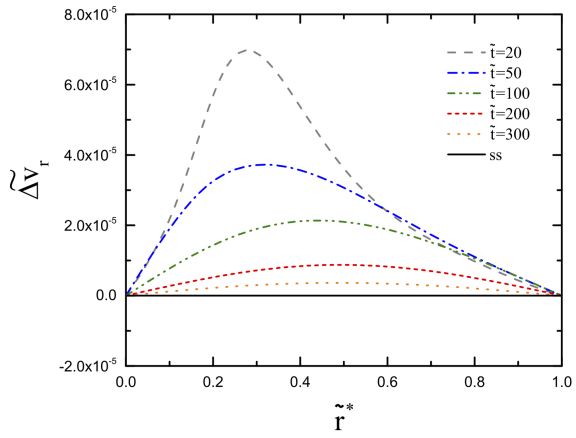

Figure 22: Temporal evolution of the radial component of the differential velocity across the gap width calculated with $Wi = 10$. The other model parameters are the same as those given in the caption of Fig. 19.

Fig. 23 shows the effect of the nonlocal diffusivity constant on the velocity profile. The speciality of our two-fluid model is that the smoothness of the profiles is controlled solely by this parameter. We find that a larger value of $\tilde{D}_{nonloc}$ leads to a smoother steady-state solution. Although the uniqueness of the solution is guaranteed here even if $\tilde{D}_{nonloc} = 0$, there may well be a parameter space where this may be the case.

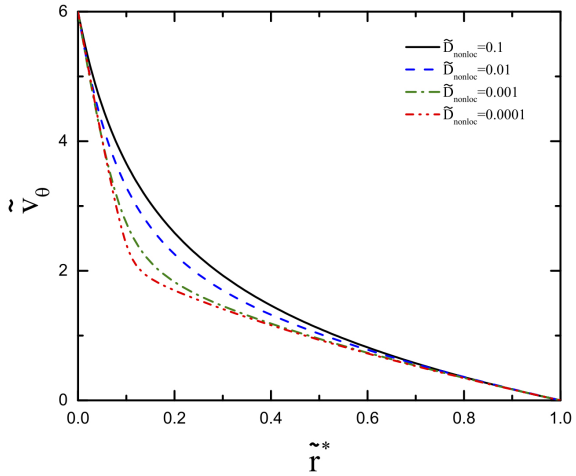

Figure 23: Effect of the nonlocal diffusivity constant on the steady-state profile of the velocity. The other model parameters are the same as those given in the caption of Fig. 19.

Figs. 24(a) and (b) show the impact of the deformation history and initial condition, respectively, on the steady-state profile of the polymer number density. To investigate the influence of deformation history, we performed some ramp-up and ramp-down tests. We started the ramp-up test from rest; for the ramp-down test, the steady-state solution at $Wi = 100$ was used as the initial condition. The terminal value of Wi was specified to be six. We find that the steady-state solution displayed in Fig. 24(a) is independent of the deformation history. To examine the impact of the initial condition, we started the simulation using an initial polymer density perturbed by $\tilde{n}_p = 1 + k_1 cos(\pi k_2 y/(R_o - R_i))$ with a magnitude of $k_1 = 10^{-3}$ and two wave numbers of $k_2 = 1$ and $k_2 = 5$. Fig. 24(b) shows that the different initial conditions evolved into a unique steady-state profile. As in the model of Cromer et al. (2013a) and as observed in experiments (Cheng and Wang, 2012), our model is capable of predicting a unique banded steady state that is independent of the initial condition and the applied deformation history.

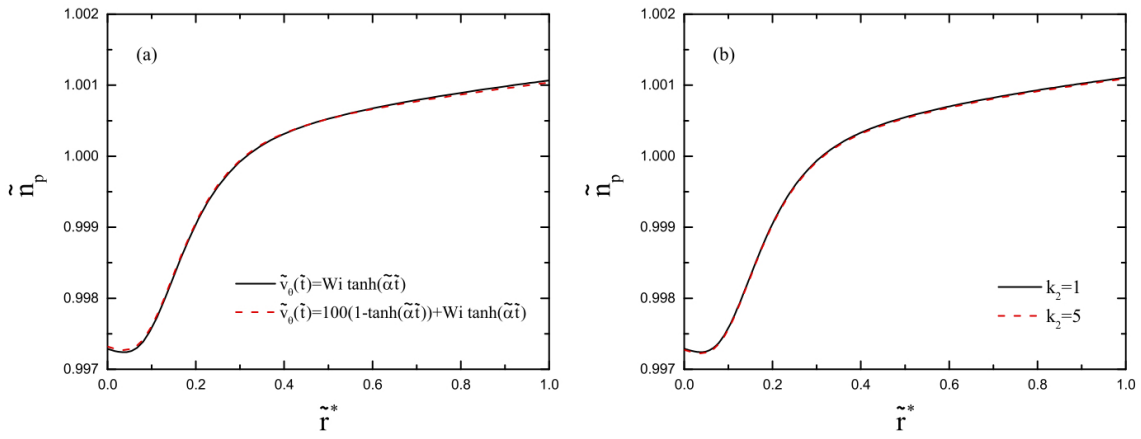

Figure 24: (a) Steady-state profiles of the polymer number density calculated using different deformation histories where ramp-up ($\tilde{v}_\theta(\tilde{t}) = Wi\tanh(\tilde{a}\tilde{t})$) and ramp-down ($\tilde{v}_\theta(\tilde{t}) = 100(1-\tanh(\tilde{a}\tilde{t})) + Wi\tanh(\tilde{a}\tilde{t})$) conditions were applied. The terminal value of Wi was set to six. (b) Steady-state profiles of the polymer number density calculated using differently perturbed initial conditions. The model parameters are the same as those given in the caption of Fig. 19.

3.5 Conclusion

We solved a cylindrical Couette flow to investigate the general behavior of the new model. We found that the steady-state solution is unique for different initial conditions and independent of the applied deformation history. Furthermore, the value of the local diffusivity constant has no significant effect on the steady-state solution. In agreement with the experiments of Callaghan and Gil (2000), velocity and concentration banding is predicted. Furthermore, we observed that stress-induced migration is responsible for shear band formation.

4 Benchmark case no. 2: pressure-driven channel flow

4.1 Introduction

In this section, we analyze the behavior of our model comprising time evolution Eqs. (32)–(33), (37), (42), the explicit expression of the extra stress tensor provided in Eq. (43), and the explicit expressions of the phase velocities provided in Eqs. (44)–(45) in a pressure-driven channel flow.

A rectilinear channel has simple geometry, which makes its flow problem a suitable benchmark problem for constitutive models and newly developed codes. Exact analytical solutions for a fully developed channel flow have been derived for various well-known differential viscoelastic fluid models, including the linearized and exponential forms of Phan-Thien-Tanner (PTT) (Oliveira and Pinho, 1999; Alves et al., 2001; Cruz et al., 2005), Giesekus (Yoo and Choi, 1989; Schleiniger and Weinacht, 1991), and Johnson-Segalman (Van Schaftingen and Crochet, 1985) models. For instance, Oliveira and Pinho (1999) found that the shear-thinning behavior reduces the wall shear stress and makes the velocity profiles flatter. Cruz et al. (2005) investigated the effect of a nontrivial Newtonian solvent viscosity and observed that the spatial variation of the velocity field can be made flatter by increasing the ratio of the solvent viscosity to the total viscosity. In addition, the UCM and Oldroyd-B models were analytically solved for a transient pressure-driven channel flow. They are now extensively used for validation purposes (Waters and King, 1970). Depending on the choice of the model parameters, viscoelastic fluid models can exhibit intense temporal oscillations. Damped inertio-elastic shear waves travel across the channel and reflect back from the stationary walls. Duarte et al. (2008) found that the transient response is longer for larger elasticity numbers, and the frequency of the oscillations is higher. Furthermore, shear-thinning reduced the time required to reach a steady state. The presence of a large Newtonian solvent contribution leads to a smaller oscillatory frequency of the response as well as an attenuation of the oscillation peak (Xue et al., 2004; Van Os and Phillips, 2004; Duarte

et al., 2008). Slip along the channel is important, as it is widely observed under strong deformations of viscoelastic materials. Meanwhile, Ferrás et al. (2012) analytically solved the Giesekus model and a simplified version of the PTT model under linear and nonlinear Navier, Hatzikiriakos, and asymptotic slip conditions. They showed that a unique steady-state solution always exists for the four phenomenological slip models considered for a simplified PTT model. For the Giesekus model, the existence of the solution can be numerically proven for some cases with slip if no physical solution exists because of the Weissenberg number restrictions in the no-slip condition.

Shear banding, which is defined as localized bands with different shear rates, is ubiquitously observed in soft materials. However, its underlying mechanisms are not always the same. While the shear banding instability of wormlike micelles is caused by a combination of reptation and micellar breakage, that of semidilute polymers is still an open issue of debate. Shear banding in complex fluids is reviewed in Olmsted (2008), Manneville (2008), Divoux et al. (2016), and Germann (2019). Several experimental studies focused on the shear banding phenomenon in Poiseuille flows. PIV experiments performed on wormlike micelles in microchannels (Kim et al., 2016), regular channels (Marín-Santibáñez et al., 2006), and capillaries (Méndez-Sánchez et al., 2003; Yamamoto et al., 2008) revealed that a spurt is evident in the rapid increase in the velocity or flow rate at the critical pressure gradient. The velocity profiles exhibit Newtonian behavior at low shear rates. Some systems form an apparent slip below the onset of the spurt. Kim et al. (2016) noted that the recorded slip velocity may be an artifact of very thin shear-banding layers near the walls, which are too thin to be optically resolved. The velocity changes from a parabolic profile to a plug-like one during the transition to the shear banding regime. Furthermore, the interface between the shear bands was spatially undulating (Nghe et al., 2010). Experimental evidence also suggests that the velocity profile of colloidal particles shows a plug-like shape as a result of shear-induced migration (Frank et al., 2003). By performing PIV in microchannels, Degré et al. (2006) observed that the maximum velocity for shear-thinning, non-shear-banding polymer solutions superlinearly increases with the applied pressure gradient in the nonlinear viscoelastic regime. The velocity profile slightly departs from the parabolic profile of the Newtonian fluids and exhibits a depletion layer in the micrometer range. The flow curve of the polymer melts shows a spurt and hysteresis in pressure-driven experiments. The wall slip in polymer melts, particularly, is extensively studied because of its potential influence on extrusion instabilities (Denn, 2001). The extent to which semidilute entangled polymer solutions exhibit the above-described phenomena is currently unclear because of the lack of experimental data.

McLeish and Ball (1986) conducted the very first numerical study that relates the spurt in a Poiseuille flow to the shear banding phenomenon. They used an improved version of the Doi-Edwards model, which also incorporates stress

contributions with shorter relaxation times than the reptation time of a single polymer chain, to capture the rheology of monodisperse polymer melts. This model exhibits a nonmonotonic steady flow curve under homogeneous flow conditions. Hence, they were able to capture the hysteresis loops in the profile of the volumetric flow rate plotted against the applied pressure gradient. Radulescu and Olmsted (2000) also published an early work on shear banding using nonlocal stress diffusive terms. Two distinct shear bands were found below the critical point of monotonicity for the Johnson-Segalman model in the case of an inertialess Poiseuille flow. Many years later, Fielding and Wilson (2010) performed a fully nonlinear stability analysis of the same model in a pressure-driven channel flow. They applied small perturbations in the flow/flow-gradient plane and flow-gradient/vorticity plane and showed that the initially flat interface was unstable with respect to the growth of undulations along it. The Vasquez-Cook-McKinley (VCM) two-species model for wormlike micelles was also examined (Cromer et al., 2011b). The authors showed an onset of shear and concentration banding above a critical pressure gradient. The interface between the bands initially forms near the walls, and then moves toward the center. The VCM model predicts a jump in the volumetric flow rate at the critical pressure drop and hysteresis, as experimentally observed for wormlike micelles. Subsequently, these authors investigated the linear stability of the VCM model and suggested that the spectrum of the unstable modes is reduced if the interface between the bands is smoothed by using a larger diffusivity constant or smaller characteristic channel dimensions (Cromer et al., 2011a). Thus far, shear banding in pressure-driven flows has only been predicted for one-fluid viscoelastic constitutive models showing a nonmonotonic homogeneous flow curve. Such models are well-known to be unable to predict steady-state bands if the curve is strictly monotonic. Therefore, a more complex two-fluid model, such as the one used in the present work, is required to examine the shear banding instability of semidilute entangled polymer solutions (Moorcroft and Fielding, 2013, 2014). Ianniruberto et al. (1994) solved Doi and Milners' two-fluid theory for semidilute entangled polymer solutions for a pressure-driven channel flow. They found stress-induced migration of the polymers toward the center. However, their predictions were limited to pressure gradients smaller than the shear banding regime.

4.2 Flow problem and nondimensionalization

In this section, we investigate our model in a rectilinear channel flow driven by a pressure gradient. We consider a one-dimensional Poiseuille flow through a straight channel. Fig. 25 shows a schematic of the problem, where H and L denote the height and length of the channel, respectively. The inlet and outlet effects can be neglected because we assume $H \ll L$. Furthermore, any dependence on the z-direction is ignored. The Cartesian coordinate system is used as the reference frame with origin at the centerline. The walls are kept stationary, whereas a nonzero pressure

gradient Δp is applied in the x-direction.

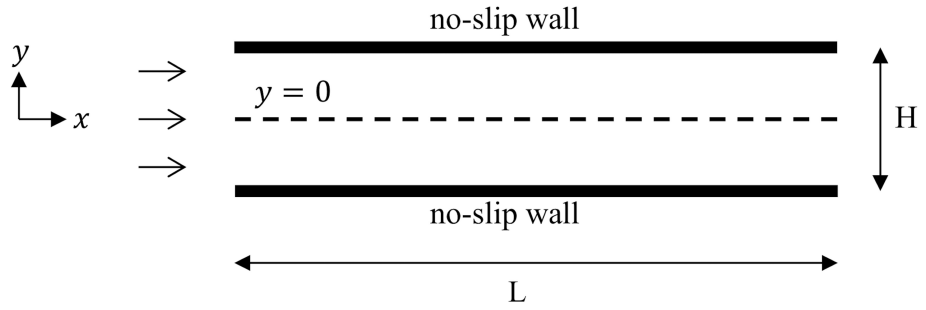

Figure 25: Two-dimensional rectilinear channel flow driven by a pressure gradient.

We work with dimensionless quantities, hereafter. The location across the gap is scaled by the channel height, $\tilde{\mathbf{y}} = \mathbf{y}/H$. Time is scaled by the characteristic relaxation time, $\tilde{t} = t/\lambda_1$. The extra stress is scaled as $\tilde{\boldsymbol{\sigma}} = \boldsymbol{\sigma}/G_0$, while the conformation tensor associated with the polymer is scaled as $\tilde{\mathbf{c}} = (K/k_BT)\mathbf{c}$. The polymer and solvent number densities are normalized using the values at the equilibrium state as $\tilde{n}_p = n_p/n_p^0$ and $\tilde{n}_s = n_s/n_p^0$, respectively. The dimensionless parameters with respect to these scalings are the pressure gradient $\tilde{P}_{\mathrm{x}} = \Delta pH/(LG_0)$; elasticity number, $E = G_0\lambda_1^2/(\rho H^2)$; ratio of the molecular weight of the solvent to that of the polymer, $\chi = M_s/M_p$; viscosity ratio, $\beta = \eta_s/\eta_0$, where $\eta_0 = G_0\lambda_1$ is the zero shear viscosity; boundary layer constant $\tilde{\xi} = \eta_{extra}/\eta_0$; and ratio of the characteristic relaxation times, $\epsilon = \lambda_1/\lambda_2$. By assuming an initially uniform polymer concentration in the flow field, the total polymer concentration corresponds to the initial local polymer concentration, and is, thus, given in weight percent by $\mu = \tilde{n}_p^0/(\tilde{n}_p^0 + \chi\tilde{n}_s^0)$. The dimensionless diffusion coefficients are defined as $\tilde{D} = D\lambda_1/H^2$ and $\tilde{D}_{nonloc} = D_{nonloc}\lambda_1/H^2$. The dimensionless form of the model equations can be found in Sec. 2.3.

4.3 Numerical method

We used the Cartesian coordinate system to solve the rectilinear channel flow. If we write the model Eqs. (32)–(33), (37), and (42)–(45) in this system and keep only the nonzero terms, we have:

The Cauchy momentum balance

$$E^{-1}\frac{\partial\tilde{\mathrm{v}}_x}{\partial\tilde{t}} = -\widetilde{P} + \frac{\partial\tilde{\sigma}_{xy}}{\partial\tilde{y}}, \tag{75}$$

the time evolution equation of the polymer number density

$$\frac{\partial \tilde{n}_p}{\partial \tilde{t}} = -\tilde{\mathrm{v}}_y^p \frac{\partial \tilde{n}_p}{\partial \tilde{y}} - \tilde{n}_p \frac{\partial \tilde{\mathrm{v}}_y^p}{\partial \tilde{y}}, \tag{76}$$

the time evolution equations of the differential velocity

$$E^{-1} \frac{\chi \tilde{n}_s \tilde{n}_p}{\left(\tilde{n}_p + \chi \tilde{n}_s\right)^2} \frac{\partial \widetilde{\Delta \mathrm{v}}_x}{\partial \tilde{t}} = \frac{\chi \tilde{n}_s}{\tilde{n}_p + \chi \tilde{n}_s} \frac{\partial \tilde{\sigma}_{xy}^p}{\partial \tilde{y}} + \beta \frac{\tilde{n}_p}{\tilde{n}_p + \chi \tilde{n}_s} \frac{\partial^2 \tilde{\mathrm{v}}_x^s}{\partial \tilde{y}^2} - \tilde{D} \widetilde{\Delta \mathrm{v}}_y, \tag{77}$$

$$E^{-1} \frac{\chi \tilde{n}_s \tilde{n}_p}{\left(\tilde{n}_p + \chi \tilde{n}_s\right)^2} \frac{\partial \widetilde{\Delta \mathrm{v}}_y}{\partial \tilde{t}} = \frac{\chi \tilde{n}_s}{\tilde{n}_p + \chi \tilde{n}_s} \left\{ -\frac{\partial \tilde{n}_p}{\partial y} + \frac{\partial \tilde{\sigma}_{yy}^p}{\partial \tilde{y}} \right\} + \frac{\tilde{n}_p}{\tilde{n}_p + \chi \tilde{n}_s} \left\{ \frac{\partial \tilde{n}_s}{\partial y} + \beta \frac{\partial^2 \tilde{\mathrm{v}}_y^s}{\partial \tilde{y}^2} \right\} - \tilde{D} \widetilde{\Delta \mathrm{v}}_y, \tag{78}$$

the explicit expressions of the extra stress

$$\tilde{\sigma}_{xx} = \tilde{n}_p \left(\tilde{c}_{xx} - 1 \right), \tag{79}$$

$$\tilde{\sigma}_{yy} = \tilde{n}_p \left(\tilde{c}_{yy} - 1 \right), \tag{80}$$

$$\tilde{\sigma}_{xy} = \tilde{n}_p \tilde{c}_{xy} + \beta \frac{\partial \tilde{\mathrm{v}}_x^s}{\partial \tilde{y}}, \tag{81}$$

the equations of the phase velocities

$$\tilde{\mathrm{v}}_x^p = \tilde{\mathrm{v}}_x + \frac{\chi \tilde{n}_s}{\tilde{n}_p + \chi \tilde{n}_s} \widetilde{\Delta \mathrm{v}}_x, \tag{82}$$

$$\tilde{\mathrm{v}}_y^p = \frac{\chi \tilde{n}_s}{\tilde{n}_p + \chi \tilde{n}_s} \widetilde{\Delta \mathrm{v}}_y, \tag{83}$$

$$\tilde{\mathrm{v}}_x^s = \tilde{\mathrm{v}}_x - \frac{\tilde{n}_p}{\tilde{n}_p + \chi \tilde{n}_s} \widetilde{\Delta \mathrm{v}}_x, \tag{84}$$

$$\tilde{\mathrm{v}}_y^s = - \frac{\tilde{n}_p}{\tilde{n}_p + \chi \tilde{n}_s} \widetilde{\Delta \mathrm{v}}_y, \tag{85}$$

and the time evolution equations of the polymer conformation

$$\frac{\partial \tilde{c}_{xx}}{\partial \tilde{t}} = -\tilde{\mathrm{v}}_y^p \frac{\partial \tilde{c}_{xx}}{\partial \tilde{y}} + 2\tilde{c}_{xy}\frac{\partial \tilde{\mathrm{v}}_x^p}{\partial \tilde{y}} - (1-\alpha+\alpha\tilde{c}_{xx})(\tilde{c}_{xx}-1) - \alpha\tilde{c}_{xy}\tilde{c}_{xy} - \epsilon\left(\tilde{c}_{xx}+\tilde{c}_{yy}+\tilde{c}_{zz}-3\right)^q(\tilde{c}_{xx}-1) + 2\widetilde{D}_{nonloc}\,\tilde{c}_{xy}\frac{\partial^2\tilde{\sigma}_{yx}^p}{\partial\tilde{y}^2}, \tag{86}$$

$$\frac{\partial \tilde{c}_{yy}}{\partial \tilde{t}} = -\tilde{\mathrm{v}}_y^p \frac{\partial \tilde{c}_{yy}}{\partial \tilde{y}} + 2\tilde{c}_{yy}\frac{\partial \tilde{\mathrm{v}}_y^p}{\partial \tilde{y}} - (1-\alpha+\alpha\tilde{c}_{yy})(\tilde{c}_{yy}-1) - \alpha\tilde{c}_{xy}\tilde{c}_{xy} - \epsilon\left(\tilde{c}_{xx}+\tilde{c}_{yy}+\tilde{c}_{zz}-3\right)^q(\tilde{c}_{yy}-1) + 2\widetilde{D}_{nonloc}\,\tilde{c}_{yy}\frac{\partial^2\tilde{\sigma}_{yy}^p}{\partial\tilde{y}^2}, \tag{87}$$

$$\frac{\partial \tilde{c}_{xy}}{\partial \tilde{t}} = -\tilde{\mathrm{v}}_y^p \frac{\partial \tilde{c}_{xy}}{\partial \tilde{y}} + \tilde{c}_{xy}\frac{\partial \tilde{\mathrm{v}}_y^p}{\partial \tilde{y}} + \tilde{c}_{yy}\frac{\partial \tilde{\mathrm{v}}_x^p}{\partial \tilde{y}} - (1-\alpha+\alpha\tilde{c}_{yy})\tilde{c}_{xy} - \alpha\tilde{c}_{xy}(\tilde{c}_{xx}-1) - \epsilon\left(\tilde{c}_{xx}+\tilde{c}_{yy}+\tilde{c}_{zz}-3\right)^q\tilde{c}_{xy} + \widetilde{D}_{nonloc}\left(\tilde{c}_{yy}\frac{\partial^2\tilde{\sigma}_{yx}^p}{\partial\tilde{y}^2} + \tilde{c}_{xy}\frac{\partial^2\tilde{\sigma}_{yy}^p}{\partial\tilde{y}^2}\right). \tag{88}$$

The flow problem can be solved only for the upper half of the channel to avoid unnecessary computations because the flow is symmetric with respect to the centerline. The symmetry of the state variables can be guaranteed by using the following conditions:

$$\frac{\partial \tilde{\mathrm{v}}_\mathrm{x}}{\partial \tilde{\mathrm{y}}} = \frac{\partial \widetilde{\Delta \mathrm{v}}_\mathrm{x}}{\partial \tilde{\mathrm{y}}} = \frac{\partial \widetilde{\Delta \mathrm{v}}_\mathrm{y}}{\partial \tilde{\mathrm{y}}} = \frac{\partial \tilde{c}_\mathrm{xx}}{\partial \tilde{\mathrm{y}}} = \frac{\partial \tilde{c}_\mathrm{yy}}{\partial \tilde{\mathrm{y}}} = \frac{\partial \tilde{c}_{zz}}{\partial \tilde{\mathrm{y}}} = \frac{\partial \tilde{n}_p}{\partial \tilde{\mathrm{y}}} = 0 \quad \text{at} \quad \tilde{\mathrm{y}} = 0, \tag{89}$$

$$\tilde{c}_\mathrm{xy} = 0 \quad \text{at} \quad \tilde{\mathrm{y}} = 0. \tag{90}$$

Symmetry requires the partial derivatives of the total velocity, differential velocity, normal components of the stress tensor, and polymer number density with respect to the channel position to be zero at the centerline. Furthermore, the value of the total momentum balance Eq. (32) and the maximum of the total velocity at the centerline require the shear stress and thus the xy-component of the conformation tensor there to be zero. The normal components of the total and differential velocities are required to be zero at the wall to guarantee no-flux of the material through the walls:

$$\tilde{\mathrm{v}}_\mathrm{y} = \widetilde{\Delta \mathrm{v}}_\mathrm{y} = 0 \qquad \text{at} \qquad \tilde{\mathrm{y}} = 1/2. \tag{91}$$

The tangential components of the total and differential velocities are set to zero at the wall if the wall has a no-slip condition:

$$\tilde{\mathrm{v}}_{\mathrm{x}} = \widetilde{\Delta \mathrm{v}}_{\mathrm{x}} = 0 \qquad \text{at} \qquad \tilde{\mathrm{y}} = 1/2. \tag{92}$$

We also considered the case of slip along the walls. We used the standard linear Navier condition (Ferrás et al., 2012), which relates the wall shear stress to the wall velocity as follows, to illustrate how to account for the slip in our two-fluid framework:

$$\tilde{\mathrm{v}}_{\mathrm{x}}^{p} = -\, k_p \tilde{\sigma}_{\mathrm{xy}}^{p}, \tag{93}$$

$$\tilde{\mathrm{v}}_{\mathrm{x}}^{s} = -\, k_s \tilde{\sigma}_{\mathrm{xy}}^{s}, \tag{94}$$

where the constants k_p and k_s control the slip magnitude. These constants must be positive for the coordinate system placed as shown in Fig. 25. The following expressions for the tangential components of the kinematic state variables can be obtained if we insert Eqs. (93) and (94) into Eqs. (21) and (22):

$$\widetilde{\Delta \mathrm{v}}_{\mathrm{x}} = \tilde{\mathrm{v}}_{\mathrm{x}}^{p} - \tilde{\mathrm{v}}_{\mathrm{x}}^{s} = -k_p \tilde{\sigma}_{\mathrm{xy}}^{p} + k_s \tilde{\sigma}_{\mathrm{xy}}^{s} \qquad \text{at} \qquad \tilde{\mathrm{y}} = 1/2, \tag{95}$$

$$\tilde{\mathrm{v}}_{\mathrm{x}} = \frac{\rho_p}{\rho} \tilde{\mathrm{v}}_{\mathrm{x}}^{p} + \frac{\rho_s}{\rho} \tilde{\mathrm{v}}_{\mathrm{x}}^{s} = -k_p \frac{\rho_p}{\rho} \tilde{\sigma}_{\mathrm{xy}}^{p} - k_s \frac{\rho_s}{\rho} \tilde{\sigma}_{\mathrm{xy}}^{s} \qquad \text{at} \qquad \tilde{\mathrm{y}} = 1/2. \tag{96}$$

As evident from Eqs. (95)–(96), we can easily impose wall slip on each phase by imposing the corresponding conditions on the total and differential velocities. Note that the higher-order derivatives appearing in the last term of Eq. (42) require special treatment at the boundaries (Germann et al., 2016). The conformation diffusion should vanish at the solid boundaries within a distance less than the radius of gyration because of the local surface effects and because the diffusivity is essentially proportional to the normal thickness of the polymer molecules. The thickness becomes zero as these become flat to fit next to the surface. A detailed explanation can be found in Mavrantzas and Beris (1992), where the main reason, namely, the surface acting as a barrier prohibiting many internal conformations, is mentioned along with an exact analysis for c_{yy}. These researchers showed that this quantity is proportional to the normal to the wall thickness of the polymer chains and goes to zero at the wall. Their findings are in excellent quantitative agreement with the Monte Carlo results of Fitzgibbon and McCullough (1989) and the molecular dynamics simulations of Bitsanis and Hadziioannou (1990). In this manner, the use of

any boundary conditions on the conformation tensor, which are arbitrary in our opinion, can be avoided. The best alternative would be to conduct a microscopic analysis down to the monomer length scale next to the wall, which would substantially increase the complexity of the model and its numerical solution. We do not make any assumption here on the shape of D_{nonloc} and set this parameter equal to zero at the walls and to one elsewhere for simplicity. This approach works well as long as the gradients of the conformation tensor are not too high.

The flow problem was solved using the numerical procedure implemented for the Couette flow (See Sec. 3). We used a Chebyshev pseudospectral collocation method (Voigt et al., 1994; Peyret, 2002) with 200 collocation points for spatial discretization and a second-order Crank-Nicolson scheme (Richtmyer and Morton, 1967) for temporal discretization. The nonlinear system of discretized algebraic equations was solved at each time step using an inverse-based ILU preconditioned Newton-Krylov solver (Bollhöfer and Saad, 2006; Bollhöfer et al., 2008).

4.4 Results

First, we start with no slip, where the tangential components of the total and differential velocities are required to be zero at the wall, as formulated in Eq. (92). The remaining boundary conditions are provided in Eqs. (89)–(91). To validate the numerical schemes, we solved first the Oldroyd-B model and compared the results with the available analytical solution of this model. Furthermore, we checked the grid independency of the results of our model by using three different meshes.

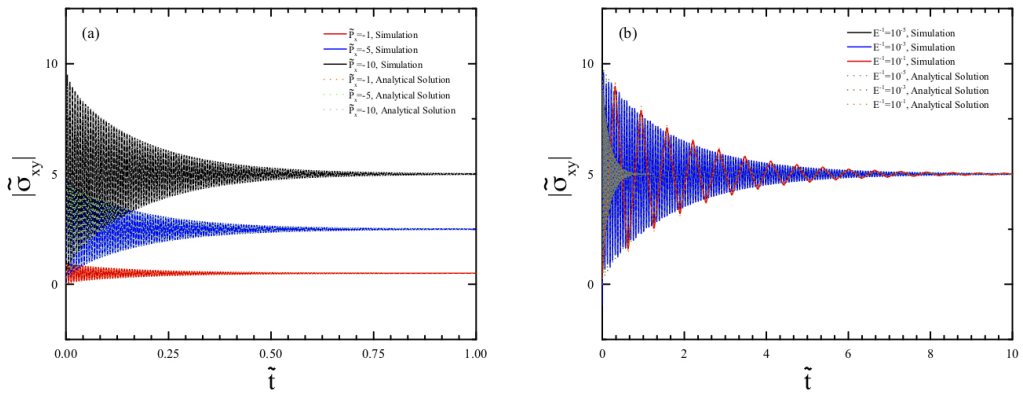

Figure 26: Temporal evolution of the magnitude of the wall shear stress calculated for the Oldroyd-B model with $\beta = 10^{-5}$ and validation with the analytical solution using (a) different values of the pressure gradient with $E^{-1} = 10^{-5}$ and (b) different reciprocal elasticities with $\tilde{P}_x = -10$.

We solved the Oldroyd-B model for the flow problem described in Sec. 4.2 and compared the numerical results with the transient analytical solution of Waters and King (1970) to validate the numerical code. The Oldroyd-B model is a limiting case of our model obtained by setting $\alpha = \epsilon = \tilde{D} = \tilde{D}_{nonloc} = 0$. Fig. 26 shows the temporal evolution of the magnitude of the shear stress at the wall, which is manifested by damped oscillations converging to its steady-state value. The results are in excellent agreement with the analytical solution, thereby confirming the validity and accuracy of the numerical code. Furthermore, we observed that a larger pressure gradient leads to an increase in the average magnitude of the wall shear stress and amplitude of the oscillations (see Fig. 26(a)). Increasing E^{-1} has no effect on the steady state. Inertia only decreases the frequency of the oscillations (Fig. 26(b)).

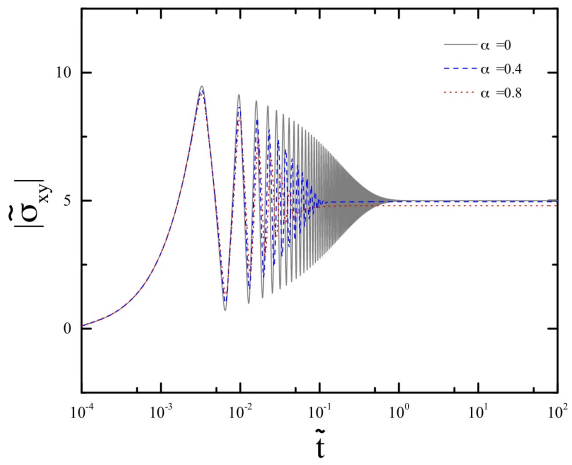

Figure 27: Temporal evolution of the magnitude of the shear stress at the wall calculated for the two-fluid model using different values of α. The other nontrivial values of the model parameters used in the calculation are $E^{-1} = 10^{-5}$, $\tilde{P}_x = -10$, $\epsilon = 0.0025$, $q = 1.46$, $\beta = 10^{-5}$, $\chi = 10^{-1}$, and $\tilde{D} = \tilde{D}_{nonloc} = 10^{-3}$.

We also present how the model parameters affect the solution of the two-fluid model presented in Sec. 2.3. The approximate values of the model parameters were determined in Sec. 2.4 by fitting to the steady-state shear rheology of a 10 wt./wt.% (1.6M) polybutadiene solution (Cheng and Wang, 2012): $\alpha = 0.73$, $\epsilon = 0.0025$, $q = 1.46$, $\chi = 10^{-1}$, and $\beta = 10^{-5}$. The corresponding constitutive curve for the homogeneous shear flow can be found in Sec. 2.4. The boundary layers in the no-slip case are less steep. Therefore, smoothening the profiles was not necessary, and the boundary layer constant was simply set to zero. Fig. 27 shows the temporal evolution of the magnitude of the wall shear stress for different values of the anisotropy factor α. The most intense oscillation is obtained for $\alpha = 0$, as expected from Duarte et al. (2008). Increasing this parameter dampens the oscillations faster. As expected, the

steady-state value of the wall shear stress is slightly smaller for a larger value of α (i.e., for greater shear-thinning). We use $\alpha = 0.73$ for all subsequent calculations.

Fig. 28 shows the influence of the local diffusivity constant on the temporal evolution of the absolute value of the shear stress and the polymer number density at the wall. Fig. 28(a) shows that neither the transient evolution of the wall shear stress nor its steady state significantly varied with the value of $\tilde{D}$. Fig. 28(b) shows that the polymer concentration at the wall needs more time for smaller values of $\tilde{D}$ to reach the steady state, which is independent of this parameter. Increasing the value of the local diffusivity reveals two undershoots in this curve. The first undershoot occurs at $\tilde{t} \simeq 0.05$, which corresponds to the time at which the oscillations of the shear stress and the x-component of the total and differential velocities are totally damped. The second undershoot for $\tilde{D} \geq 0.1$ corresponds to the fact that the velocity profile increases to a temporary maximum at $\tilde{t} \simeq 3$ (Fig. 29(b)).

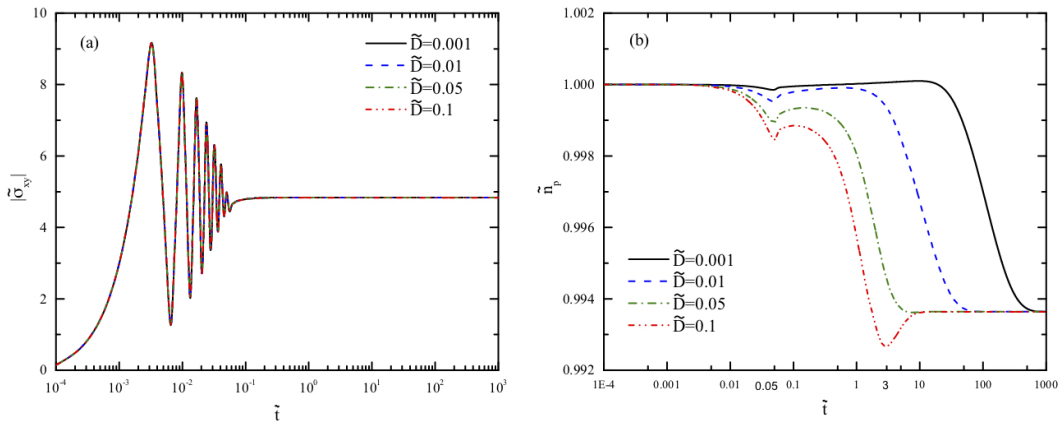

Figure 28: Effect of $\tilde{D}$ on (a) the temporal evolution of the magnitude of the wall shear stress and (b) the temporal evolution of the polymer number density at the wall. The other nontrivial values of the model parameters are $E^{-1} = 10^{-5}$, $\tilde{P}_x = -10$, $\alpha = 0.73$, $\epsilon = 0.0025$, $q = 1.46$, $\beta = 10^{-5}$, $\chi = 10^{-1}$, and $\tilde{D}_{nonloc} = 10^{-3}$.

Fig. 29 presents the effect of diffusion on the temporal evolution of the total velocity. In Fig. 29(a), we observe that the local velocity for $\tilde{D} = 10^{-3}$ monotonically increases at each point in the flow domain to the corresponding value of the steady state. The velocity at the centerline for $\tilde{D} = 10^{-1}$ increases to a temporary maximum, and then decreases to the steady-state profile (Fig. 29(b)). However, we do not expect this phenomenon to be observed experimentally because the value of $\tilde{D}$ is extremely large in this case.

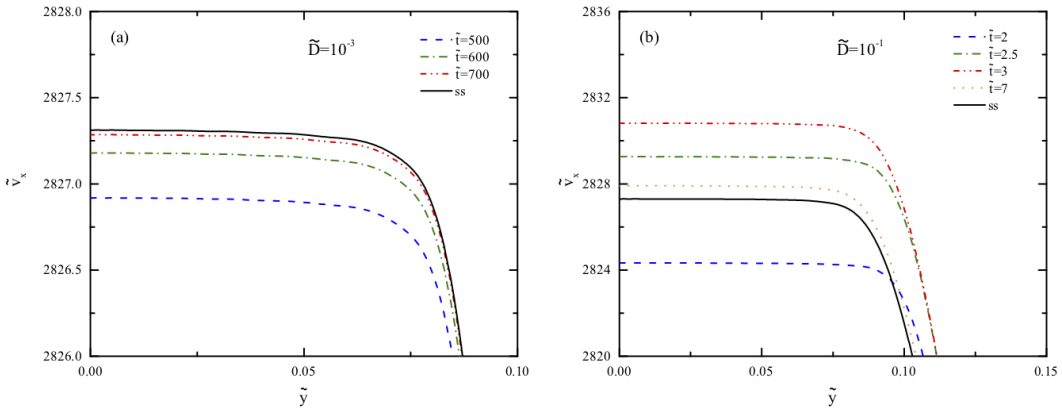

Figure 29: Temporal evolution of the velocity profile with (a) $\tilde{D} = 10^{-3}$ and (b) $\tilde{D} = 10^{-1}$. The other nontrivial values of the model parameters are $E^{-1} = 10^{-5}$, $\tilde{P}_x = -10$, $\alpha = 0.73$, $\epsilon = 0.0025$, $q = 1.46$, $\beta = 10^{-5}$, $\chi = 10^{-1}$, and $\tilde{D}_{nonloc} = 10^{-3}$.

Fig. 30 shows how the nonlocal diffusivity influences the solution. The parameter $\tilde{D}_{nonloc}$ does not substantially affect either the transient or the steady-state solution of the wall shear stress (Fig. 30(a)). The profiles of the polymer number density obtained for different values of $\tilde{D}_{nonloc}$ reach the steady state at approximately the same time (Fig. 30(b)). However, Fig. 30(c) shows that a larger value of $\tilde{D}_{nonloc}$ leads to a more uniform concentration profile in the steady state. The kinks separating the bands in this curve become closer to the centerline as the nonlocal diffusivity decreases because of the lower stress diffusion. Interestingly, the value of $\tilde{D}_{nonloc}$ does not greatly affect the steady-state velocity across the gap, as shown in Fig. 30(d). We plot the $xx-$ and xy-components of the conformation tensor in the vicinity of the upper wall to confirm that the selected shape of the nonlocal diffusivity results in a smooth near-wall dynamics (Fig. 31).

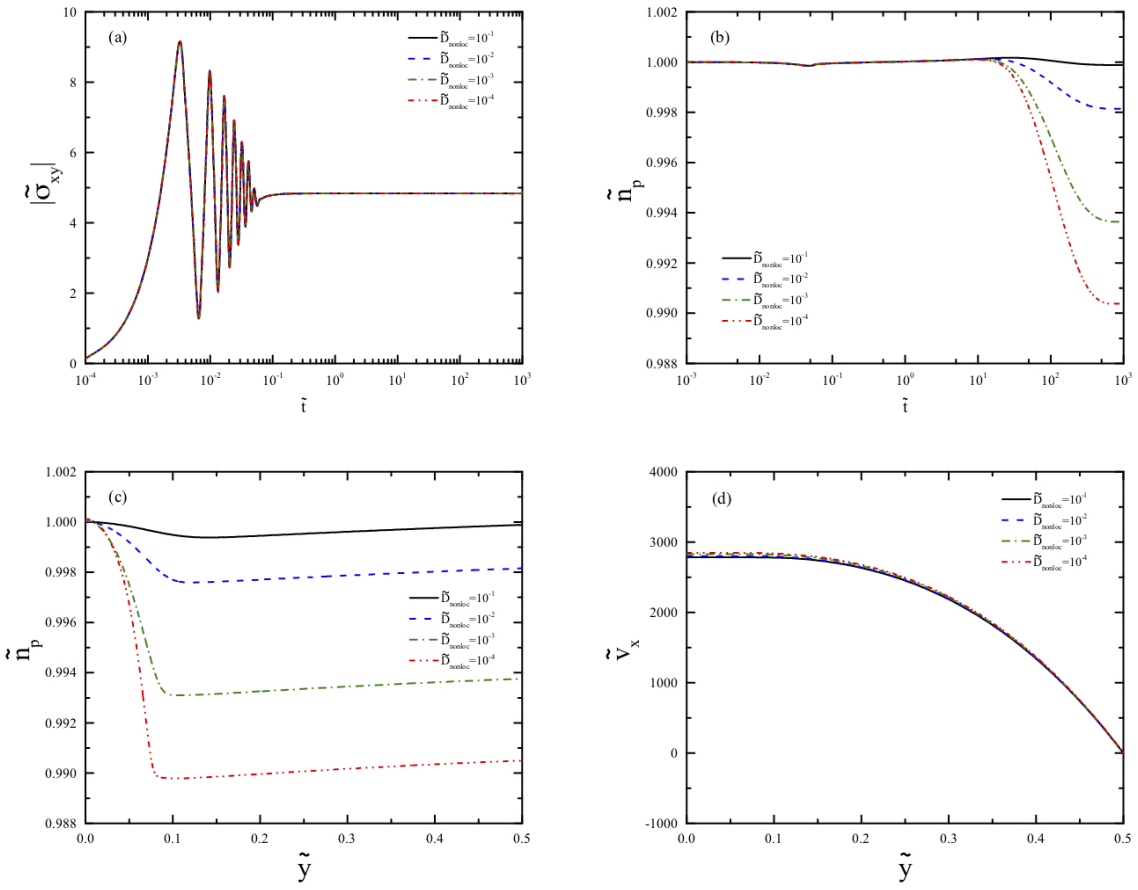

Figure 30: Effect of $\tilde{D}_{nonloc}$ on the (a) temporal evolution of the wall shear stress magnitude, (b) temporal evolution of the polymer number density at the wall, (c) steady-state profile of the polymer number density across the gap, and (d) steady-state profile of the velocity across the gap. The other nontrivial values of the model parameters are the same as those given in the caption of Fig. 29(a).

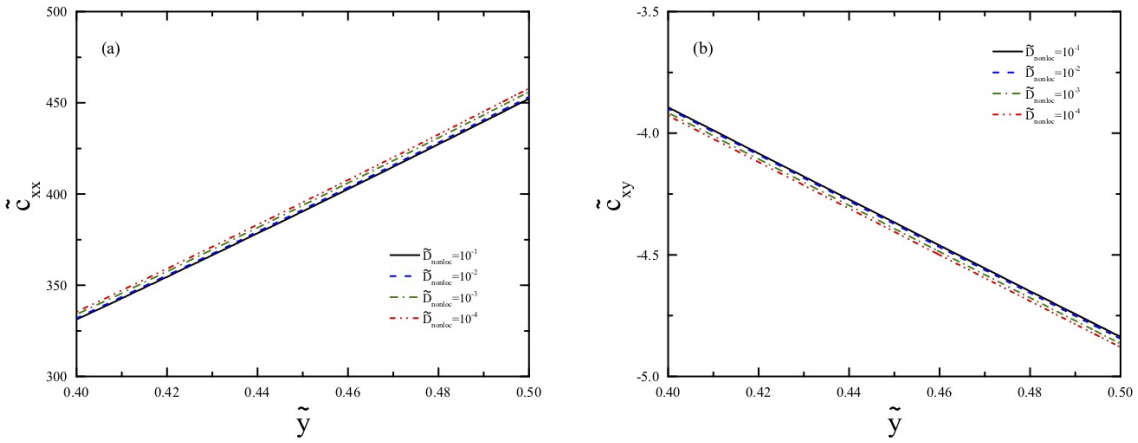

Figure 31: Near-wall dynamics of the (a) xx- and (b) xy-components of the conformation tensor. The nontrivial values of the model parameters are the same as those given in the caption of Fig. 29(a). The $y = 0$ and 0.5 values correspond to the centerline and the channel wall, respectively.

Figs. 32(a)-(d) show the effect of increasing the absolute value of the pressure gradient on the steady-state profiles of the velocity, shear stress, first normal stress difference, and polymer number density across the gap, respectively. The velocity profile decreases from the centerline to the walls with a low shear band near the center and a high one near the walls. Shear-thinning reduces the wall slip and consequently flattens the typical parabolic velocity profiles observed in Newtonian fluids (Oliveira and Pinho, 1999). The stress-induced migration moves the polymer particles toward the center of the channel. The sharp kink separating these bands is considerably smoother than that predicted by the VCM model (Cromer et al., 2011b) for wormlike micelles. No sharp transition is obtained here even if $\tilde{D}_{nonloc} = 0$. The velocity profile for $P_{\rm x} = -1$ is linear. The profile becomes plug-like as the magnitude of the pressure gradient further increases. Moreover, the maximum value of the velocity decreases. As required by the total momentum balance, the magnitude of the shear stress linearly increases from zero at the centerline to its maximum at the wall, where this value is larger for the larger absolute values of the pressure gradient. The first normal stress difference monotonically increases from the center to a maximum value at the walls, which is larger for the larger absolute values of the pressure gradient. This profile is different from that predicted by the VCM model, which exhibits a local maximum at the location of the kink because of the flow-induced breakage of the wormlike micelles (c.f. Fig. 12 of Cromer et al. (2011b)). The concentration bands shown in Fig. 32(d) are predicted by the two-fluid model for the same range of pressure gradients, where the velocity profile assumes a plug-like shape. Increasing the magnitude of the pressure gradient reduces the inhomogeneity of the concentration profile and moves the transition region toward the centerline. The polymer concentration is higher at the center than at the wall, which

is in agreement with the predictions by Ianniruberto et al. (1994) for semidilute entangled polymer solutions below the onset of shear banding. The decrease of the polymer concentration already occurs where the velocity profile is plug-like.

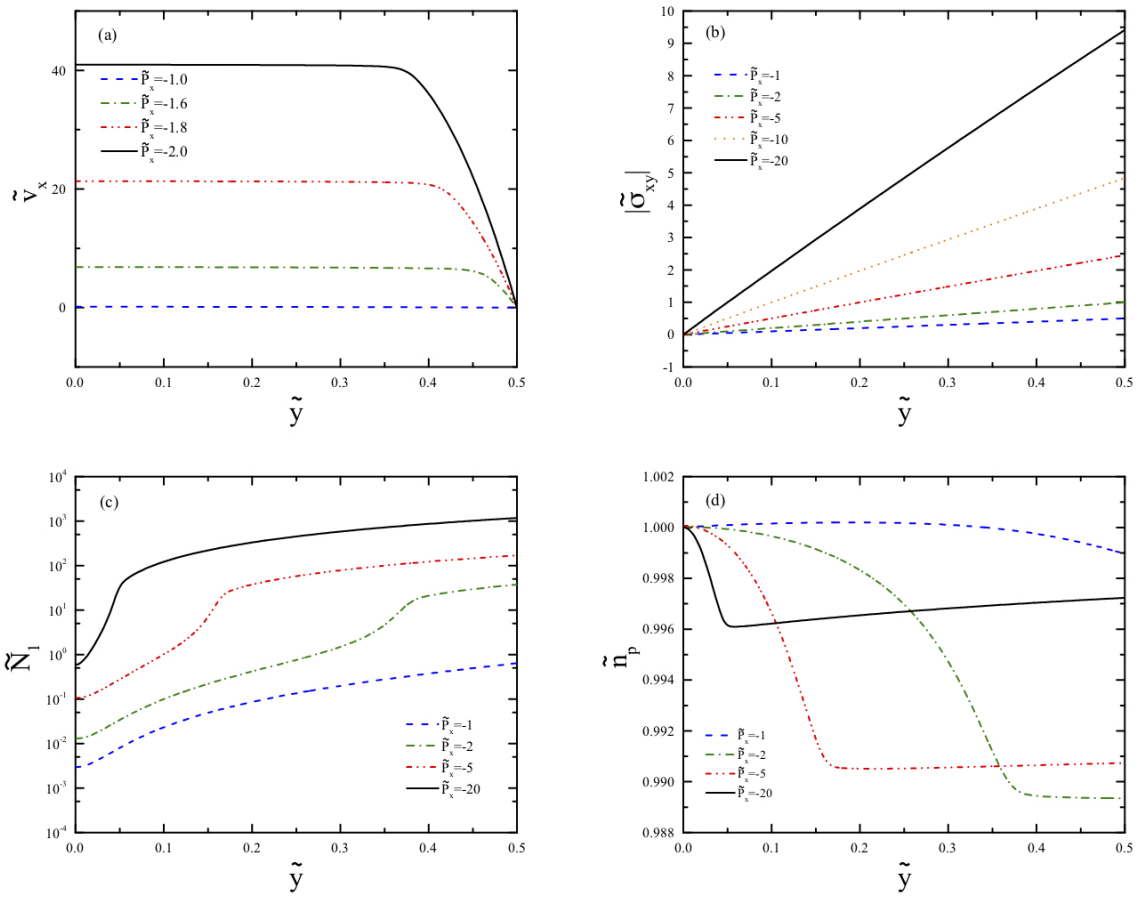

Figure 32: Influence of the pressure gradient on the steady-state profiles of the (a) velocity, (b) shear stress, (c) first normal stress difference, and (d) polymer number density across the channel. The other nontrivial values of the model parameters are the same as those given in the caption of Fig. 29(a).

The volumetric flow rate is calculated using different values of the pressure gradient with $\tilde{D}_{nonloc} = 10^{-3}$, which results in a profile with a spurt at a critical value of the pressure gradient $\tilde{P}_{x,cr} \simeq -1.5$. The agreement of the ramp-up and ramp-down curves shown in Fig. 33(a) confirms the uniqueness of the solution. The nonuniqueness of the results indicated by the hysteresis in constitutive models showing a nonmonotonic flow curve under homogeneous conditions is not observed here. This discrepancy is related to the different underlying mechanisms of the shear band formation and must be experimentally verified in the future. Next, we examine the influence of the nonlocal diffusivity constant on the ramp-up test shown in Fig. 33(b). The critical pressure gradient is not affected by this parameter. Furthermore, the value of the nonlocal diffusivity slightly changes the value of the flow rate in the region of the spurt ($-3 \lesssim \tilde{P}_x \lesssim -1.5$). The smallest nonlocal diffusivity leads to the largest flow rate in the shear banding regime, whereas the opposite behavior is observed in the linear viscoelastic regime.

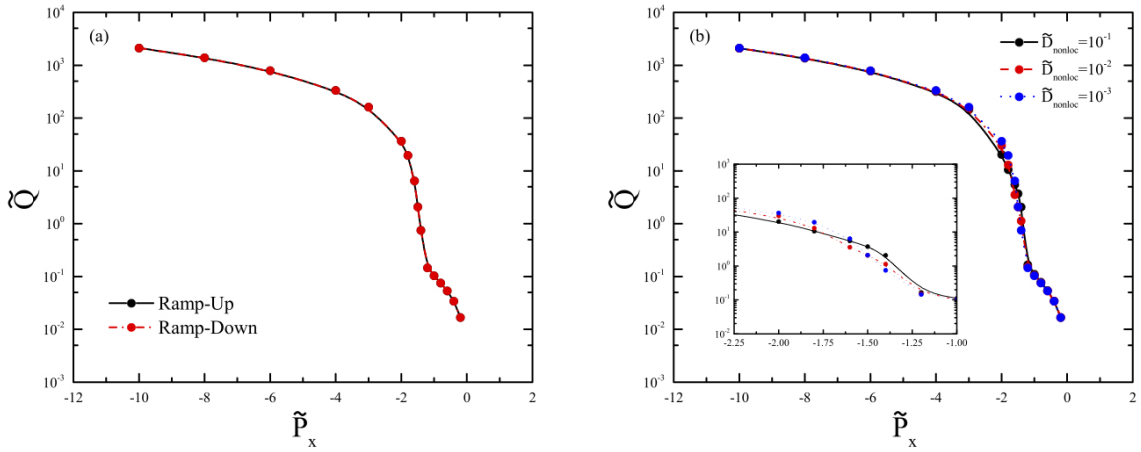

Figure 33: Effect of the pressure gradient on the (a) dimensionless volumetric flow rate with $\tilde{D}_{nonloc} = 10^{-3}$ and (b) the value of the dimensionless volumetric flow rate in ramp-up tests with different values of $\tilde{D}_{nonloc}$. The other nontrivial values of the model parameters are the same as those given in the caption of Fig. 29(a).

Fig. 34 shows the effect of $\tilde{D}_{nonloc}$ on the profile indicating the relation between the pressure gradient and the location of the kink separating the shear bands. We find that increasing the magnitude of $\tilde{P}_{\mathrm{x}}$ moves the kink toward the centerline. The inset of Fig. 34 shows that the value of $\tilde{D}_{nonloc}$ only has a minor influence on this profile for $\tilde{P}_{\mathrm{x}} \geq -40$. As already discussed, in this region and at fixed pressure gradient, the kink is closer to the wall for a larger nonlocal diffusivity. However, a significant impact is observed for large absolute values of the pressure gradient ($\tilde{P}_{\mathrm{x}} \lesssim -90$). This finding is related to the fact that the shear bands fade out at smaller absolute values of $\tilde{P}_{\mathrm{x}}$ for larger $\tilde{D}_{nonloc}$.

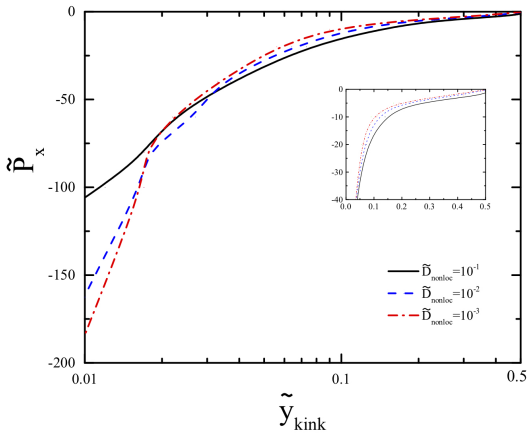

Figure 34: Effect of the pressure gradient on the location of the kink for different values of $\tilde{D}_{nonloc}$. The other nontrivial values of the model parameters are the same as those given in the caption of Fig. 29(a).

Finally, we consider the effect of slip using Eqs. (95)–(96). A nontrivial positive value of the boundary layer constant $\tilde{\xi}$ had to be used to be able to numerically resolve the steep gradients of $\widetilde{\Delta \mathrm{v}_{\mathrm{x}}}$. Fig. 35 shows the x-component of the total velocity (left column) and the differential velocity (right column) across the gap for two different pressure gradients, namely, $\tilde{P}_{\mathrm{x}} = 10$ (top figures) and $\tilde{P}_{\mathrm{x}} = 100$ (bottom figures). The steady-state differential velocity in the y-direction is zero. Therefore, we do not show the profile of this component. Note that all components of the vector $\widetilde{\mathbf{\Delta v}}$ in the no-slip case are zero at the steady state. We note that the parameter k_s that controls the amount of wall slip of the solvent has no significant effect if the results of $k_p = k_s = 50$ are compared with those of $k_p = 50$ and $k_s = 0$. However, increasing the value of k_p, the polymer slip, results in a vertical downward shift of the whole profile of $\widetilde{\mathrm{v}}_{\mathrm{x}}$, thereby leading to a larger wall slip velocity. Interestingly, the parameter $\tilde{P}_{\mathrm{x}}$ has no effect on the shape of the profiles; it only increases the magnitudes of $\widetilde{\mathrm{v}}_{\mathrm{x}}$ and $\widetilde{\Delta \mathrm{v}_{\mathrm{x}}}$.

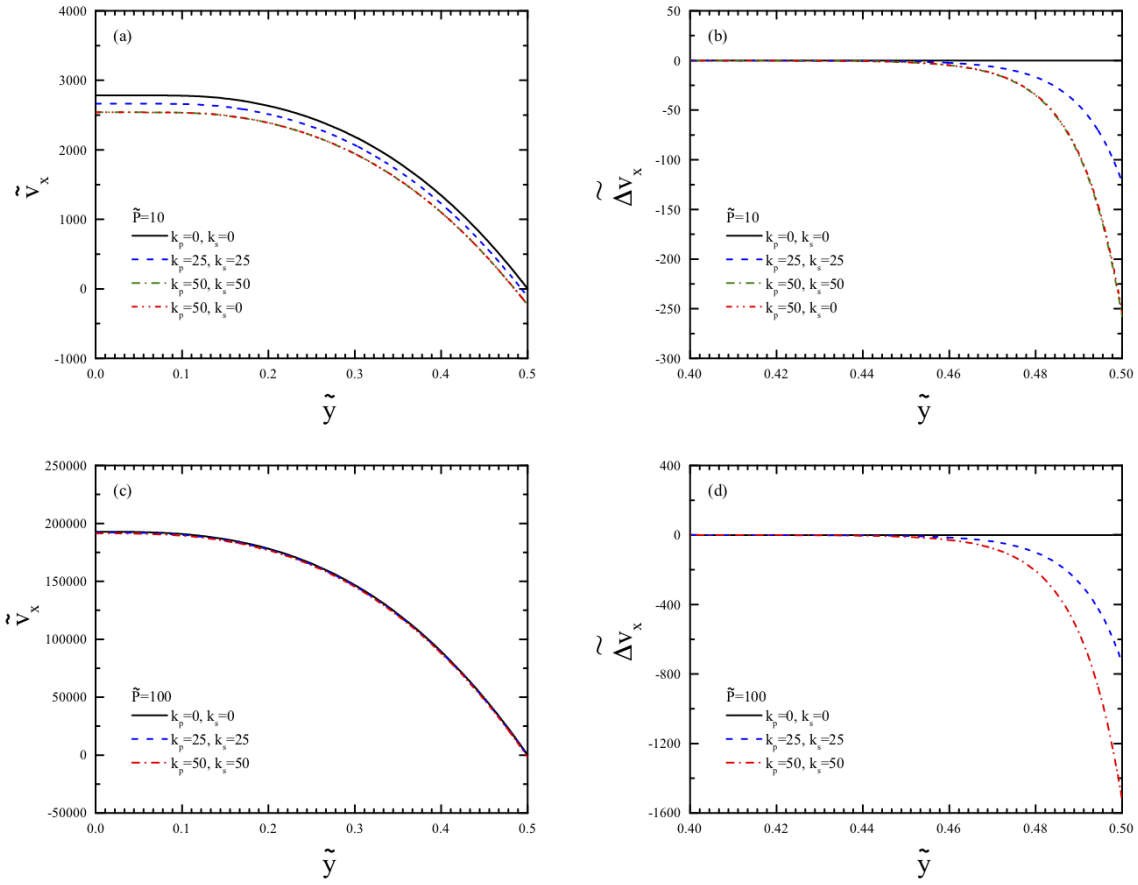

Figure 35: Effect of the value of the slip constants on the steady-state profiles of the total velocity (left column) and the differential velocity (right column) in the x-direction with two pressure gradients $\tilde{P}_x = 10$ (top row) and $\tilde{P}_x = 100$ (bottom row). The values of the parameters are $E^{-1} = 10^{-5}$, $\alpha = 0.73$, $\epsilon = 0.0025$, $q = 1.46$, $\beta = 10^{-5}$, $\chi = 10^{-1}$, $\tilde{\xi} = 10^{-3}$, and $\tilde{D} = \tilde{D}_{nonloc} = 10^{-3}$.

We examine the influence of this quantity below to demonstrate that the selected value of $\tilde{\xi} = 10^{-3}$ had no effect on the results discussed in the preceding paragraph. Figs. 36(a)-(b) show the profiles of the polymer number density and differential velocity, respectively, in the x-direction across the channel for different $\tilde{\xi}$ values. We observe that the profiles of $\widetilde{n}_p$ are not affected. Up to moderate values (i.e., for $\tilde{\xi} \leqslant 10^{-2}$), the boundary layer constant has no influence on the profiles of $\widetilde{\Delta \mathrm{v}_\mathrm{x}}$ in the region inside the channel. However, decreasing the $\tilde{\xi}$ value leads to steeper gradients near the solid walls.

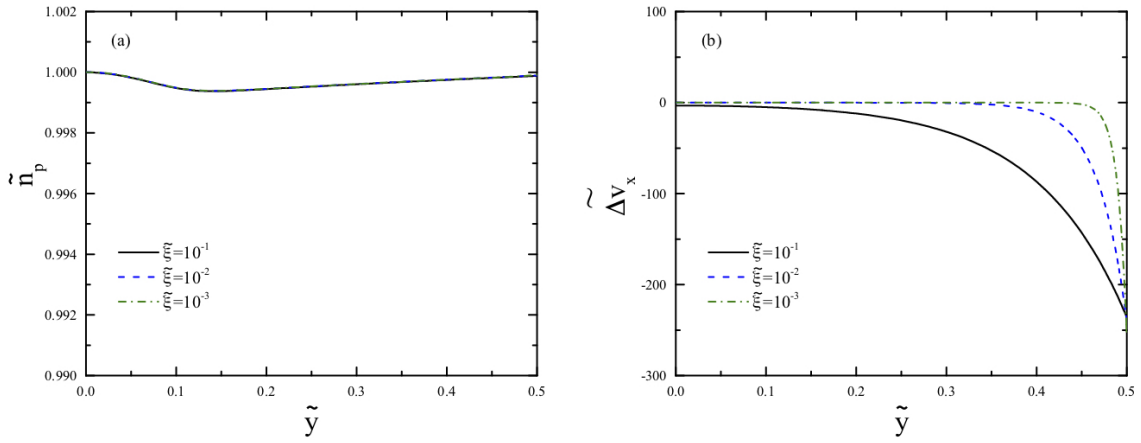

Figure 36: Influence of the specific viscosity on (a) the steady-state profile of the polymer number density and (b) the differential velocity in the x-direction across the gap width with $\tilde{P}_x = 10$ and $k_p = k_s = 50$. The other model parameters are the same as those given in the caption of Fig. 35.

4.5 Conclusion

This section examined the behavior of the new two-fluid model for semidilute entangled polymer solutions in a pressure-driven channel flow. The computational results showed a plug-like profile of the velocity and concentration bands for the same range of pressure gradients. Increasing the value of the pressure gradient shifted the kink separating the shear bands to the center. The steady-state profile of the first normal stress difference monotonically increased from the center of the channel to a maximum value at the walls. The value of the nonlocal diffusivity constant did not significantly influence the total velocity and the wall shear stress. The polymer concentration showed the same temporal behavior for different values of the nonlocal diffusivity constant. However, the steady-state solution was more uniform when we used larger $\tilde{D}_{nonloc}$. The results of the volumetric flow rate calculated using different values of the pressure gradient in the ramp-up and -down tests agreed, thereby confirming the uniqueness of the solution. This profile showed a spurt at a critical pressure gradient, as experimentally observed in the pressure-driven shear flows of polymeric materials. We also studied the effect of wall slip using the linear Navier slip model to illustrate how to account for slip in our two-fluid framework. We noticed that the slip velocity of the solvent had no significant effect on the solution, whereas changing the polymer slip vertically shifted the velocity profile.

5 Benchmark case no. 3: 4:1 contraction flow

5.1 Introduction

Contraction flow is of great importance in many processing operations, such as molding and extrusion of viscoelastic materials. Furthermore, the 4:1 planar contraction is a suitable benchmark problem for the evaluation of new models or codes. Different types of vortices, namely, salient and lip vortices, can appear in this geometry. The lip vortex originates from the re-entrant corner and dominates the flow by vortex enhancement and growth (Boger et al., 1986). Experimental evidence has revealed that the vortex enhancement is absent for Boger fluids while it is apparent for shear-thinning fluids (Nigen and Walters, 2002; Walters and Webster, 2002). Comparisons between strain-hardening low-density polyethylene (LDPE) and strain-softening polystyrene suggest that the size and strength of the vortices are influenced by both extensional and shear properties (Olson and Fuller, 2000; White and Baird, 1986). With increasing flow rate, the vortex size increases if the ratio of the extensional to the shear viscosity increases and vice versa (Aboubacar et al., 2002b).

Numerical simulations of viscoelastic contraction flow use constitutive models according to the material under investigation. Olsson (1994) observed the lip vortex of a shear-thinning fluid for the first time using the Giesekus model. In several works, the Oldroyd-B and PTT models were utilized to describe the behavior of Boger and shear-thinning fluids, respectively. The Oldroyd-B model predicts that the size of the salient vortex decreases, and the lip vortex appears and further grows with increasing flow rate (Walters and Webster, 2002; Alves et al., 2003c). The results of Aboubacar et al. (Aboubacar et al., 2002b,a) revealed that by increasing the elasticity, the Oldroyd-B model and both the linear and exponential versions of the PTT model with a small value of the parameter simultaneously controlling shear-thinning and strain hardening exhibit vortex reduction. The PTT model reverts to the Oldroyd-B model if the value of this parameter reduces to zero. However, the size of the vortex increases for the

PTT model with stronger shear-thinning behavior. Thompson et al. (1999) proposed a new constitutive equation that can predict the increase in the corner vortex size with strain hardening. The idea of their model was that the stress tensor is an isotropic function of the strain rate and the relative rotation rate. White and Baird (1988b) used the PTT model and suggested that extension hardening increases the size and intensity of the vortex, and this proposition was in agreement with their flow visualization and birefringence data (White and Baird, 1988a). The Pom-pom model is an appropriate model to describe contraction flows due to shear-thinning and bounded strain hardening-softening properties. Many works have adopted this model and showed that the size of the vortex increases with the ratio of the extensional to shear stresses (Bishko et al., 1999; Aguayo et al., 2007; Jahromi and Webster, 2011). Ferrás et al. (2014) used the PTT model along with slip boundary conditions. Increasing the slip enlarges the lip vortex until it absorbs the salient vortex. The new single vortex grows in size and intensity with the value of the slip coefficient.

Many features of a planar contraction flow cannot be observed in the 4:1 geometry. Alves et al. (2004) used the linear PTT model to numerically study the effects of the contraction ratio CR and the Deborah number De. They illustrated in a map that the lip vortex appears at $De \approx 1-2$, the vortex enhancement starts at $De/CR \approx 0.5-1$, and the lip vortex becomes completely dominant for $De/CR \geq 1-2$. Their results are in qualitative agreement with the visualizations of Evans and Walters (1986). The material properties of a fluid also affect the vortex enhancement; for instance, no lip vortex was experimentally found at $CR = 4$ for Boger fluids (1.0 wt/wt% polyacrylamide dissolved in maltose syrup and water) or for 0.3 and 0.5 wt/wt% shear-thinning aqueous polyacrylamide solutions observed by Evans and Walters (1989). However, a lip vortex was observed for the lower concentration of 0.2 wt/wt%. This result was numerically confirmed using the finite extensible nonlinear elastic with Peterlin's closure (FENE-P) model (Purnode and Crochet, 1996).

Shear banding is a ubiquitous phenomenon observed in soft materials, such as semidilute entangled polymer solutions. However, limited information is available about its origin and the impact on processing. Germann (2019) comprehensively reviewed recent theoretical and experimental developments in the area of shear banding entangled polymer solutions. Hemminger et al. (2010) experimentally studied a 4:1 rounded-corner contraction flow of 75 kbp DNA solutions with concentrations from 0.1 to 1.0 wt/wt% over a wide range of Deborah numbers (up to 2×10^4 for the most concentrated solution). They observed that the vortex flow dominates for the non-shear-banding solutions with concentrations of 0.1 and 0.5 wt/wt%. However, shear banding was found for the higher concentrations of 0.7 and 1.0 wt/wt% at the entrance of the contraction with a high flow rate at the centerline and a low flow rate at the corner. The authors found that in this regime, reduction in slip length, obtained by, for example, increasing the solvent

viscosity, causes the vortex flow to become dominant again. As the phenomenon of shear banding was studied in the converging zone before the contraction, the flow velocities were much higher than those examined in the present article. Hitherto, no two-fluid model for shear banding polymer solutions has been solved for 4:1 planar contraction flow. The goal of this section is to study the new model in this geometry and to investigate the influence of the shear bands on the vortices.

5.2 Numerical method

We solved the model Eqs. (31)–(33), and (42)–(45) for a steady, laminar, incompressible, two-dimensional flow through a 4:1 planar contraction. In addition, we replaced Eq. (49) with Eq. (97)

$$\widetilde{\mathbf{\Delta v}} = \frac{1}{\widetilde{D}}\Big[\frac{\chi\widetilde{n}_s}{\widetilde{n}_p+\chi\widetilde{n}_s}\Big\{-\widetilde{\mathbf{\nabla}}\left(\widetilde{n}_p\right)+\widetilde{\mathbf{\nabla}}\cdot\widetilde{\boldsymbol{\sigma}}\Big\}+\frac{\widetilde{n}_p}{\widetilde{n}_p+\chi\widetilde{n}_s}\{\widetilde{\mathbf{\nabla}}\left(\widetilde{n}_s\right)+\beta\widetilde{\mathbf{\nabla}}^2\widetilde{\mathbf{v}}^s\}\Big], \tag{97}$$

as the variation in the polymer concentration is very small here, Eq. (37), or Eq. (49) in the dimensionless form, is difficult to solve with a lower-order discretization method. Therefore, we neglected the left-hand side and used the value of the previous iteration for the calculation of the Laplacian term.

A schematic sketch of the flow geometry is given in Fig. 37. The half-width of the downstream channel is denoted by the characteristic height H. As required by the problem, the half-width of the upstream channel is $4H$. Inlet and outlet effects can be neglected since we assume $100H$ for both the lengths of the upstream and downstream channels. The Deborah number is defined as $De = \lambda_1 U_{out}/H$, where U_{out} is the mean velocity at the outlet. The Reynolds number is defined as $Re = \rho U_{out} H/\eta_0 = E^{-1}De$, with E and η_0 being the elasticity number and the zero shear viscosity, respectively, defined below. The Cartesian coordinate system was used as the reference frame. Any dependence on the z-direction was ignored for simplicity.

In the following, we work with nondimensional quantities. The location is scaled by the characteristic height, $\tilde{\mathbf{y}} = \mathbf{y}/H$; the time is scaled by the characteristic relaxation time, $\tilde{t} = t/\lambda_1$; the extra stress is scaled as $\tilde{\boldsymbol{\sigma}} = \boldsymbol{\sigma}/G_0$; and the conformation tensor associated with the polymer is scaled as $\tilde{\mathbf{C}} = (K/n_p k_B T)\mathbf{C}$. The number densities of the polymer and the solvent are normalized using the values at equilibrium as $\tilde{n}_p = n_p/n_p^0$ and $\tilde{n}_s = n_s/n_p^0$, respectively. The dimensionless parameters with respect to these scalings are the elasticity number, $E = G_0\lambda_1^2/(\rho H^2)$; the ratio of the molecular weight of the solvent to that of the polymer, $\chi = M_s/M_p$; the viscosity ratio, $\beta = \eta_s/\eta_0$, with

$\eta_0 = G_0\lambda_1$ being the zero shear viscosity; and the ratio of the characteristic relaxation times, $\epsilon = \lambda_1/\lambda_2$. The total polymer concentration corresponds to the initial uniform polymer concentration and is given in weight percent by $\mu = \tilde{n}_p^0/(\tilde{n}_p^0 + \chi\tilde{n}_s^0)$. The dimensionless diffusion coefficients are $\tilde{D} = D\lambda_1/H^2$ and $\tilde{D}_{nonloc} = D_{nonloc}\lambda_1/H^2$.

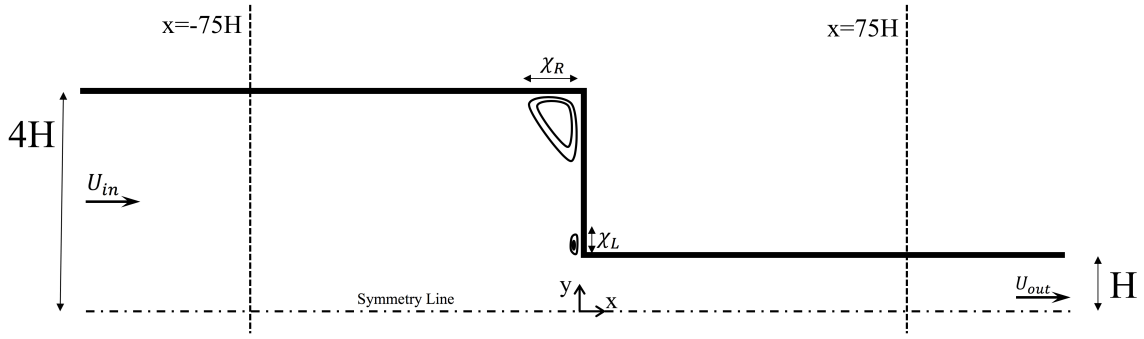

Figure 37: Planar 4:1 contraction geometry.

The OpenFOAM v4.0 finite volume package, together with the viscoelastic solver rheoTool v.2.0 (Pimenta and Alves, 2018), was used to solve the flow problem. To add our model to the solver, we implemented the two-fluid description by using the differential velocity as an intermediate variable, similar to the approach of Guo et al. (2014). In our simulations, the convection term was discretized using the high-resolution convergent and universally bounded interpolation scheme for the treatment of advection (CUBISTA) following a component-wise and deferred correction approach. The diffusion term and the gradients of the velocity and pressure were discretized using the Gauss linear scheme. The Crank-Nicolson method was employed for time discretization. The discretized flow problem was iteratively solved using the semi-implicit method for the pressure linked equations-consistent (SIMPLEC) algorithm with 10 inner iterations per time step. The conjugate gradient method with a diagonal incomplete-Cholesky (DIC) preconditioner was used for solving the continuity and momentum equations and the biconjugate gradient solver with an ILU decomposition for the remaining linear equations. The absolute tolerance for the variables was 1.0×10^{-7} for the steady-state test simulations.

At the inlet boundary, a uniform profile of the polymer number density and a uniform velocity field U_{in} were imposed, resulting in a zero tensorial value for the stress and unity for the polymer conformation. At the outlet boundary, we assumed a vanishing pressure field and fully developed flow with Neumann conditions for the total velocity, the polymer number density and conformation, and the extra stress. At the solid walls, we utilized no-slip and

no-flux conditions for the total velocity. For the polymer number density, we used the Neumann condition. The conformation and stress tensors were linearly extrapolated along the walls using the linearExtrapolation boundary available in rheoTool. The differential velocity must be zero for the conditions specified above. Since no asymmetry was observed relative to the channel centerline in our preliminary calculations, we solved the flow only for the upper half of the channel to avoid unnecessary computations, and we correspondingly used symmetry boundary conditions for the centerline.

The flow was solved using the four meshes reported in Table 1. The coarsest mesh M1 is obtained by considering the upper half of the mesh M1 utilized by Pimenta and Alves (2017). Their mesh is generated so that the resolution is higher near the walls and the corners. We doubled and tripled the number of faces of our mesh M1 in both spatial directions to obtain meshes M2 and M3, respectively. The number of faces of M3 is doubled in both directions to generate the mesh M4.

Table 1: Mesh characteristics.

Mesh	$\Delta x_{min}/\mathbf{H} = \Delta \mathbf{y}_{min}/\mathbf{H}$	**Number of Cells**
M1	0.0042	6051
M2	0.0021	24,204
M3	0.0014	54,459
M4	0.0007	217,836

5.3 Results

To validate the numerical scheme, we first checked the consistency of the implemented terms of the new model by comparison with the numerical solution obtained for steady homogeneous Couette flow presented in Sec. 2.4. Afterward, we solved the benchmark problem for the Oldroyd-B model and compared our results with those of Pimenta and Alves (2017). The dimensionless size of the corner vortex, $\tilde{\chi}_R$, is shown in Fig. 38(a) for Deborah numbers up to 4, where Re was kept constant at 0.01. As the Deborah number increases, the corner vortex becomes smaller. We find that the agreement is excellent. The streamlines displayed for $De = 4$ in Fig. 38(b) also closely match with those published for the same condition in Pimenta and Alves (2017). After the grid independence test, subsequent simulations were performed using mesh M3.

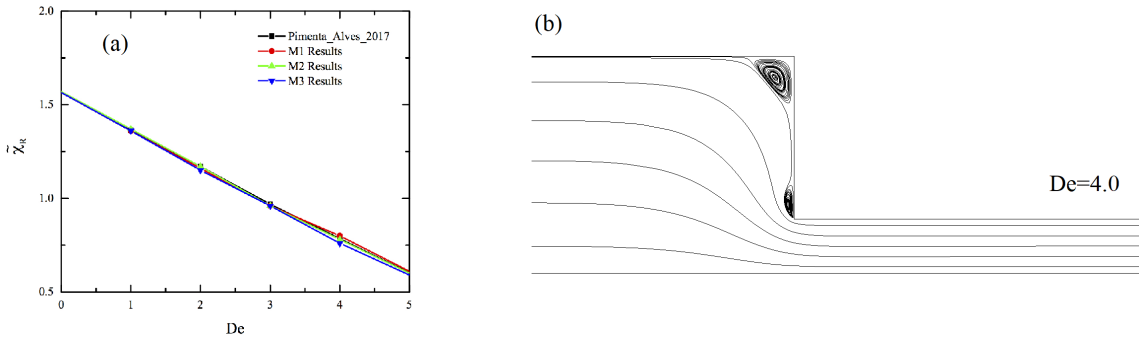

Figure 38: Solution of Oldroyd-B model for 4:1 contraction: (a) size of dimensionless corner vortex for different Deborah numbers and (b) streamlines at $De = 4$ and $Re = 0.01$. The results are compared with those of Pimenta and Alves (2017) for validation.

The planar contraction flow is a combination of a simple shear flow and a uniaxial extension. The predictions of our model for these flows under homogeneous flow conditions are shown in Fig. 39. The values are the same as those used in Sec. 2.4. The model parameters were determined by fitting the flow curve of the shear stress against the shear rate with shear experiments of a 10 wt/wt% (1.6 M) shear-banding polybutadiene solution (Cheng and Wang, 2012). The parameters are the mobility factor $\alpha = 0.73$, the ratio of the characteristic relaxation times $\epsilon = 0.0025$, the power-law factor $q = 1.46$, the viscosity ratio $\beta = 10^{-4}$, and the ratio of the molecular weight of the solvent to that of the polymer $\chi = 10^{-1}$. A moderate nondimensional nonlocal diffusion coefficient $\tilde{D}_{nonloc} = 10^{-3}$ was selected to remove the sharp kink in the banded profiles, and a moderate nondimensional local diffusion constant $\tilde{D} = 10^{-3}$

was used to avoid long running times since the value of this coefficient does not affect the steady-state solution. In homogeneous simple shear (Fig. 39(a)), both the shear stress and the first normal stress difference increase monotonically with the shear rate. In homogeneous uniaxial extension (Fig. 39(b)), the extensional viscosity shows a plateau followed by mild extension thickening and thinning.

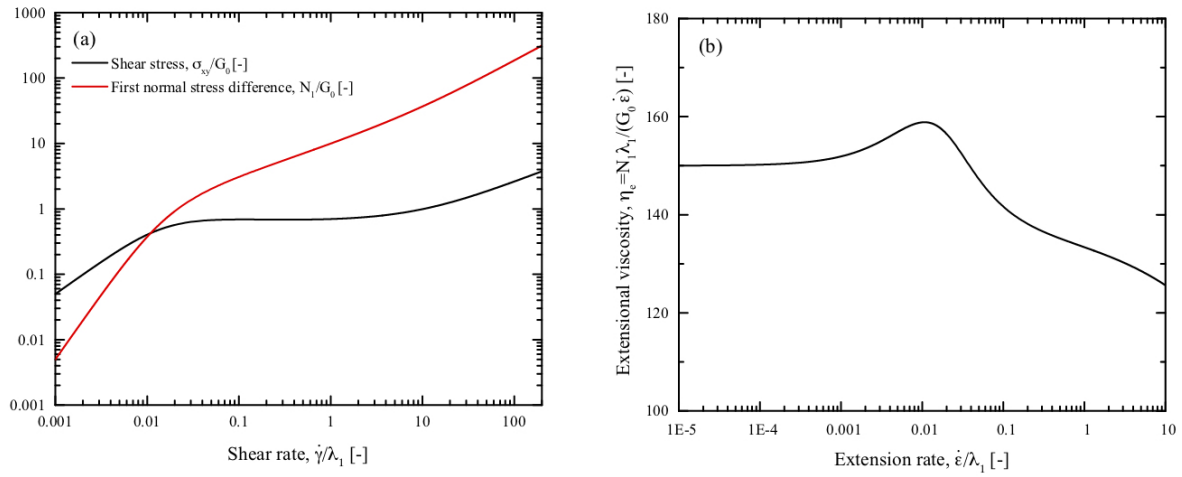

Figure 39: (a) Dimensionless shear stress and first normal stress difference vs dimensionless shear rate in homogeneous simple shear flow. (b) Dimensionless viscosity vs dimensionless extension rate in homogeneous uniaxial extension.

In Fig. 40, we show the size of the corner vortex, $\tilde{\chi}_R$, and the maximum value of the vortex intensity, $\tilde{\psi}_R$, respectively, for the Deborah numbers 0.1, 0.5, 1, 1.5, and 2. The corner vortex size increases with De due to shear-thinning as expected (Aboubacar et al., 2002b; Alves et al., 2003a); however, it decreases as the shear banding starts to occur at $De = 1$, which is in agreement with the experimental data (Hemminger et al., 2010). The vortex intensity follows the trend of the vortex size.

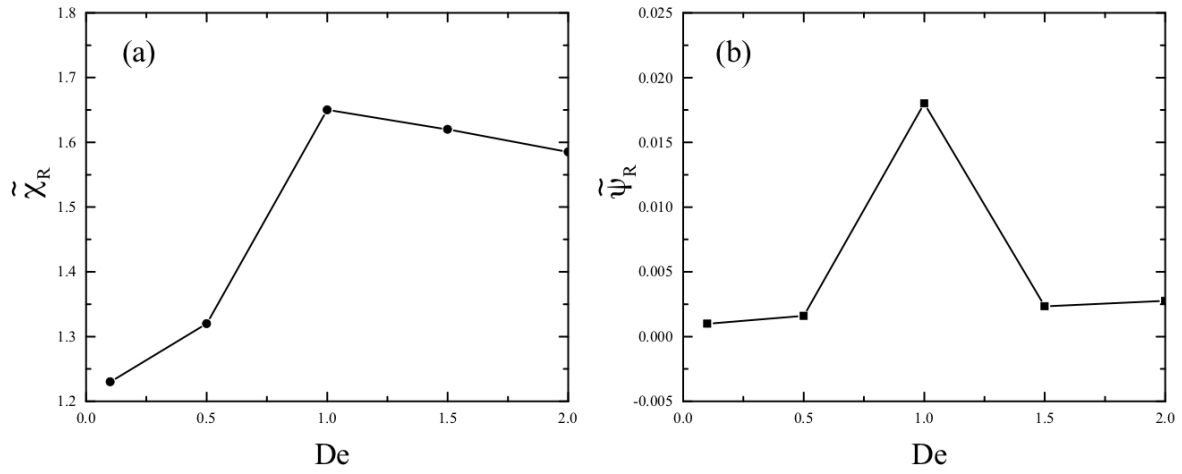

Figure 40: (a) Corner vortex size normalized by characteristic height H and (b) corner vortex intensity normalized by $U_{out}H$ versus Deborah number.

In Fig. 41, we see the profiles of the axial velocity $\tilde{v}_x$, the polymer number density $\tilde{n}_p$, the shear stress $\tilde{\sigma}_{xy}$, and the first normal stress difference $\tilde{N}_1 = \tilde{\sigma}_{xx} - \tilde{\sigma}_{yy}$ at $\tilde{x} = -75$. The selected cross-section is so that the effects of the inlet and the contraction region can be neglected. In these plots, $\tilde{y} = 0$ and 4 represent the centerline and the wall, respectively. In Fig. 41(a), the profiles of the axial velocity are shown. Note that the value of De is evaluated at the outlet; therefore, the Deborah number calculated at the upstream using the inlet velocity and the inlet width is only 1/16 of the written value. This explains why there is no evidence of shear banding for these small values of De before the contraction. The profiles of the polymer number density are shown in Fig. 41(b). The overshoot generated at larger De is due to the Fickian diffusion, which moves toward the wall as De is increased. In Fig. 41(c), the profiles of the shear stress are depicted. The value of $\tilde{\sigma}_{xy}$ is zero at the centerline and increases linearly to the maximum value at the wall, as typically observed for pressure-driven channel flow (see Sec. 4). The absolute wall shear stress is larger for larger De numbers. In Fig. 41(d), we show the first normal stress difference, which is larger for a flow with increasing values of De. The value of $\tilde{N}_1$ is zero at the centerline and quadratically increases for larger De as the wall is approached.

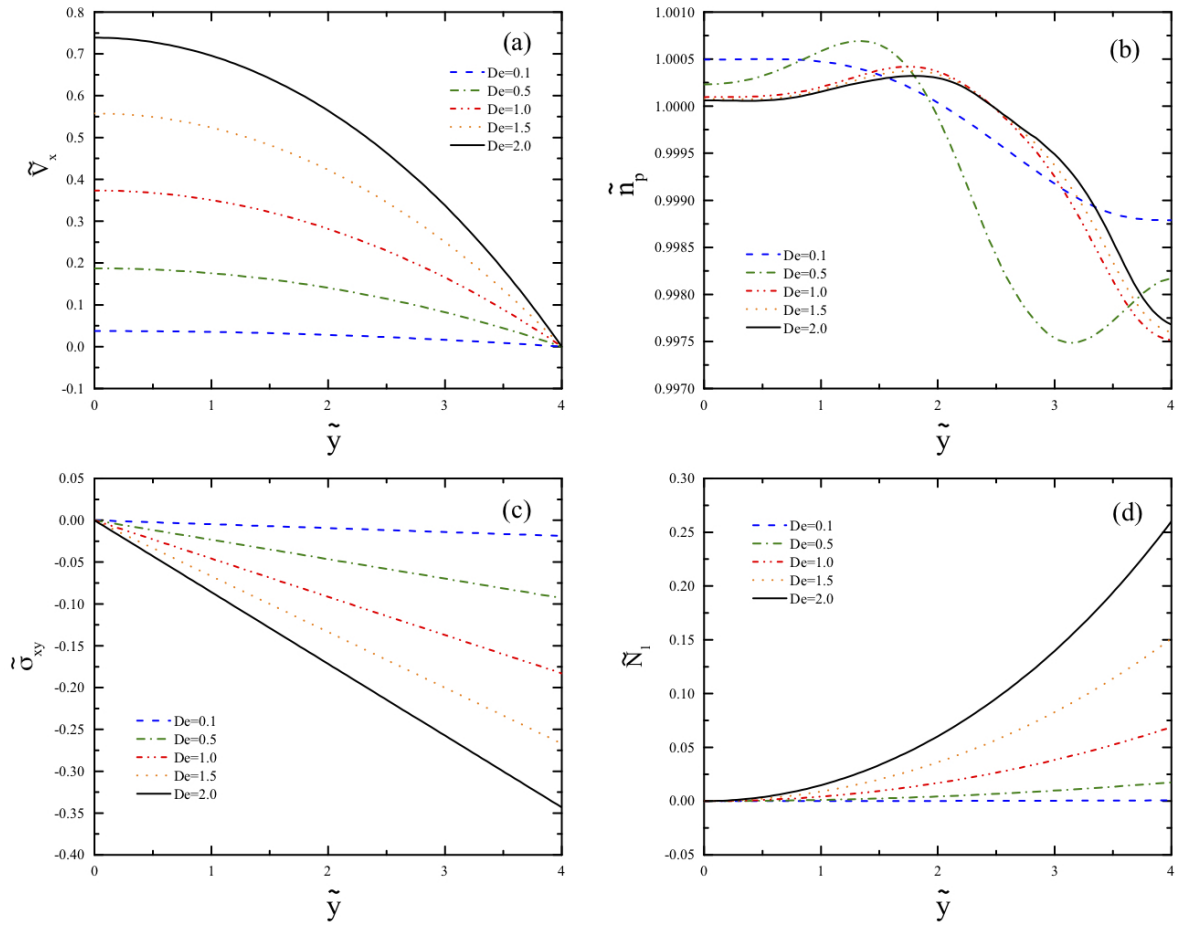

Figure 41: Profiles of (a) axial velocity, (b) polymer number density, (c) shear stress, and (d) first normal stress difference evaluated at $\tilde{x} = -75$ for different Deborah numbers.

Fig. 42 shows the results of the channel far away from the contraction at $\tilde{x} = 75$. The velocity profiles shown in Fig. 42(a) deviate from the typical parabolic profile of channel flow and form plug-like flow for $De \geqslant 1$. This phenomenon is related to shear banding. The kink separating the bands move toward the center of the channel as De increases. The profiles of the polymer number density are illustrated in Fig. 42(b). For $De \geqslant 1$, we can see clear bands where the band near the centerline forms a plateau, and the other band shows a strong decrease near the wall. The effect of shear banding is much smaller than the effect of recirculation for the De values considered in this work (Fig. 42(b)). However, at very large De values, the opposite trend may be found. Fig. 42(c) shows that the profiles of the shear stress increase from zero at the centerline to the extremum at the wall. The overlap of these profiles in the shear banding regime is expected from the plug-like velocity profiles, where the similar shear rates of the bands result in similar stress profiles in the plateau regime of the flow curve. The small difference in the bands

arises from the relatively narrow range of De examined. The profile of the shear stress in the shear banding regime shows nonlinearity near the wall if the resolution of the mesh is not high enough; therefore, we used the mesh M4 to obtain Fig. 42(c).

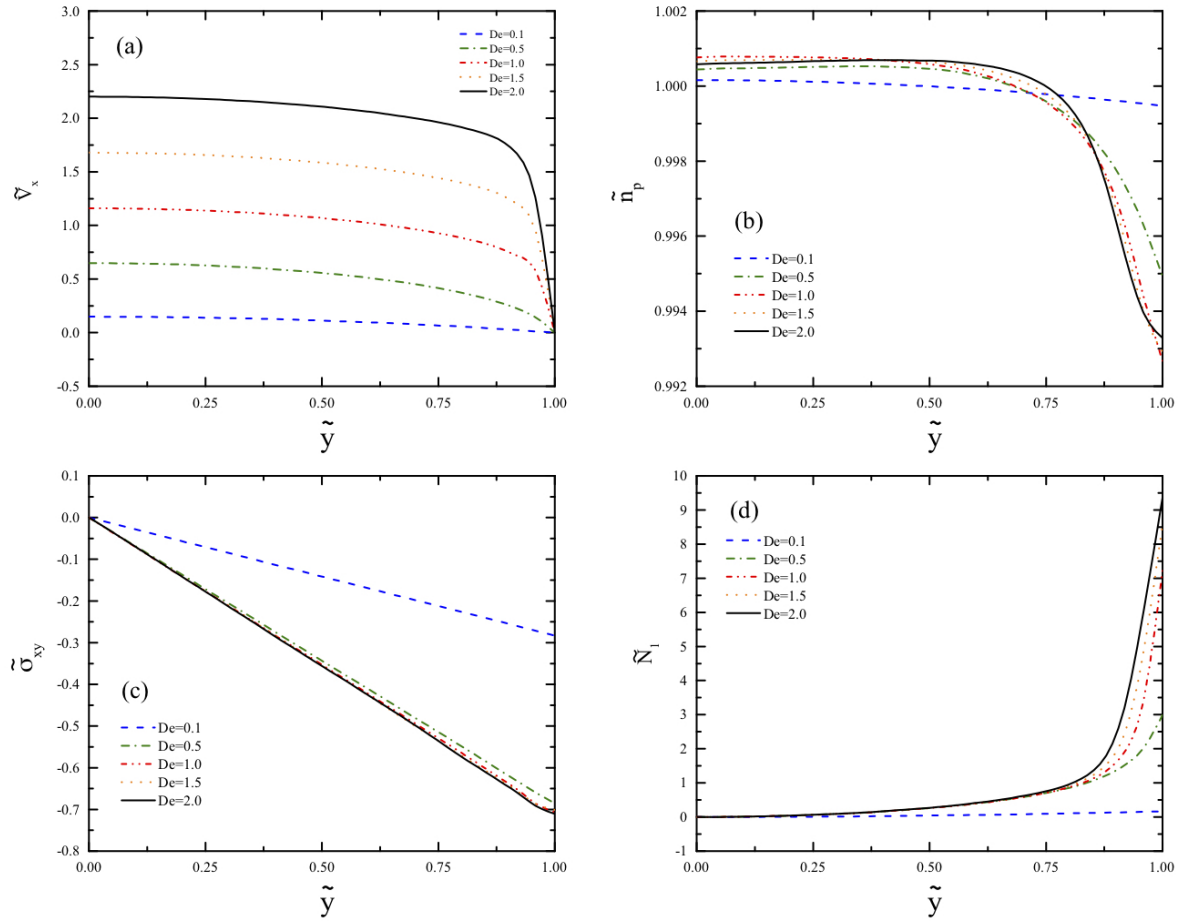

Figure 42: Profiles of (a) axial velocity, (b) polymer number density, (c) shear stress, and (d) first normal stress difference evaluated at $\tilde{x} = 75$ for different Deborah numbers.

Fig. 43 shows the streamlines and the contours of the flow for $De = 0.5$. We can see a vortex at the corner in Fig. 43(a). The contour of the polymer number density is shown in Fig. 43(b). We note a huge increase in $\tilde{n}_p$ as a result of flow recirculation. At the re-entrant corner, there is a concentrated zone of large absolute shear stress values (Fig. 43(c)). The first normal stress difference (Fig. 43(d)) becomes negative as a result of a large $\tilde{\sigma}_{yy}$ value. It must be noted that $\tilde{\sigma}_{zz}$ is nonzero in the channel, although the values are much smaller than the other normal components of the shear stress. Our viscoelastic flow predictions depicted in Figs. 43-45 qualitatively agree with the velocity and stress calculations of the Giesekus, PTT, and FENE-P models (Azaiez et al., 1996; Favero et al., 2010).

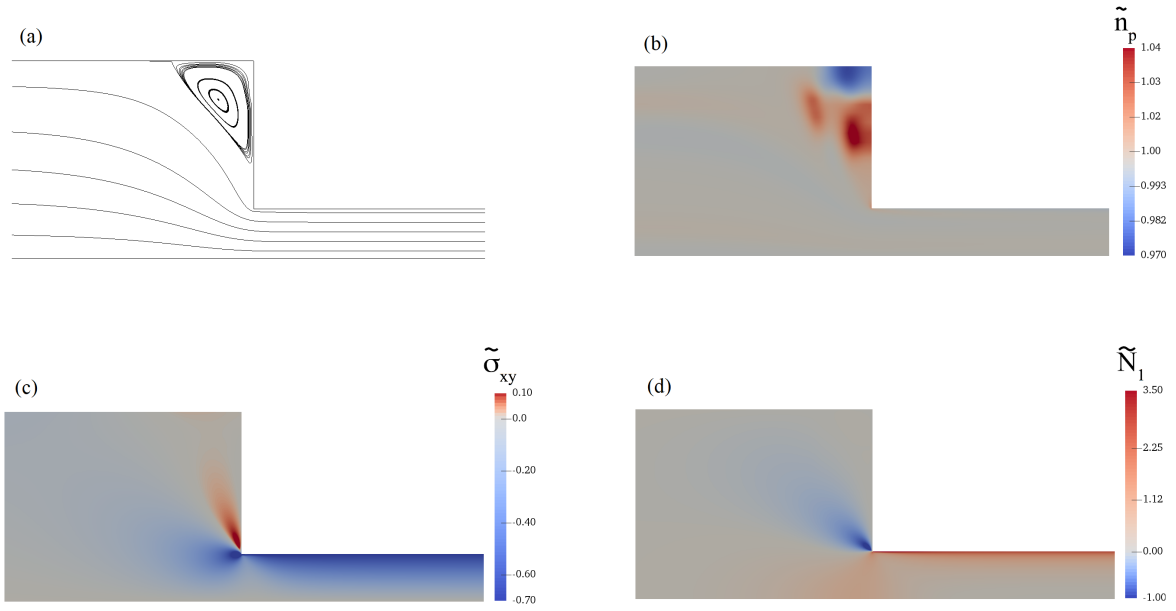

Figure 43: Contours of (a) stream function, (b) polymer number density, (c) shear stress, and (d) first normal stress difference for $De = 0.5$.

Fig. 44 shows the results for the flow $De = 0.5$ at different vertical cross-sections before and after the contraction. We see in Fig. 44(a) how the axial velocity profile adapts itself to the narrow channel. The velocity strongly increases due to the requirement of the mass conservation. However, the shear rate is still not large enough for $De = 0.5$ to form a banded plug-like curve. Fig. 44(b) shows the profiles of the polymer number density in the vertical sections. The strong overshoot of the profile at $\tilde{x} = -0.5$ corresponds to the recirculation region depicted in Fig. 43(b). In Fig. 44(c), we can see that the value of the shear stress changes its sign in the recirculation region, while this profile is linear further away ($\tilde{x} = -10$ and 5). The profiles of the first normal stress difference are shown in Fig. 44(d). The negative sign of $\tilde{N}_1$ in the recirculation zone suggests that the $\tilde{\sigma}_{yy}$-component dominates in this region. The

large values of the first normal stress difference after the contraction region is due to the larger local De after the contraction.

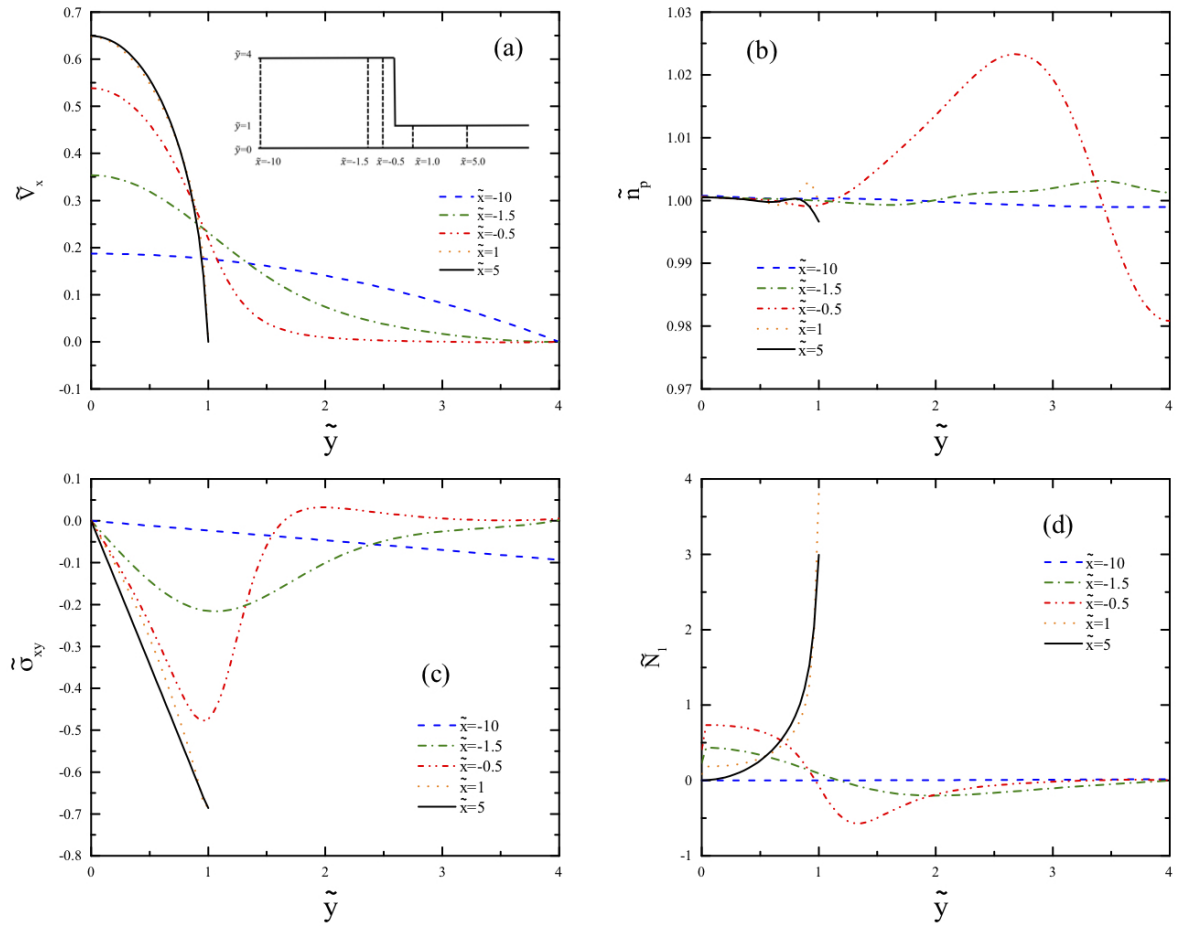

Figure 44: Profiles of (a) axial velocity, (b) polymer number density, (c) shear stress, and (d) first normal stress difference for $De = 0.5$ at vertical cross-sections $\tilde{x} = -10$, -1.5, -0.5, 1.0, and 5.0.

Fig. 45 shows the profiles in cross-sections parallel to the centerline. Since the important changes happen in the contraction region, we only depict the part of the channel in the range $-10 \leqslant \tilde{x} \leqslant 10$. There is strong shearing near the walls and significant uniaxial extension along the centerline. As the flow approaches the contraction, the increasing extension rate increases the velocity for $\tilde{y} = 0$ and 0.5 (Fig. 45(a)). It is evident from Fig. 45(b) that $\tilde{n}_p$ increases in the recirculation region at $\tilde{y} = 2.5$ and overshoots at $\tilde{y} = 3.5$, which matches with the shape of the vortex. We can see in Fig. 45(c) that $\tilde{\sigma}_{xy}$ undershoots and overshoots before and after the contraction, respectively. The maximum of $\tilde{N}_1$ occurs close to the contraction (Fig. 45(d)).

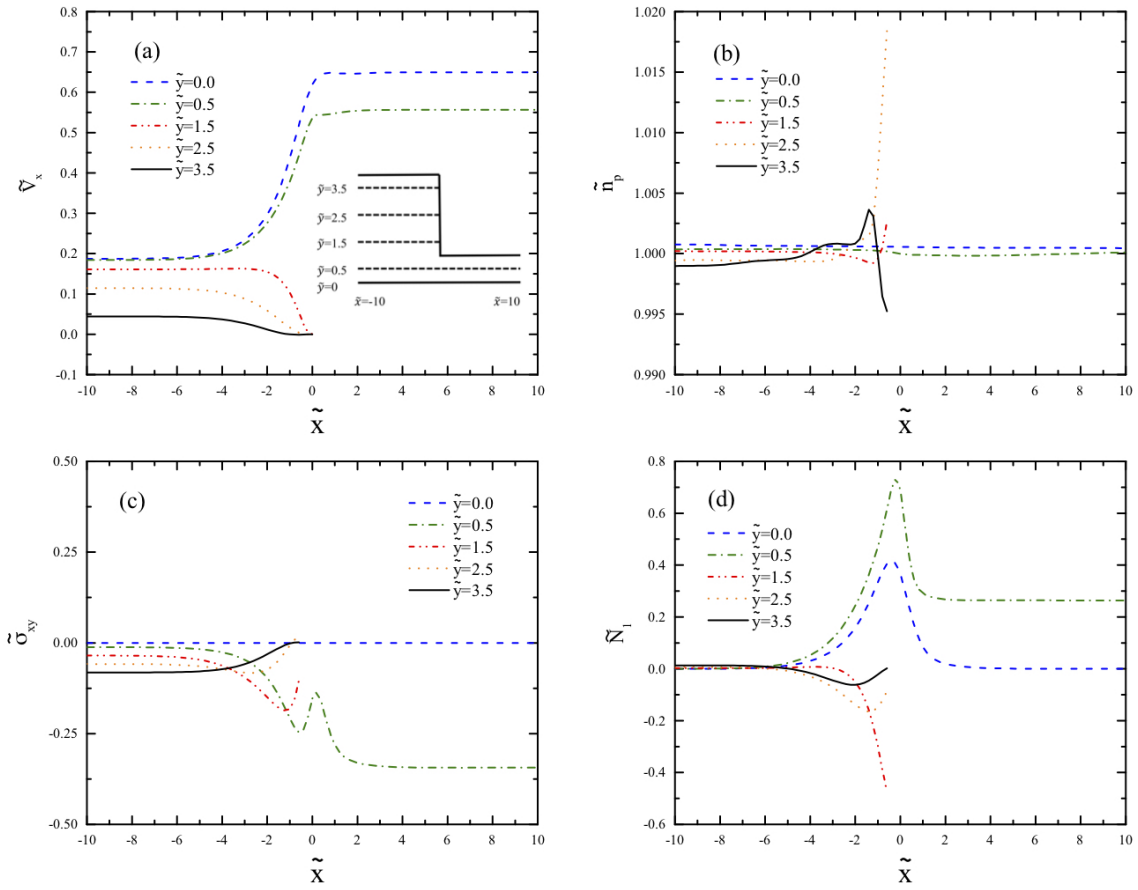

Figure 45: Profiles of (a) axial velocity, (b) polymer number density, (c) shear stress, and (d) first normal stress difference for $De = 0.5$ at horizontal cross-sections $\tilde{y} = 0$, 0.5, 1.5, 2.5, and 3.5.

The streamlines and contours are shown for $De = 2$ in Fig. 46 and are compared with the information of Fig. 43. The vortex size is larger, and the accumulation of the polymer particles in the recirculation zone is closer to the wall. The contours of the shear stress and first normal stress difference are qualitatively similar, but the magnitudes are larger.

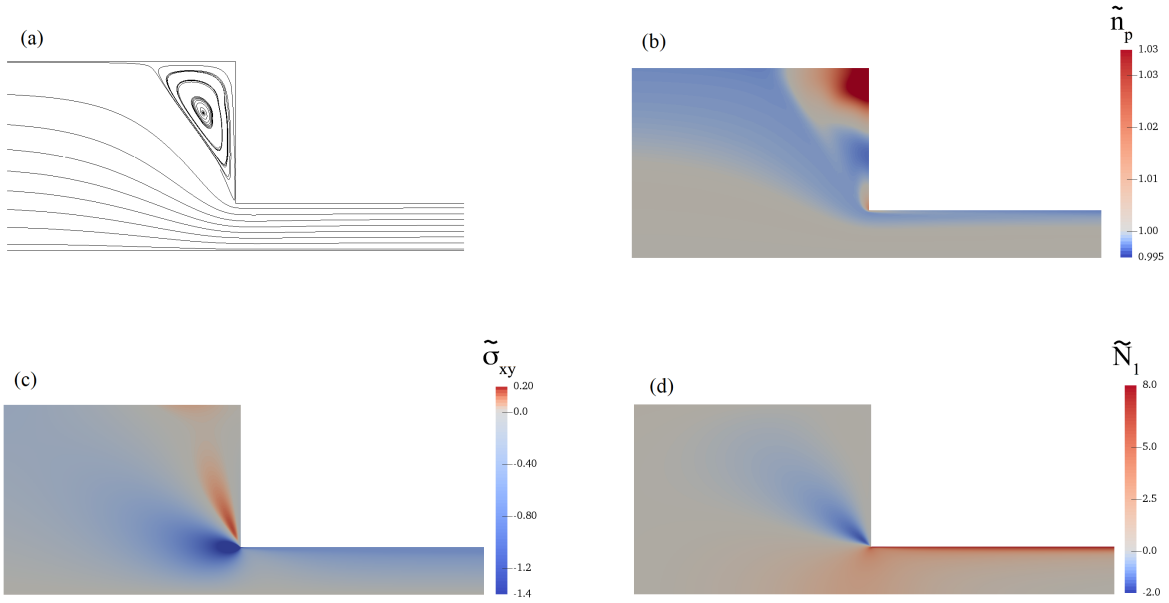

Figure 46: Contours of (a) stream function, (b) polymer number density, (c) shear stress, and (d) first normal stress difference for $De = 2.0$.

Fig. 47 shows the profiles for $De = 2$ at different vertical cross-sections of the channel before and after the contraction region. The results are compared with those obtained from Fig. 44. In Fig. 47(a), we can see the transition from parabolic flow to plug-like flow as the fluid flows from small deformation regime at the wide channel to the shear banding regime at the narrow channel. The increased polymer number density in the contraction region (Fig. 47(b)) is closer to the wall because of the larger De value. The shear stress profiles (Fig. 47(c)) qualitatively follow the same trend; however, the values are larger. The sharp profile of $\tilde{N}_1$ (Fig. 47(d)) is due to the shear band formation.

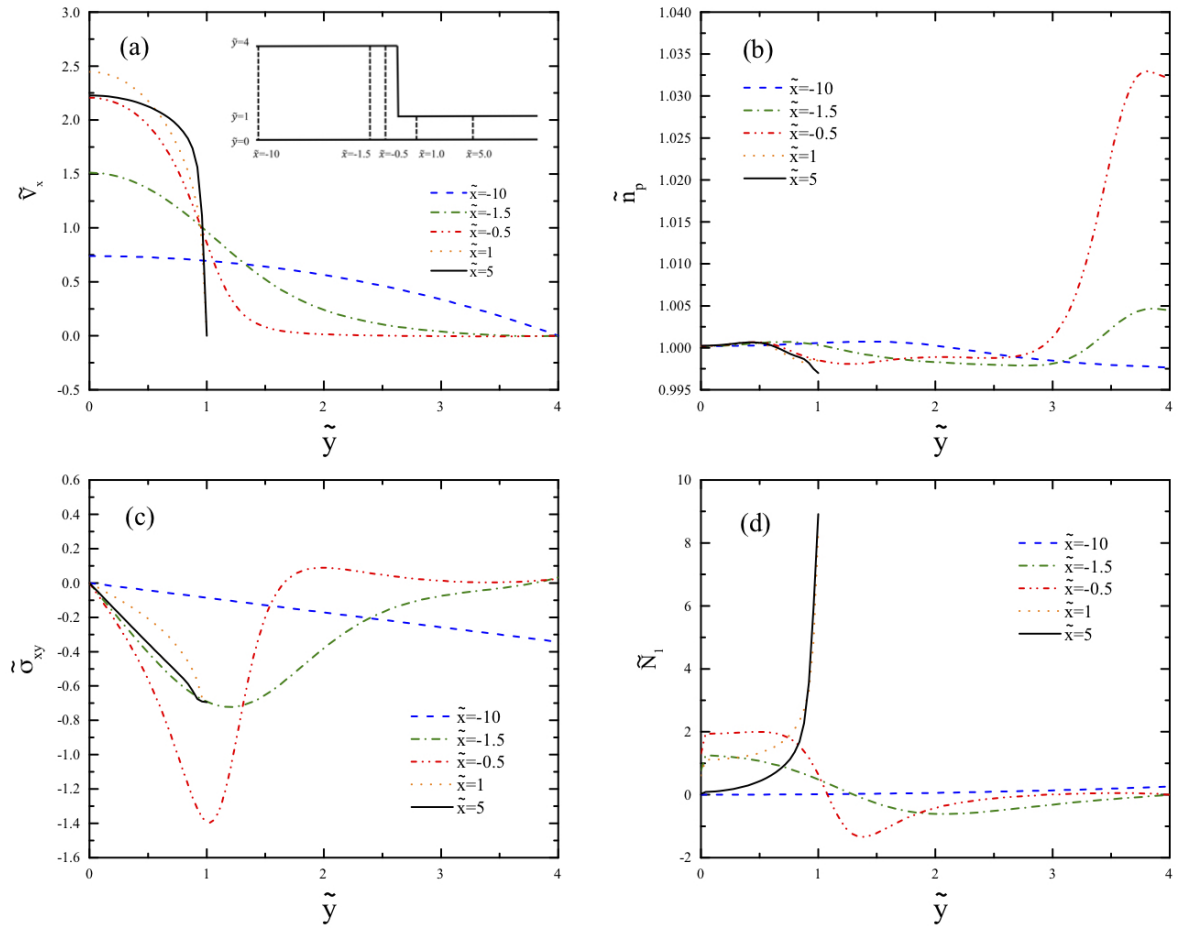

Figure 47: Cross-sectional profiles of (a) axial velocity, (b) polymer number density, (c) shear stress, and (d) first normal stress difference for $De = 2.0$. The selected $\tilde{x}$-values are the same as in Fig. 44.

Fig. 48 shows how the profiles change near the contraction region in different horizontal cross-sections. There is an overshoot of the axial velocity, as shown by Kim et al. (2005) for larger De. We see in Fig. 48(c) that $\tilde{\sigma}_{xy}$ undershoots before the contraction and overshoots after it, as already seen in Fig. 45 for $De = 0.5$.

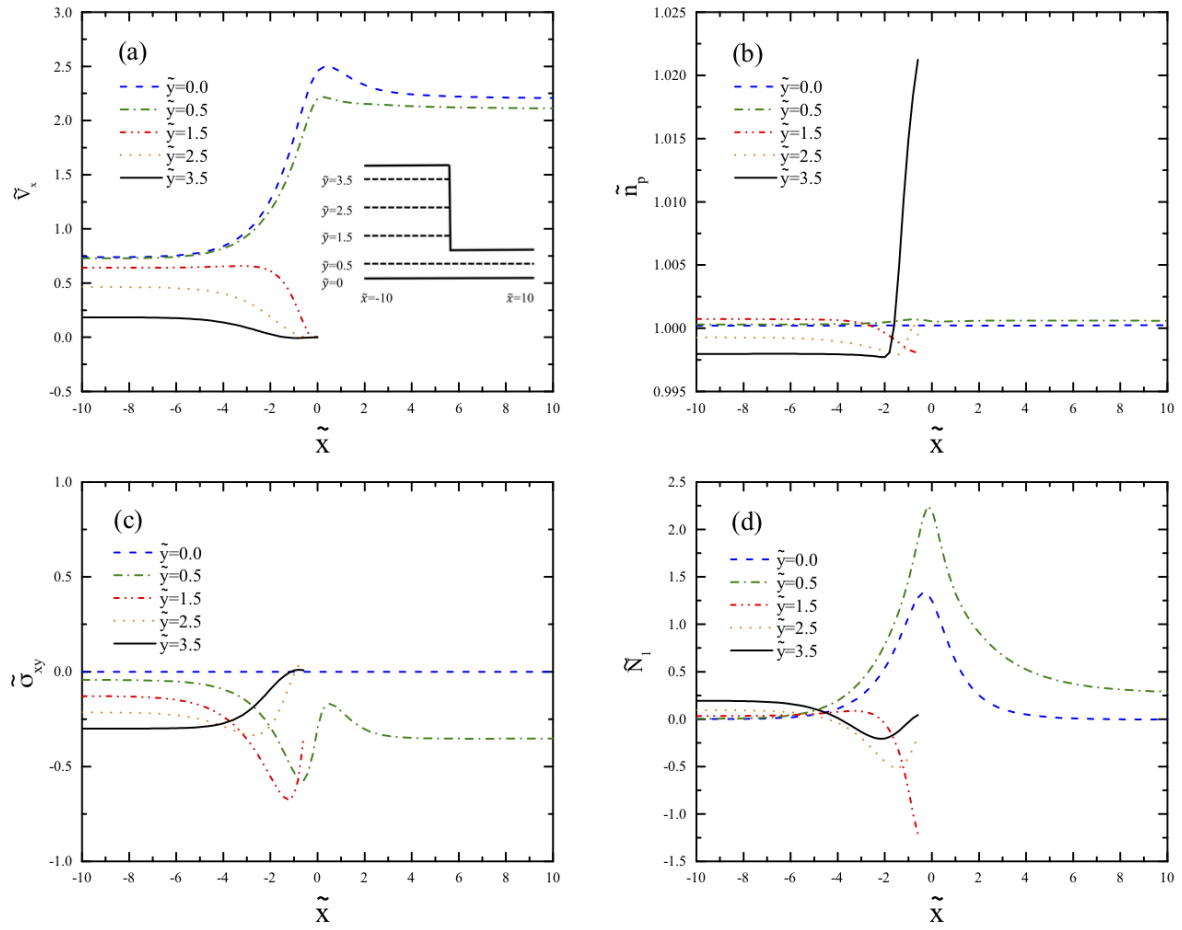

Figure 48: Cross-sectional profiles of (a) axial velocity, (b) polymer number density, (c) shear stress, and (d) first normal stress difference for $De = 2.0$. The selected $\tilde{y}$-values are the same as in Fig. 45.

5.4 Conclusion

The results of the contraction flow reveal that the size and the intensity of the corner vortex increase with the Deborah number as a result of shear-thinning, but they decrease after the onset of shear banding; these findings are in agreement with experiments. The axial velocity profile forms a plug-like shape in the shear banding regime after the contraction, where the local De number is much larger because of the decreased channel height. The kinks separating the velocity bands move toward the centerline as De increases. For the De values investigated in this work, the concentration of the polymer in the recirculation region is strongly increased. However, there is an increased effect of shear banding on $\tilde{n}_p$ at larger De, typically encountered in industrial processing flows.

6 Benchmark case no. 4: extrusion flow

6.1 Introduction

Entangled polymeric materials exhibit various phenomena when passed through a die. A prominent example is the extrudate swell, which is characterized by the expansion of the extrudate after leaving the die (Allain et al., 1997; Karapetsas and Tsamopoulos, 2008). A rapid increase in the volumetric flow rate (Fig. 49) is initially noticed as the pressure drop is increased (Achilleos et al., 2002a; Hill et al., 1990; Hatzikiriakos and Dealy, 1992; El Kissi et al., 1997). By further increasing the pressure drop, the extrudate surface demonstrates first periodic distortions with short wavelengths and small amplitudes, called sharkskin (Denn, 2001; Sornberger et al., 1987). Then, it temporary switches between sharkskin and smooth flow, named slip-stick, which is followed by unsteady flow with long-wavelength distortions, and finally, melt fracture. The sharkskin and slip-stick are surface distortions, while the wavy and gross melt fractures are volume instabilities as they involve the whole extrudate (Koopmans and Molenaar, 1998; Agassant et al., 2006; Vergnes, 2015). Whether these regimes are desired or not depends on the specific application. For instance, one tries to avoid sharkskin in plastic manufacturing, whereas it is advantageous in the processing of spaghetti since it helps the tomato sauce sticks to the product.

The origin of the extrusion instabilities is still a controversial topic even though it has been studied for the past fifty years. These instabilities may originate from the singularity at the die exit, the slip on the surface of the die, or the constitutive equation. The die exit singularity emerges as the zero velocity at the wall meets the free surface, which leads to sudden extensional gradients. In numerical computations, the singularity effect is stronger for a finer mesh since the solution is closer to the location of the stress singularity. The sharp corners are often rounding to avoid numerical problems (Inn et al., 1998; Arda and Mackley, 2005). In the review by Denn (2001), wall slip was classified into an adhesive failure of the polymer chains at the wall and a cohesive failure due to the

shear-induced chain disentanglement, resulting in a low-viscosity region near the wall. However, it is still unclear whether the wall slip delays (Sornberger et al., 1987; Ramamurthy, 1986; El Kissi et al., 1994; Achilleos et al., 2002b) or suppresses (Ghanta et al., 1999; Migler et al., 2002) the extrusion instabilities. The constitutive instability was explained by the existence of multiple steady-state shear rates for the same shear stress at the decreasing part of the homogeneous flow curve, resulting in different spatial regions with constant shear rates (Cao et al., 2015). Whether or not the underlying homogeneous flow curve should be described as nonmonotonic remains an open question. Shear banding can also be successfully predicted by two-fluid models accounting for stress-induced migration (Germann, 2019).

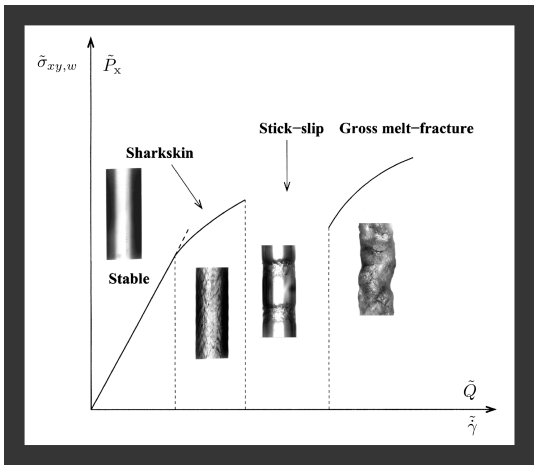

Figure 49: Instability regions in the flow curve of an extrusion flow [modified from Achilleos et al. (2002b), Fig 1].

A few numerical studies have been conducted to examine the effect of viscoelasticity during extrusion. For instance, the extrudate swell phenomenon was studied by applying the UCM (Bush et al., 1984; Crochet and Keunings, 1980), Oldroyd-B (Crochet and Keunings, 1982; Clermont and Normandin, 1993; Russo and Phillips, 2011), and Giesekus (Comminal et al., 2018) models. These studies indicate that the value of the swell ratio slightly decreases in the low-shear-rate regime compared to the Newtonian case, and it increases as the Deborah number is further increased. The local minimum is related to both shear thinning and elastic recoil (Comminal et al., 2018). In the analytical study of Tanner (1970), the swell ratio was expressed in terms of the ratio of the first normal stress difference to the shear stress. Konaganti et al. (2015) assessed the predictive capability of multimode differential and integral viscoelastic models by quantitative comparison with experiments. Although all the material functions

were the same for the differential and integral versions of a given model, the swell predictions greatly differed. Further research is required to find out the exact reason. Finally, by using a multimode version of the Rolie-Poly model, Robertson et al. (2017, 2019) conducted finite element simulations to study the effect of chain orientation and stretch at higher shear rates.

In our model, we associated shear banding with shear-induced migration and not the result of a nonmonotonic flow curve. This chapter aims to discuss the effect of shear banding, which was comprehensively reviewed by Germann (2019), on the extrudate swell phenomenon. It would be interesting to investigate which of the various extrusion phenomena mentioned above could be captured by our model or an improved version of it. However, with our current numerical solution approach, we cannot go into the non-stationary regime. Hence, we stick to the stationary laminar regime where we can see the characteristic fast increase in the flow rate upon increasing the pressure drop.

6.2 Numerical method

We solved the model Eqs. (31)–(33), and (42)–(45) for steady, laminar, and incompressible planar flow through a planar die. In addition, we replaced Eq. (49) with Eq. (97). As the variation in the polymer concentration is very small here, Eq. (37), or Eq. (49) in the dimensionless form, is difficult to solve with a lower-order discretization method. Therefore, we neglected the left-hand side and used the value of the previous iteration for the calculation of the Laplacian term. A schematic diagram of the flow geometry is shown in Fig. 50. The die was long enough to ensure fully developed flow. The half-width of the die, H, is considered as the characteristic height. The lengths of the upstream and downstream are denoted by L_1 and L_2, respectively, where $L_1 = L_2 = 25H$. The Cartesian coordinate system is used as the reference frame with origin at the intersection of the centerline and the die exit.

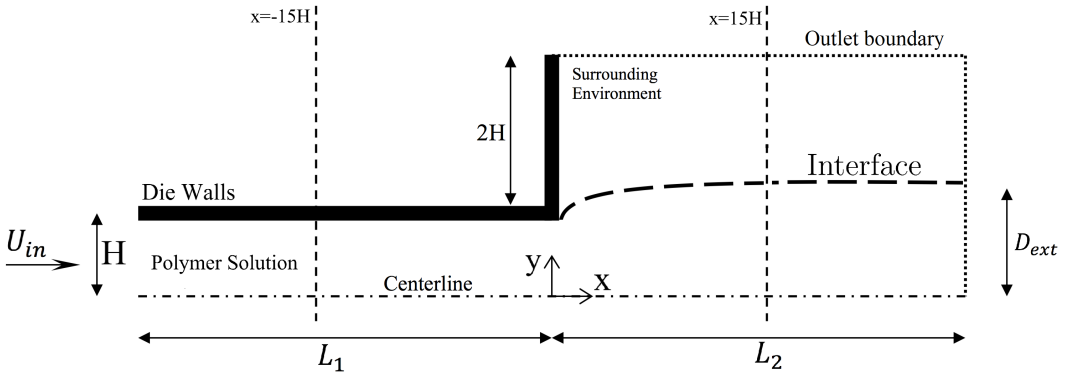

Figure 50: Geometrical sketch of extrudate flow through planar die.

We will use non-dimensional quantities in the sequel. The location is given by the characteristic height, $\tilde{\mathbf{y}} = \mathbf{y}/H$;

the time is given by the characteristic relaxation time, $\tilde{t} = t/\lambda_1$; the extra stress is given by $\tilde{\boldsymbol{\sigma}} = \boldsymbol{\sigma}/G_0$; and the conformation tensor associated with the polymer is defined by $\tilde{\mathbf{C}} = (K/n_p k_B T)\mathbf{C}$. The number densities of the polymer and the solvent are normalized using the values at equilibrium state as $\tilde{n}_p = n_p/n_p^0$ and $\tilde{n}_s = n_s/n_s^0$, respectively. The dimensionless parameters regarding these definitions are the ratio of the molecular weight of the solvent to that of the polymer, $\chi = M_s/M_p$; the viscosity ratio $\beta = \eta_s/\eta_0$, with $\eta_0 = G_0\lambda_1$ being the zero shear viscosity; and the ratio of the characteristic relaxation times $\epsilon = \lambda_1/\lambda_2$. For comparison's sake, we defined the Deborah number $De = 3\lambda_1 U_{in}/H$ and the Reynolds number $Re = \rho U_{in} H/\eta_0 = E^{-1}De/3$, where U_{in} denotes the inlet velocity and $E = G_0\lambda_1^2/(\rho H^2)$ denotes the elasticity number. As in Comminal et al. (2018), we did not consider the surface tension in our simulations. Similarly, the density and the viscosity of the surrounding environment are given by $\rho_{se} = 10^{-2}\rho$ and $\eta_{se} = 10^{-6}\beta\eta_0$, respectively. The total polymer concentration corresponds to the initial uniform polymer concentration and is given in weight percent by $\mu = \tilde{n}_p^0/(\tilde{n}_p^0 + \chi\tilde{n}_s^0)$. The dimensionless diffusion coefficients are denoted by $\tilde{D} = D\lambda_1/H^2$ and $\tilde{D}_{nonloc} = D_{nonloc}\lambda_1/H^2$. The non-dimensional form of the model equations is provided in Sec. 2.3.

The values of the model parameters are the same as those applied in Sec. 2.4. We determined them by fitting the flow curve of the shear stress against the shear rate with shear experiments of a 10 wt/wt% 1.6 M shear-banding polybutadiene solution (Cheng and Wang, 2012). The parameters are the mobility factor, $\alpha = 0.73$, the ratio of the characteristic relaxation times, $\epsilon = 0.0025$, the power-law factor, $q = 1.46$, the viscosity ratio, $\beta = 10^{-4}$, and the ratio of the molecular weight of the solvent to that of the polymer, $\chi = 10^{-1}$. The Reynolds number was set to $Re = 0.01$. A moderate non-dimensional nonlocal diffusion coefficient $\tilde{D}_{nonloc} = 10^{-3}$ was utilized to obtain a smooth transition region between the velocity bands and to guarantee a unique solution. In preliminary tests, the non-dimensional local diffusion constant did not affect the steady-state solution. Therefore, we used a relatively large value of $\tilde{D} = 10^{-3}$ to avoid long computing times. Detailed information about the roles of the local and nonlocal diffusion coefficients in our model can be found in Sec. 3. The predictions of the viscometric functions are provided in Fig. 51. Both the shear stress and the first normal stress difference increase monotonically with the shear rate (Fig. 51(a)). The uniaxial extensional viscosity shows a plateau followed by mild extension thickening and thinning (Fig. 51(b)).

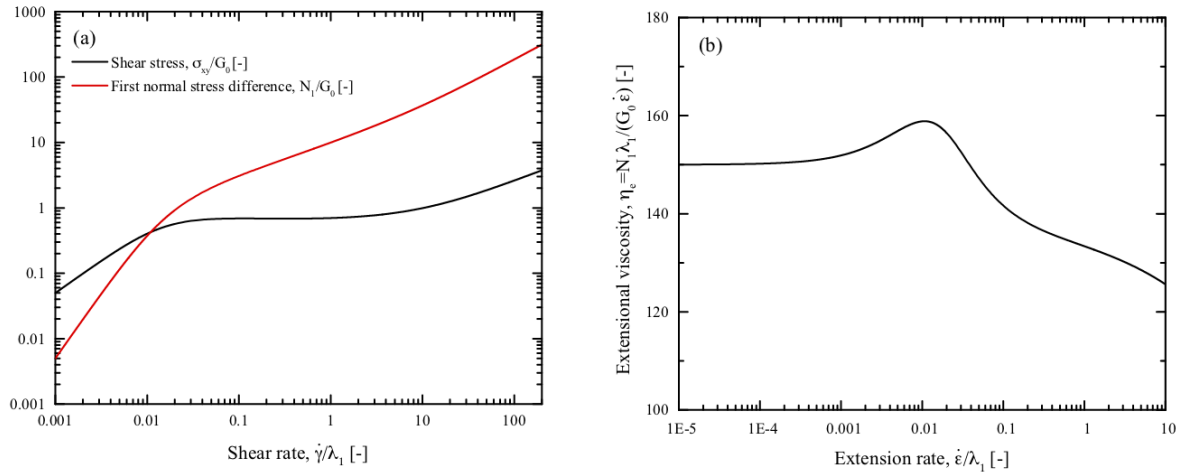

Figure 51: (a) Dimensionless shear stress and first normal stress difference vs dimensionless shear rate in homogeneous simple shear flow. (b) Dimensionless viscosity vs dimensionless extension rate in homogeneous uniaxial extension.

Transient simulations were performed by utilizing the OpenFOAM v4.0 finite volume package with the viscoelastic toolbox RheoTool version 2.0 (Pimenta and Alves, 2018). Based on the volume-of-fluid (VOF) method, we employed the rheoInterFoam solver to simulate the two-phase flow. By applying the differential velocity as an intermediate variable similar to the approach of Guo et al. (2014), the two-fluid model was implemented and validated in Sec. 5. The stress-velocity coupling described in Pimenta and Alves (2017) and available in the Rheotool package v.2.0 was utilized to stabilize the momentum equation. The convective terms were discretized using the high-resolution convergent and universally bounded interpolation scheme for the treatment of advection (CUBISTA), followed by a component-wise and deferred correction approach. The diffusion terms and the spatial gradients of the velocity and pressure fields were discretized using the Gauss linear scheme. We applied the Euler method to discretize time. The discretized flow problem was iteratively solved by employing the PIMPLE algorithm with ten inner iterations per time step. We applied the multidimensional universal limiter with explicit solution (MULES) for the indicator variable of the VOF method, the geometric-algebraic multi-grid solver for the pressure, and the biconjugate gradient solver with an incomplete lower-upper decomposition for the remaining variables. At each time step, the absolute tolerance for the variables was 1.0×10^{-10}.

The MULES solver is used to account for the compressive flux in the interface to minimize diffusion (Deshpande

et al., 2012). In the VOF method, the distribution of the phases is defined by the color function:

$$\phi(x,t) = \begin{cases} 1 & \text{for a cell containing only the fluid phase with viscosity } \eta_1 \text{ and density } \rho_1, \\ 0 & \text{for a cell containing only the surrounding air phase with viscosity } \eta_2 \text{ and density } \rho_2. \end{cases} \tag{98}$$

The liquid volume fraction Θ represents the volume average of $\phi(x,t)$ in each cell of the computational domain:

$$\Theta = \frac{1}{V_\Omega} \int_\Omega \phi(x,t) dV \,, \tag{99}$$

with $V_\Omega = \int_\Omega dV$ being the total volume of the cell Ω. Some of the material properties are averaged using the arithmetic rule of mixtures, such as:

$$\eta = \Theta\eta_1 + (1-\Theta)\eta_2, \tag{100}$$

$$\rho = \Theta\rho_1 + (1-\Theta)\rho_2. \tag{101}$$

The liquid volume fraction is described by a transport equation as the color function is advected with the flow. The mass is conserved directly by the VOF method since it solves a transport equation of the color function. The transport equation can be solved by geometric method with a sharp interface, and algebraic method. In the latter case, the numerical diffusion arising from the discretization of the transport equation smooths the jump of the color function across the interface. Thus, the position of the interface spreads over a few cells and the interface is not sharp anymore. However, we can mention some advantages of the algebraic over the geometric method such as less computational costs, as well as more straightforward implementation on unstructured meshes and extension to higher dimensional computational domains. The geometric VOF method consists of a reconstruction of the interface and an advection scheme. It is called geometric since the liquid volume fraction is updated through calculations of polynomial intersections (Comminal et al., 2018). The algebraic VOF scheme directly solves the transport equation of the color function

$$\frac{\partial \phi}{\partial t} + \nabla \cdot (\mathbf{v}\phi) = 0 \,. \tag{102}$$

This equation states that the algebraic VOF method can be coupled with the set of time evolution equations. In the MULES solver, the advection part of Eq. (102) is modified so that a multiplied constant is defined to be one at the interface and zero elsewhere. Consequently, the interfacial compression flux is solved only at the interface and reduces both the numerical diffusion at the interface and the computational costs (Deshpande et al., 2012).

The die was filled with the resting polymer solution at the initial time. At the inlet boundary, we imposed a constant polymer number density corresponding to its equilibrium value in the state of test, i.e., $\tilde{n}_p = 1.0$, and a constant inlet velocity. Similarly, we utilized a zero tensorial value for the stress and unity for the polymer conformation. The differential velocity must be zero for these uniforconditions. At the walls, we applied the no-slip and no-flux conditions for the total and differential velocities. We used the Neumann condition for the polymer number density. Using the linearExtrapolation boundary condition available in the RheoTool version 2.0, the conformation and stress tensors were linearly extrapolated along the walls (Pimenta and Alves, 2018). For the outer periphery of the expansion region, we applied an outlet Neumann boundary condition. At the liquid/air interface, we assumed a zero pressure and applied the Neumann condition on the other variables. Since no asymmetry was observed relative to the channel centerline in our preliminary calculations, we only solved the flow for the upper half to avoid unnecessary computations. Moreover, we used the symmetry boundary condition for all the variables at the centerline.

The meshes M1, M2, M3, and M4 considered in this study comprise 12230, 48920, 195680, and 782720 cells, respectively. The mesh M1 is available in the DieSwell tutorial of the RheoTool v2.0 (Pimenta and Alves, 2018) while the meshes M2, M3, and M4 can be generated by successive refinement. Comminal et al. (2018) validated the solution methodology presented in this tutorial as well as the corresponding mesh.

6.3 Results

We solved our model for Deborah numbers ranging from 0.25 to 6. The extrudate swell ratio is given by $S_r = D_{ext}/H$, where D_{ext} denotes the extrudate width. In Fig. 52(a), we plotted the S_r values against the De number, calculated using our model and the non-shear banding Giesekus model ($\alpha = 0.2$ and $\beta = 1/9$). The agreement with the numerical data obtained for Rheotool by Comminal et al. (2018) is very good. This is to expect as we utilized the same mesh and employed the same software package. Nevertheless, as noted by Comminal et al. (2018), there are significant variations between different numerical schemes, which deserves future research. Convergence was observed for the meshes M1 and M2, and, a much higher spatial resolution was obtained inside the flow field with the mesh M3. Although the trend is very similar for M3, numerical artifacts cause slight deviations, especially at $De = 2$.

Our model calculations performed with the mesh M3 show non-stationary ripples close to the free surfaces, which Comminal et al. (2018) also observed in some of their simulations. Nevertheless, because of the higher resolution, we decided to utilize the mesh M3 in most of our subsequent simulations.

We find that both models predict an initial decrease of S_r. The occurrence of a local minimum was experimentally verified for various synthetic polymer melts, including melts of monodisperse and bidisperse polystyrenes (Robertson et al., 2017, 2019) and high-density polyethylene (Behzadfar et al., 2015), and is related to both shear thinning and elastic recovery. The presence of an undershoot was also reported for various viscoelastic models (Comminal et al., 2018; Wesson and Papanastasiou, 1988; Chang and Yang, 1994; Phan-Thien, 1988; Robertson et al., 2017, 2019). However, the decrease of our model is possibly too strong, which we relate to excessive shear thinning and the use of a single set of long and short relaxation times, λ_1 and λ_2, respectively. More importantly, the only modest increase in the shear banding regime needs to be experimentally verified for shear banding polymer solutions. Comminal et al. (2018) used the Carreau model and showed a drop from $S_r = 1.192$ to about 0.993 as the shear-thinning parameter n decreased from 1 to 0.2. The Oldyord-B model only exhibited a tiny decrease below the Newtonian value as this viscoelastic model does not account for shear thinning. In the same article, the behavior of the Giesekus model is analyzed for different values of the anisotropy constant α. The minimum of S_r was further decreased to around 1.1 and shifted to a larger De value by increasing α from 0.2 to 0.5, i.e., by enhancing shear-thinning and second normal stress effects. The value of α utilized in our model calculations was 0.73, i.e., significantly larger than the two values examined in their paper. Therefore, we have an even stronger decrease. Using a multimode version of the Giesekus model, Konaganti et al. (2015) observed that the slope of the curve was still smaller at higher shear rates than expected from experiments. Robertson et al. (2017, 2019) used the Rolie-Poly model with a spectrum of relaxation times and calculated the swelling ratio for shear rates starting slightly before the occurrence of the local minimum. The predictions captured the experimental data very well over a broad shear-rate range, including the minimum extrudate swell ratio of about 1.1. As the structure of our constitutive equation is similar to that of the Rolie-Poly model, we believe that we can improve our model predictions by using a spectrum of relaxation times.

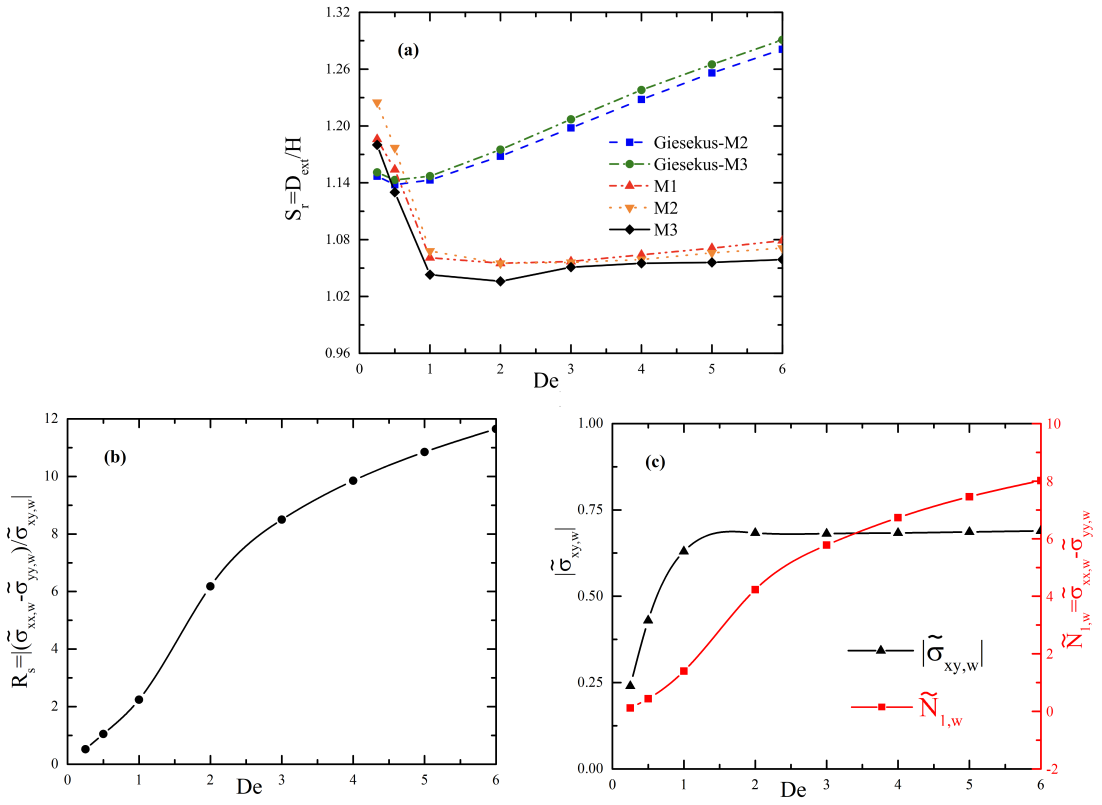

Figure 52: (a) Swell ratio, (b) recoverable shear property at wall, and (c) absolute value of shear stress and value of first normal stress difference at wall plotted against De number. In Fig. 52(a), the results are shown for different meshes to verify mesh independency and compared with the non-shear banding Giesekus model ($\alpha = 0.2$ and $\beta = 1/9$).

According to Tanner (1980), S_r can be expressed as a function of R_s, defined as the ratio of the magnitude of the first normal stress difference to the shear stress evaluated at the wall. We can see in Fig. 52(b) that R_s increases monotonically with De. The rate of the increase decreases at the onset of shear banding. The individual trends of the first normal stress difference at the wall, $\tilde{N}_{1,\mathrm{w}} = \tilde{\sigma}_{\mathrm{yy,w}} - \tilde{\sigma}_{\mathrm{xx,w}}$, and the wall shear stress, $\tilde{\sigma}_{\mathrm{xy,w}}$, are depicted in Fig. 52(c). Here, we can see the shear banding plateau in the shear stress curve and note that the shape of R_s closely follows the trend of the first normal stress difference. A comparison to the experimental data is needed to quantitatively assess the effect of shear banding on R_s and S_r. Allain et al. (1997) reported experimental data for semidilute polymer solutions; however, the concentration of the polymer was too small to be in the shear banding regime despite the extremely high molecular weight.

In Fig. 53(a)-(d), we see the profiles of the axial velocity, the polymer number density, the shear stress, and the first normal stress difference, $\tilde{N}_1 = \tilde{\sigma}_{xx} - \tilde{\sigma}_{yy}$, respectively, at $\tilde{x} = -15$. The cross-section is selected to neglect the effects of the inlet and the die exit region. In these plots, $\tilde{y} = 0$ and 1 represent the centerline and the solid wall of the die, respectively. The velocity profile changes from parabolic in the low-shear rate regime to plug-like at $De \approx 2$.

This change is related to the onset of shear banding. The kink separating the velocity bands moves toward the center of the channel as De is further increased, which can be explained by the effect of stress-induced migration. Two bands are also evident in the polymer concentration at $De = 2$; the polymer concentration assumes a large plateau value near the centerline and a sharply decreasing band near the wall. The differences observed in the polymer number density are extremely small. We do not show the polymer concentration for the larger De values considered in this work since a significantly more refined mesh would be needed to resolve the transition region between the bands accurately. The results presented in Fig. 53(a)-(b) can be explained by the different types of diffusion. In the low-shear-rate regime where the Fickian diffusion is the major mechanism, the polymeric constituents diffuse from the region with more to less concentration; i. e., from the center to the wall. However, the opposite trend exists in the shear banding regime. Here, the dominant diffusion mechanism is stress-induced migration, pushing the velocity kink towards the centerline. For pressure-driven channel flow, the value of $\tilde{\sigma}_{xy}$ is zero at the centerline, and it increases linearly to the maximum value at the wall (see Sec. 4). The absolute wall shear stress is increased for increasing De values. The overlap of these profiles in the shear banding regime is expected from the plug-like velocity profiles, where the similar shear rates of the bands result in similar stress profiles in the plateau regime of the flow curve. The small difference in the bands comes from the relatively narrow examined De range. In the shear banding regime, the profile of the shear stress indicates nonlinearity near the wall if the resolution of the mesh is not high enough. Consequently, the mesh M4 was used to obtain Fig. 53(c). Finally, the first normal stress difference is larger for larger De values. The value of $\tilde{N}_1$ is zero at the centerline, and it increases as the wall is approached. This increase is especially strong in the shear banding regime.

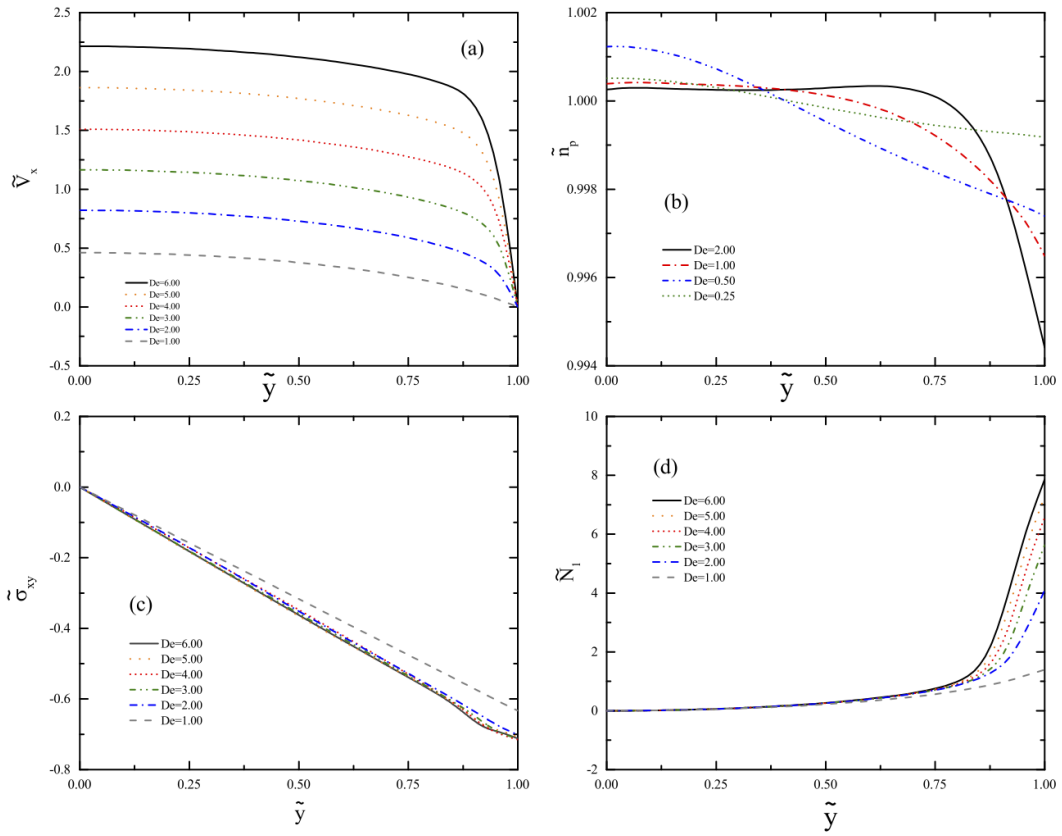

Figure 53: Profiles of (a) axial velocity, (b) polymer number density, (c) shear stress, and (d) first normal stress difference evaluated at $\tilde{x} = -15$ for different values of De number.

Fig. 54 illustrates the results for the case $De = 0.25$ at different vertical cross-sections before and after the die exit. As expected for an extrusion flow, Fig. 54(a) shows that the velocity profile changes from the parabolic profile in the channel to a more uniform pattern after the channel exit. The zero velocity at the die wall suddenly reaches the free surface, which leads to sharp extensional acceleration. Consequently, the centerline velocity decreases to satisfy mass conservation (Richardson, 1970; Agassant et al., 2006; Burghelea et al., 2010). Since we are in the low-shear-rate regime, the velocity profile in the die is parabolic. Fig. 54(b) depicts the profiles of the polymer number density in different vertical cross-sections. As the polymer reaches the expansion region, a decrease is observed in the direction of the interface to satisfy the mass conservation in the liquid phase. In addition, this non-uniform profile can be described using the non-zero value of the component $\tilde{\mathrm{v}}_y$ though it is very small compared to $\tilde{\mathrm{v}}_x$. As expected from a fully developed Poiseuille flow, Fig. 54(c) demonstrates that the profile of the shear stress is linear when it is further away ($\tilde{x} = -5$). The first normal stress difference increases around the die exit, whereas it decreases as the material exits the die (Fig. 54(d)). Since the velocity in the free surface region is uniform, the shear and extensional stresses are zero at $\tilde{x} \geqslant 5.0$.

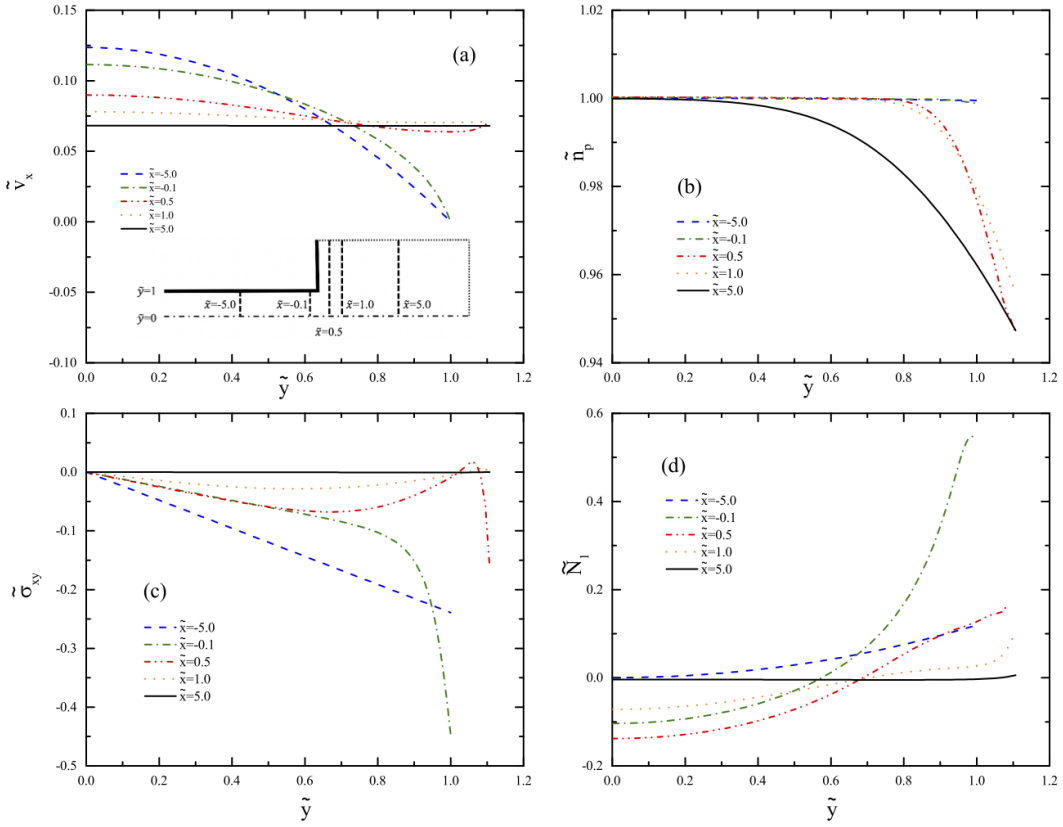

Figure 54: Vertical profiles of (a) axial velocity, (b) polymer number density, (c) shear stress, and (d) first normal stress difference calculated for $De = 0.25$.

Fig. 55 shows the profiles at different vertical cross-sections of the channel before and after the die exit region for $De = 6$, which is in the shear banding regime. The velocity profile changes from the plug-like profile in the channel to the uniform profile after the die exit. The profile of the polymer concentration is also banded; however, the effect is negligible compared to the large concentration changes which occur as a result of the expansion at $\tilde{x} = 5$. The other results are qualitatively similar to those obtained for $De = 0.25$ (Fig. 54) while the magnitudes of the variables are larger. As shown in Fig. 58(c)-(d), the decrease of the shear stress slightly before the die exit near the die wall is consistent with the stress polarization. Since the extensional forces have been already relaxed in the die flow due to the large De value, the profiles of the first normal stress difference at the fully developed die channel and immediately before the die exit are similar.

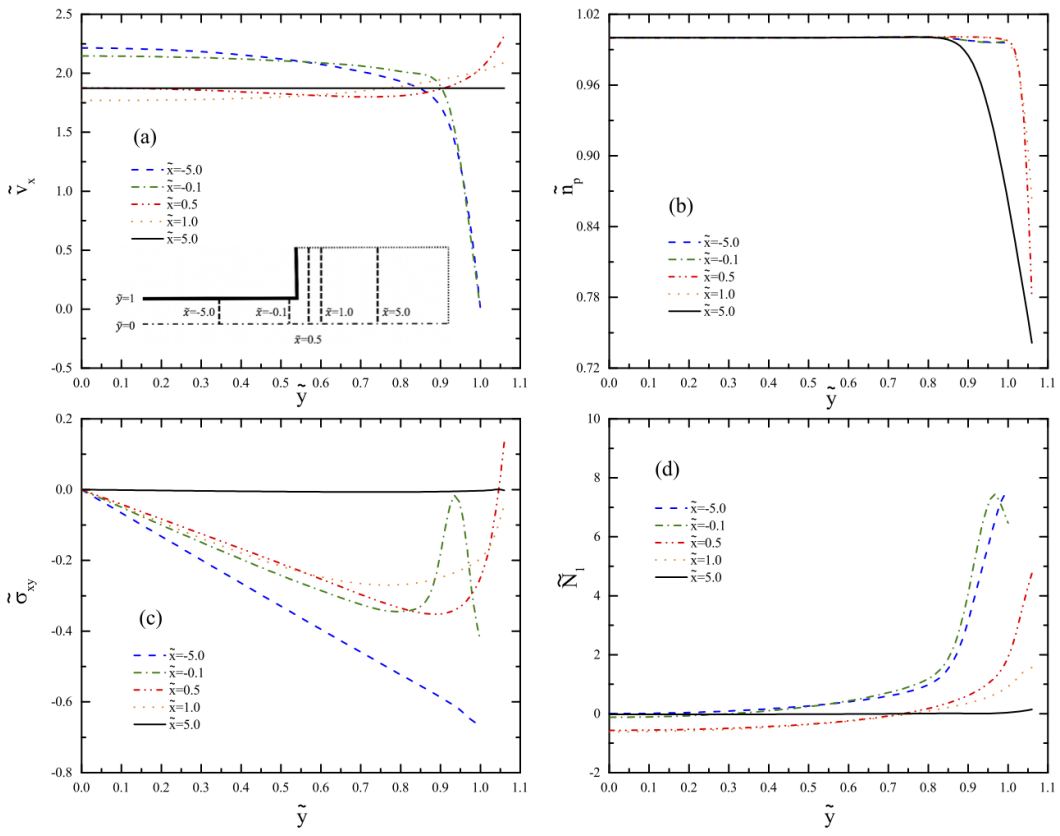

Figure 55: Vertical profiles of (a) axial velocity, (b) polymer number density, (c) shear stress, and (d) first normal stress difference calculated for $De = 6$.

Fig. 56 illustrates the profiles in a cross-section parallel to the centerline at $\tilde{y} = 0.5$. Because the important changes happen in the die exit region, we depict only the part of the channel in the range $-10 \leqslant \tilde{x} \leqslant 10$. The axial velocity decreases at the die exit to form the uniform profiles of the free surface flow outside the die (Fig. 56(a)). We can see in Fig. 56(b) that after the die exit, the concentration of the polymers is larger for larger De along the selected cross-selection, whereas the trend was vice versa if the cross-section was closer to the centerline. The decrease of the velocity occurs after an overshoot and an undershoot at larger De, which was also observed by Venet and Vergnes (2000) for a multimode version of the exponential Phan-Thien and Tanner model. In addition, they detected the stress peak in the vicinity of the die exit, as shown in Fig. 56(c). The die exit effect appears as an overshoot in the profile of the first normal stress difference at large De (Fig. 56(d)) where the material leaves the die. In the free surface flow where the profiles are uniform, the shear and normal stresses are zero.

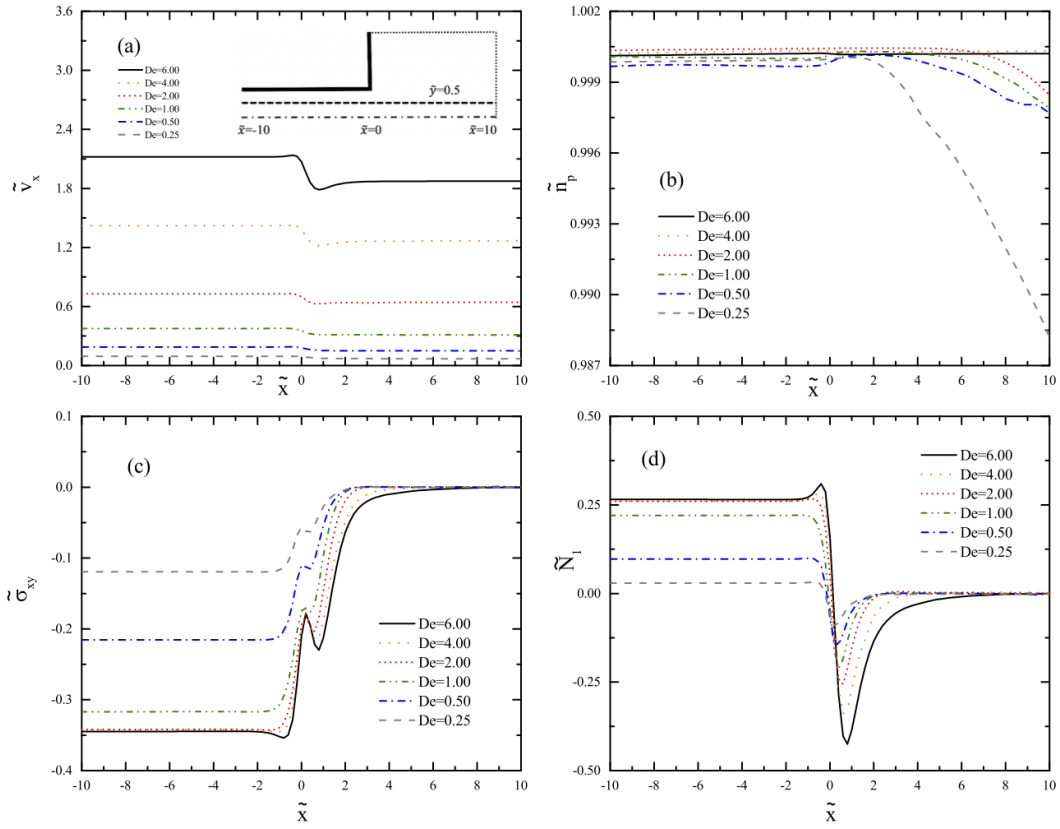

Figure 56: Profiles of (a) axial velocity, (b) polymer number density, (c) shear stress, and (d) first normal stress difference for different values of the De number at the horizontal cross-section $\tilde{y} = 0.5$.

Fig. 57 depicts the contours of the flow for $De = 0.25$. We can observe that the results calculated using the mesh M2 (on the left) agree with those calculated using the mesh M3 (on the right). The slight surface distortions seen in the contour plots obtained for M2 are related to the surface generation procedure applied by the open-source postprocessing software ParaView. As already mentioned, the resolution obtained with M3 is higher inside the extrudate. However, numerical artifacts appear as non-stationary ripples in the interfacial areas. Since the difference in the polymer number density is extremely small here, we only comment on the major trends. From the discussion of Fig. 53(b), we know that in the low-shear rate regime, the polymer number density is governed by Fickian diffusion. Consequently, there are no concentration bands (Fig. 57(a)-(b)). An important effect that we already noticed in Fig. 54 is the reduction of the polymer number density in the expansion region after the die. The shear stress increases from zero at the centerline to the maximum at the wall in the die and becomes zero at the die exit (Fig. 57(c)-(d)). There is a sign change in the shear stress close to where the die meets the free surface (Bush et al., 1984; Konaganti et al., 2016; Pettas et al., 2015; Venet and Vergnes, 2000). In agreement with the previous computational predictions (Crochet and Keunings, 1980; Bush et al., 1984; Salipante et al., 2017; Burghelea et al., 2010; Konaganti et al., 2016), the first normal stress difference is relatively small in the die as the flow is shear flow, and it becomes maximum at the die exit due to the stretching of the polymer as a consequence of transition from no-slip to free boundary condition (Fig. 57(e)-(f)). Since the flow has developed uniform velocity profiles, both the shear stress and the first normal stress difference are zero at the downstream away from the die exit. The negative values of the latter quantity near the centerline at the die exit are related to the local velocity deceleration.

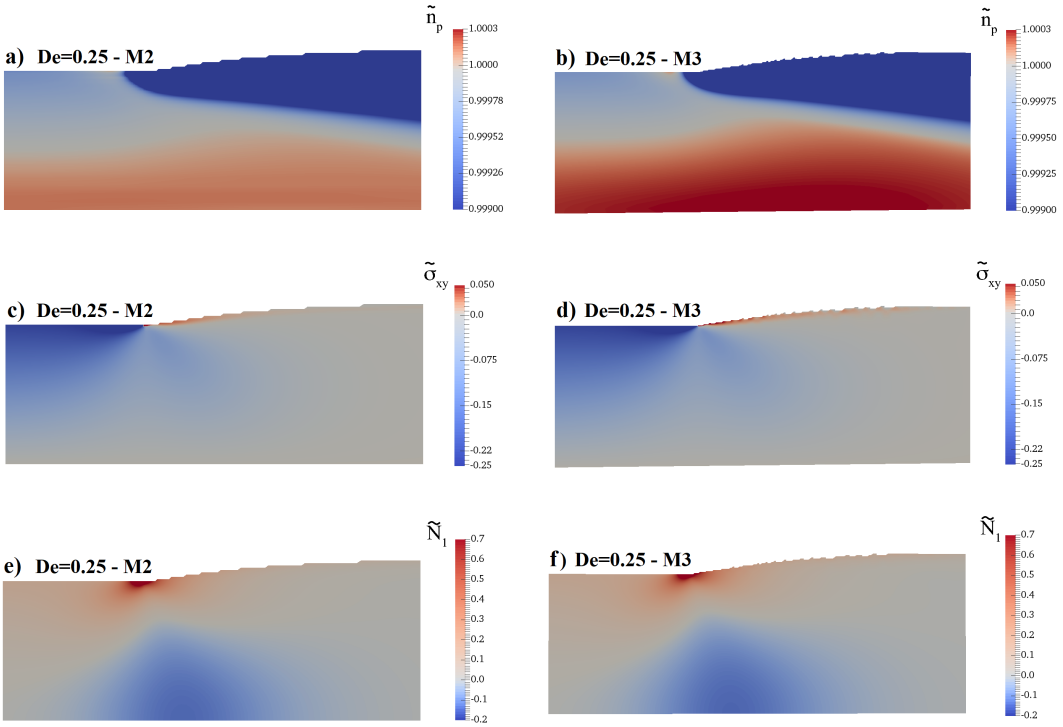

Figure 57: The contours of (a)-(b) polymer number density, (c)-(d) shear stress, and (e)-(f) first normal stress difference calculated for $De = 0.25$ using mesh M2 (left) and mesh M3 (right).

The contours shown for $De = 3$ in Fig. 58 are compared with the results of Fig. 57. For both De values, the polymer number density is reduced in the expansion region after the die. A fundamental difference to the low-shear rate case is the reduced polymer number density near the walls inside the channel. This phenomenon also occurs in a pure channel (as already observed in Sec. 4 and Sec. 5), i.e., in the absence of a free surface and is related to the presence of two concentration bands (Fig. 58(a)-(b)), as already noticed in Fig. 53(b). The trends of the shear stress (Fig. 58(c)-(d)) and the first normal stress difference (Fig. 58(e)-(f)) are qualitatively similar to what was observed in Fig. 57(c)-(f). However, the magnitudes are larger due to the increased De number. As aforementioned, the surface oscillations for the fine mesh have also been observed in other studies (Comminal et al., 2018, e.g.). These are numerical artifacts due to the approximations of the two-phase flow with the Eulerian surface-capturing approach.

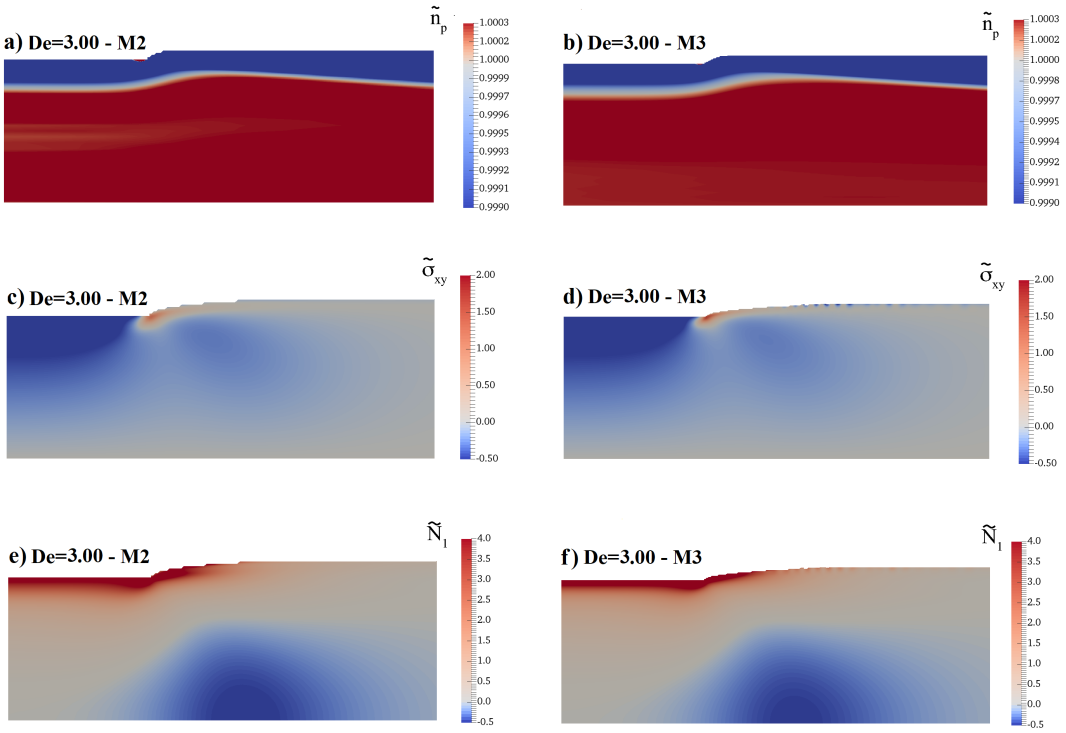

Figure 58: Contours of (a)-(b) polymer number density, (c)-(d) shear stress, and (e)-(f) first normal stress difference calculated for $De = 3$ using mesh M2 (left) and mesh M3 (right).

6.4 Conclusion

In this chapter, we studied and discussed shear banding in an extrusion flow using our recently developed two-fluid model for semidilute entangled polymer solutions. In this model, shear banding is associated with the stress-induced migration of the polymeric constituents. We observed a local minimum in the profile of the extrudate swell ratio against the Deborah number immediately after the Newtonian case. The subsequent increase is significantly reduced, which may be related to both the influence of shear banding and the use of a single set of long and short relaxation times, λ_1 and λ_2, respectively. Owing to the change in the boundary conditions from no-slip at the wall to the free surface condition, both the parabolic velocity profile in the low-shear-rate regime and the plug-like profile of the shear banding regime developed to uniform profiles at the downstream after the die exit. Consequently, the stresses demonstrate peaks at the die exit region, whereas they become zero after the die exit region. The vertical profiles of the polymer number density inside the channel closely follow that of the axial velocity. As a result of the stress-induced migration, we noticed plateau values followed by a sharp decrease in the polymer number density as the wall is approached. However, this effect was much smaller than the concentration changes observed after the die exit, which occurs as a result of the expansion. The results and the simplicity of our model encourage

us to study further types of mixed flows. To improve the model capabilities, we can extend it to multiple modes and make the defined parameters to depend on the polymer concentration. Finally, there is a lack of experimental work of extrusion swell on shear banding polymer solutions.

7 Summary and outlook

We developed a new two-fluid model for semidilute entangled polymer solutions using the generalized bracket approach of non-equilibrium thermodynamics to study rheological behaviors such as shear banding. The new model is based on the hypothesis that diffusional processes like Fickian diffusion and stress-induced migration are responsible for steady-state shear banding in semidilute entangled polymer solutions. The time evolution equation for the conformation tensor includes a nonlinear Giesekus relaxation, which accounts for the stress overshoot of a shear-banding material during the rapid start-up of simple shear flow and hydrodynamic interactions between the constituents of the solution. To capture the upturn of the flow curve at high shear rates, we developed a nonlinear relaxation term that resembles the term used in the Rolie-Poly model to account for CCR and chain stretch. Although stress diffusion is accounted for in this two-fluid approach, an additional stress-diffusive term had to be included to the conformation tensor equation to control the smoothness of the profiles.

The advantage of this two-fluid approach is that the differential velocity is treated as a state variable. Consequently, the additional boundary conditions arising from the higher diffusive derivatives in the time evolution equation of the differential velocity can be directly imposed with respect to this variable. For instance, no-slip and no-flux boundary conditions translate into the requirement that the tangential and normal components, respectively, of the differential velocity must be zero at the boundaries. Another advantage is that the total mass is conserved by the model equations themselves. Therefore, it is no longer necessary to explicitly impose a no-flux condition on the polymer concentration to prevent outflow material through the system boundaries. Because our model is relatively simple, it is an ideal candidate for use in more complicated flow simulations. We solved four flows with our model, namely a cylindrical Couette flow, a pressure-driven channel flow, a 4:1 contraction flow, and an extrusion flow.

We solved a cylindrical Couette flow to investigate the general behavior of the new model. We found that the steady-state solution is unique for different initial conditions and independent of the applied deformation history. Furthermore, the value of the local diffusivity constant has no significant effect on the steady-state solution. In agreement with the experiments of Callaghan and Gil (2000), velocity and concentration banding is predicted. Furthermore, we observed that stress-induced migration is responsible for shear band formation.

The computational results of the pressure-driven channel flow showed a plug-like profile of the velocity and concentration bands for the same range of pressure gradients. Increasing the value of the pressure gradient shifted the kink separating the shear bands to the center of the channel. The steady-state profile of the first normal stress

difference monotonically increased from the center of the channel to a maximum value at the walls. The value of the nonlocal diffusivity constant did not significantly influence the total velocity and the wall shear stress. The polymer concentration showed the same temporal behavior for different values of the nonlocal diffusivity constant. However, the steady-state solution was more uniform when we used larger nonlocal diffusivity constant. The results of the volumetric flow rate calculated using different values of the pressure gradient in the ramp-up and -down tests agreed, thereby confirming the uniqueness of the solution. This profile showed a spurt at a critical pressure gradient, as experimentally observed in the pressure-driven shear flows of polymeric materials. We also studied the effect of wall slip using the linear Navier slip model to illustrate how to account for slip in our two-fluid framework. We noticed that the slip velocity of the solvent had no significant effect on the solution, whereas changing the polymer slip vertically shifted the velocity profile.

The results of the contraction flow revealed that the size and the intensity of the corner vortex increase with the Deborah number as a result of shear-thinning, but they decrease after the onset of shear banding; these findings are in agreement with experiments. The axial velocity profile forms a plug-like shape in the shear banding regime after the contraction, where the local De number is much larger because of the smaller channel width. The kinks separating the velocity bands move toward the centerline as De increases. For the De values investigated in this work, the concentration of the polymer in the recirculation region is strongly increased. However, there is an increased effect of shear banding on $\tilde{n}_p$ at larger De, typically encountered in industrial processing flows.

The study of the extrusion flow showed a local minimum in the profile of the die swell ratio against the Deborah number immediately after the Newtonian case, which is followed by a positive slope that is very small as a result of shear banding. Owing to the change in the boundary conditions from no-slip at the wall to the free surface condition, both the parabolic velocity profile in the linear viscoelastic regime and the plug-like profile of the shear banding regime developed to uniform profiles at the downstream after the die exit. Consequently, the stresses demonstrate peaks at the die exit region, whereas they become zero after the die exit region. The polymers were more concentrated near the centerline in the linear viscoelastic regime since the dominant diffusional process is Fickian. However, the trend is more pronounced in the shear banding regime because of the stress-induced migration dominance. Moreover, this effect was much smaller than the concentration changes observed after the die exit, which occurs as a result of the expansion.

The results and the simplicity of the new model encourage us to analyze the model behavior in more complicated types of inhomogeneous flows. To do so, higher-order approaches can be implemented in the model to increase its

numerical capabilities. The model parameters can be defined to be dependent on the concentration or the molecular weight of the polymer. Furthermore, the model can have a more realistic spectrum of the relaxation times by for instance including additional component. To verify the hypotheses of the new model, and to assess the validity of the results, we need to conduct experiments such as PIV measurements to observe velocity profiles, and SANS and high-speed videography of labelled polymers to examine microstructural and conformational changes during flow.

Symbols

α	mobility factor
$\bar{\mathbf{r}}$	end-to-end vector of polymer chain
β	viscosity ratio
$\boldsymbol{\gamma}$	strain
$\boldsymbol{\Lambda}^1_{\alpha\beta\gamma\varepsilon}$	general fourth-order reptation relaxation tensor
$\boldsymbol{\Lambda}^2_{\alpha\beta\gamma\varepsilon}$	general fourth-order Rouse relaxation tensor
$\dot{\boldsymbol{\gamma}}$	shear rate
$\boldsymbol{\sigma}$	total stress
$\boldsymbol{\sigma}^p$	extra stress associated with the polymer
$\boldsymbol{\sigma}^s$	viscose stress
$\boldsymbol{C}$	polymer structural tensorial parameter density
$\boldsymbol{c}$	polymer conformation tensor
$\boldsymbol{D}$	symmetric velocity gradient tensor
$\boldsymbol{I}$	identity tensor
$\boldsymbol{N_1}$	first normal stress difference
χ	ratio of the molecular weight of the solvent to that of the polymer
χ_L	size of the lip vortex in the contraction flow
χ_R	size of the corner vortex in the contraction flow
Δp	pressure gradient
$\dot{\gamma}_1$	shear rate of the plateau beginning
$\dot{\gamma}_2$	shear rate of the plateau end

ϵ	ratio of the characteristic relaxation times
ϵ'	Rolie-Poly model parameter controlling the strength of CCR
η	dynamic viscosity
η_0	zero shear viscosity
η_p	polymer viscosity
η_s	Newtonian solvent viscosity
λ_1	reptation relaxation time
λ_2	Rouse relaxation time
$\mathbf{\Delta m}$	differential momentum density
$\mathbf{\Delta v}$	differential velocity
$\mathbf{m}$	total momentum density
$\mathbf{m}^p$	polymer momentum density
$\mathbf{m}^s$	solvent momentum density
$\mathbf{v}$	mass-averaged velocity of the polymer solution
$\mathbf{v}^p$	polymer velocity field
$\mathbf{v}^s$	solvent velocity field
$\mathrm{wt}/\mathrm{wt}\%$	Mass fraction
μ	initial polymer concentration in the solution
Ω	flow domain
ϕ	color function representing the distribution of the phases
ρ	total mass density of the polymeric solution
ρ_p	polymer mass density
ρ_s	solvent mass density
τ'	a relaxation time

τ'' a relaxation time

τ_{xy} shear stress

Θ liquid volume fraction

$\tilde{a}$ dimensionless ramp rate of the rheometer

$\tilde{P}_{\mathrm{x}}$ dimensionless pressure gradient

$\tilde{Q}$ dimensionless volumetric flow rate

$\tilde{\psi}_R$ vortex intensity

$\tilde{\xi}$ boundary layer constant

$B_{\alpha\beta}$ second-order transport coefficient

c total polymer concentration in the solution

c^* overlap concentration

c^{**} crossover concentration

CR contraction ratio

D local diffusivity constant

D_{ext} extrudate width

D_{nonloc} nonlocal diffusivity constant

De Deborah number

E elasticity number

F arbitrary functional of the system variables

G_0 modulus of elasticity evaluated at the linear viscoelastic limit (plateau modulus)

H Hamiltonian

h total local free energy density

H_e total elastic potential energy of the system

H_k total kinetic energy of the system

K	Hookean spring
k_1	wave magnitude
k_2	wave number
k_B	Boltzmann constant
k_p	constant controlling the amount of wall slip of the polymer
k_s	constant controlling the amount of wall slip of the solvent
M_1	coarsest mesh
M_4	finest mesh
M_p	molecular weight of the polymer
M_s	molecular weight of the solvent
N_A	Avogadro constant
n_p	polymer number density
n_s	solvent number density
q	power-law parameter
q'	Rolie-Poly model parameter controlling the suppression of CCR with chain stretch
q^*	dimensionless curvature of the Couette flow
r^*	dimensionless location in the gap of the cylindrical Couette flow
R_g	radius of gyration
R_i	radius of the inner cylinder in the Couette flow
R_o	radius of the outer cylinder in the Couette flow
R_s	The recoverable shear property at the wall
S_r	die swell ratio
T	absolute temperature
U_{in}	inlet mean velocity

U_{out}	outlet mean velocity
V	wall velocity of the simple shear flow
V_θ	angular velocity
Wi	Weissenberg number
$Z_{\alpha\beta}$	drag coefficient tensor
H	characteristic height
S	displacement

Glossary

CCR convective constraint release.

CUBISTA convergent and universally bounded interpolation scheme for the treatment of advection.

DIC diagonal incomplete-Cholesky.

FENE-P finite extensible nonlinear elastic with Peterlin's closure.

ILU incomplete lower upper.

LDPE low-density polyethylene.

MULES Multidimensional Universal Limiter with Explicit Solution.

NMR nuclear magnetic resonance.

OCT optical coherence tomography.

PIV particle image velocimetry.

PTT Phan-Thien-Tanner.

PTV particle tracking velocimetry.

Rolie-Poly Rouse linear entangled polymers.

SANS small angle neutron scattering.

SIMPLEC Semi-Implicit Method for Pressure Linked Equations-Consistent.

UCM Upper-convected Maxwell.

VCM Vasquez-Cook-McKinley.

VOF volume of fluid.

List of Figures

List of Tables

Copyright Permissions

The source that if any figure of this thesis is adopted or modified from is included in the caption of the figure after obtaining the corresponding license. Furthermore, the content of the thesis includes the following publications:

- Hooshyar and Germann (2016), A thermodynamic study of shear banding in polymer solutions, Physics of Fluids, 28(6):063104,
  with the permission of AIP Publishing,
- Hooshyar and Germann (2017), Shear banding of semidilute polymer solutions in pressure-driven channel flow, Journal of Non-Newtonian Fluid Mechanics, 242:1-10,
  with the permission of Elsevier Ltd.,
- Hooshyar and Germann (2019a), Shear Banding in 4:1 Planar Contraction, Polymers, 11(3):417,
  with the permission of MDPI,
- Hooshyar and Germann (2019b), The investigation of shear banding polymer solutions in die extrusion geometry, Journal of Non-Newtonian Fluid Mechanics, 272,
  with the permission of Elsevier Ltd.

Bibliography

Aboubacar, M., Matallah, H., Tamaddon-Jahromi, H. R., and Webster, M. F. (2002a). Numerical prediction of extensional flows in contraction geometries: hybrid finite volume/element method. *J. Non-Newt. Fluid Mech.*, 104(2):125–164.

Aboubacar, M., Matallah, H., and Webster, M. F. (2002b). Highly elastic solutions for Oldroyd-B and Phan-Thien/Tanner fluids with a finite volume/element method: planar contraction flows. *J. Non-Newt. Fluid Mech.*, 103(1):65–103.

Achilleos, E., Georgiou, G. C., and Hatzikiriakos, S. G. (2002a). On numerical simulation of polymer extrusion instabilities. *Appl. Rheol.*, 12(2):72–104.

Achilleos, E. C., Georgiou, G., and Hatzikiriakos, S. G. (2002b). Role of processing aids in the extrusion of molten polymers. *J. Vinyl Addit. Technol.*, 8(1):7–24.

Adams, J. M., Fielding, S. M., and Olmsted, P. D. (2011). Transient shear banding in entangled polymers: A study using the Rolie-Poly model. *J. Rheol.*, 55(5):1007–1032.

Adams, J. M. and Olmsted, P. D. (2009). Nonmonotonic models are not necessary to obtain shear banding phenomena in entangled polymer solutions. *Phys. Rev. Lett.*, 102(6):067801.

Agassant, J. F., Arda, D. R., Combeaud, C., Merten, A., Muenstedt, H., Mackley, M. R., Robert, L., and Vergnes, B. (2006). Polymer processing extrusion instabilities and methods for their elimination or minimisation. *Int. Polym. Process.*, 21(3):239–255.

Aguayo, J. P., Phillips, P. M., Phillips, T. N., Tamaddon-Jahromi, H. R., Snigerev, B. A., and Webster, M. F. (2007). The numerical prediction of planar viscoelastic contraction flows using the pom–pom model and higher-order finite volume schemes. *J. Comput. Phys.*, 220(2):586–611.

Allain, C., Cloitre, M., and Perrot, P. (1997). Experimental investigation and scaling law analysis of die swell in semi-dilute polymer solutions. *J. Non-Newt. Fluid Mech.*, 73(1-2):51–66.

Alves, M. A., Oliveira, P. J., and Pinho, F. T. (2003a). Benchmark solutions for the flow of Oldroyd-B and PTT fluids in planar contractions. *J. Non-Newt. Fluid Mech.*, 110(1):45–75.

Alves, M. A., Oliveira, P. J., and Pinho, F. T. (2003c). Numerical simulation of viscoelastic contraction flows. *Comput. Fluid Solid Mech*, pages 826–829.

Alves, M. A., Oliveira, P. J., and Pinho, F. T. (2004). On the effect of contraction ratio in viscoelastic flow through abrupt contractions. *J. Non-Newt. Fluid Mech.*, 122(1):117–130.

Alves, M. A., Pinho, F. T., and Oliveira, P. J. (2001). Study of steady pipe and channel flows of a single-mode Phan-Thien–Tanner fluid. *J. Non-Newt. Fluid Mech.*, 101(1):55–76.

Apostolakis, M. V., Mavrantzas, V. G., and Beris, A. N. (2002). Stress gradient-induced migration effects in the Taylor–Couette flow of a dilute polymer solution. *J. Non-Newt. Fluid Mech.*, 102(2):409–445.

Arda, D. R. and Mackley, M. R. (2005). The effect of die exit curvature, die surface roughness and a fluoropolymer additive on sharkskin extrusion instabilities in polyethylene processing. *J. Non-Newt. Fluid Mech.*, 126(1):47–61.

Ascher, U. M. and Greif, C. (2011). *A First Course on Numerical Methods*, volume 7. Siam.

Azaiez, J., Guénette, R., and Ait-Kadi, A. (1996). Numerical simulation of viscoelastic flows through a planar contraction. *J. Non-Newt. Fluid Mech.*, 62(2-3):253–277.

Behzadfar, E., Ansari, M., Konaganti, V. K., and Hatzikiriakos, S. G. (2015). Extrudate swell of HDPE melts: I. Experimental. *J. Non-Newt. Fluid Mech.*, 225:86–93.

Beris, A. N. and Edwards, B. J. (1994). Thermodynamics of flowing systems with internal microstructure, volume 36 of Oxford Engineering Science Series.

Berret, J. F., Roux, D. C., Porte, G., and Lindner, P. (1994). Shear-induced isotropic-to-nematic phase transition in equilibrium polymers. *EPL-Europhys. Lett.*, 25(7):521.

Bertola, V. (2013). Dynamic wetting of dilute polymer solutions: the case of impacting droplets. *Adv. Colloid Interface Sci.*, 193:1–11.

Bishko, G. B., Harlen, O. G., McLeish, T. C. B., and Nicholson, T. M. (1999). Numerical simulation of the transient flow of branched polymer melts through a planar contraction using the 'Pom–Pom' model. *J. Non-Newt. Fluid Mech.*, 82(2):255–273.

Bitsanis, I. and Hadziioannou, G. (1990). Molecular dynamics simulations of the structure and dynamics of confined polymer melts. *J. Chem. Phys.*, 92(6):3827–3847.

Boger, D. V., Hur, D. U., and Binnington, R. J. (1986). Further observations of elastic effects in tubular entry flows. *J. Non-Newt. Fluid Mech.*, 20:31–49.

Bollhöfer, M. and Saad, Y. (2006). Multilevel preconditioners constructed from inverse-based ILUs. *SIAM J. Sci. Comput.*, 27(5):1627–1650.

Bollhöfer, M., Saad, Y., and Schenk, O. (2008). ILUPACK-Preconditioning Software Package, Release 2.2, 2008. `http://www-public.tu-bs.de/bolle/ilupack/`.

Boukany, P. E., Wang, S., Ravindranath, S., and Lee, L. J. (2015). Shear banding in entangled polymers in the micron scale gap: a confocal-rheoscopic study. *Soft Matter*, 11(41):8058–8068.

Boukany, P. E. and Wang, S. Q. (2009b). Shear banding or not in entangled DNA solutions depending on the level of entanglement. *J. Rheol.*, 53(1):73–83.

Britton, M. M. and Callaghan, P. T. (1997). Two-phase shear band structures at uniform stress. *Phys. Rev. Lett.*, 78(26):4930.

Burghelea, T. I., Griess, H. J., and Münstedt, H. (2010). Comparative investigations of surface instabilities ("sharkskin") of a linear and a long-chain branched polyethylene. *J. Non-Newt. Fluid Mech.*, 165(19):1093–1104.

Bush, M. B., Milthorpe, J. F., and Tanner, R. I. (1984). Finite element and boundary element methods for extrusion computations. *J. Non-Newt. Fluid Mech.*, 16(1-2):37–51.

Callaghan, P. T. and Gil, A. M. (2000). Rheo-NMR of semidilute polyacrylamide in water. *Macromolecules*, 33(11):4116–4124.

Cao, Y., Yang, W. J., Guo, X. W., Xu, X. H., Chen, J., Yang, X. J., and Yuan, X. F. (2015). Role of nonmonotonic constitutive curves in extrusion instabilities. *Int. J. Polym. Sci.*

Chang, R. Y. and Yang, W. L. (1994). Numerical simulation of non-isothermal extrudate swell at high extrusion rates. *J. Non-Newt. Fluid Mech.*, 51(1):1–19.

Cheng, S. and Wang, S. (2012). Is shear banding a metastable property of well-entangled polymer solutions? *J. Rheol.*, 56(6):1413–1428.

Clarke, N. and McLeish, T. C. B. (1998). Shear flow effects on phase separation of entangled polymer blends. *Phys. Rev. E.*, 57(4):R3731.

Clermont, J. and Normandin, M. (1993). Numerical simulation of extrudate swell for Oldroyd-B fluids using the stream-tube analysis and a streamline approximation. *J. Non-Newt. Fluid Mech.*, 50(2-3):193–215.

Comminal, R., Pimenta, F., Hattel, J. H., Alves, M. A., and Spangenberg, J. (2018). Numerical simulation of the planar extrudate swell of pseudoplastic and viscoelastic fluids with the streamfunction and the VOF methods. *J. Non-Newt. Fluid Mech.*, 252:1–18.

Crochet, M. J. and Keunings, R. (1980). Die swell of a Maxwell fluid: numerical prediction. *J. Non-Newt. Fluid Mech.*, 7(2-3):199–212.

Crochet, M. J. and Keunings, R. (1982). Finite element analysis of die swell of a highly elastic fluid. *J. Non-Newt. Fluid Mech.*, 10(3-4):339–356.

Cromer, M., Cook, L. P., and McKinley, G. H. (2011a). Interfacial instability of pressure-driven channel flow for a two-species model of entangled wormlike micellar solutions. *J. Non-Newt. Fluid Mech.*, 166(11):566–577.

Cromer, M., Cook, L. P., and McKinley, G. H. (2011b). Pressure-driven flow of wormlike micellar solutions in rectilinear microchannels. *J. Non-Newt. Fluid Mech.*, 166(3):180–193.

Cromer, M., Fredrickson, G. H., and Leal, L. G. (2014). A study of shear banding in polymer solutions. *Phys. Fluids.*, 26(6):063101.

Cromer, M., Villet, M. C., Fredrickson, G. H., and Leal, L. G. (2013a). Shear banding in polymer solutions. *Phys. Fluids.*, 25(5):051703.

Cromer, M., Villet, M. C., Fredrickson, G. H., Leal, L. G., Stepanyan, R., and Bulters, M. J. H. (2013b). Concentration fluctuations in polymer solutions under extensional flow. *J. Rheol.*, 57(4):1211–1235.

Cruz, D. O. A., Pinho, F. T., and Oliveira, P. J. (2005). Analytical solutions for fully developed laminar flow of some viscoelastic liquids with a Newtonian solvent contribution. *J. Non-Newt. Fluid Mech.*, 132(1):28–35.

Daprà, I. and Scarpi, G. (2015). Analytical solution for a Couette flow of a Giesekus fluid in a concentric annulus. *J. Non.-Newt. Fluid Mech.*, 223:221–227.

De Gennes, P. G. (1971). Reptation of a polymer chain in the presence of fixed obstacles. *J. Chem. Phys.*, 55(2):572–579.

De Gennes, P. G. (1979). *Scaling Concepts in Polymer Physics*. Cornell university press.

De Ryck, A. and Quéré, D. (1998). Fluid coating from a polymer solution. *Langmuir*, 14(7):1911–1914.

Degré, G., Joseph, P., Tabeling, P., Lerouge, S., Cloitre, M., and Ajdari, A. (2006). Rheology of complex fluids by particle image velocimetry in microchannels. *Appl. Phys. Lett.*, 89(2):024104.

Denn, M. M. (2001). Extrusion instabilities and wall slip. *Ann. Rev. Fluid Mech.*, 33(1):265–287.

Deshpande, S. S., Anumolu, L., and Trujillo, M. F. (2012). Evaluating the performance of the two-phase flow solver interfoam. *Comput. Sci. Discov.*, 5(1):014016.

Dhont, J. K. G. and Briels, W. J. (2008). Gradient and vorticity banding. *Rheol. Acta*, 47(3):257–281.

Dill, K. A. and Zimm, B. H. (1979). A rheological separator for very large DNA molecules. *Nucleic Acids Res.*, 7(3):735–749.

Divoux, T., Fardin, M. A., Manneville, S., and Lerouge, S. (2016). Shear banding of complex fluids. *Ann. Rev. Fluid Mech.*, 48:81–103.

Doi, M. and Edwards, S. F. (1988). *The theory of polymer dynamics*, volume 73. oxford university press.

Doi, M. and Onuki, A. (1992). Dynamic coupling between stress and composition in polymer solutions and blends. *Journal de Physique II*, 2(8):1631–1656.

Duarte, A. S. R., Miranda, A. I. P., and Oliveira, P. J. (2008). Numerical and analytical modeling of unsteady viscoelastic flows: The start-up and pulsating test case problems. *J. Non-Newt. Fluid Mech.*, 154(2):153–169.

El Kissi, N., Leger, L., Piau, J. M., and Mezghani, A. (1994). Effect of surface properties on polymer melt slip and extrusion defects. *J. Non-Newt. Fluid Mech.*, 52(2):249–261.

El Kissi, N., Piau, J.-M., and Toussaint, F. (1997). Sharkskin and cracking of polymer melt extrudates. *J. Non-Newt. Fluid Mech.*, 68(2-3):271–290.

Evans, R. E. and Walters, K. (1986). Flow characteristics associated with abrupt changes in geometry in the case of highly elastic liquids. *J. Non-Newt. Fluid Mech.*, 20:11–29.

Evans, R. E. and Walters, K. (1989). Further remarks on the lip-vortex mechanism of vortex enhancement in planar-contraction flows. *J. Non-Newt. Fluid Mech.*, 32(1):95–105.

Favero, J. L., Secchi, A. R., Cardozo, N. S. M., and Jasak, H. (2010). Viscoelastic flow analysis using the software OpenFOAM and differential constitutive equations. *J. Non-Newt. Fluid Mech.*, 165(23-24):1625–1636.

Ferrás, L. L., Afonso, A. M., Alves, M. A., Nóbrega, J. M., Carneiro, O. S., and Pinho, F. T. (2014). Slip flows of Newtonian and viscoelastic fluids in a 4: 1 contraction. *J. Non-Newt. Fluid Mech.*, 214:28–37.

Ferrás, L. L., Nóbrega, J. M., and Pinho, F. T. (2012). Analytical solutions for channel flows of Phan-Thien–Tanner and Giesekus fluids under slip. *J. Non-Newt. Fluid Mech.*, 171:97–105.

Fielding, S. M. (2007). Complex dynamics of shear banded flows. *Soft Matter*, 3(10):1262–1279.

Fielding, S. M. and Olmsted, P. D. (2003a). Early stage kinetics in a unified model of shear-induced demixing and mechanical shear banding instabilities. *Phys. Rev. Lett.*, 90(22):224501.

Fielding, S. M. and Olmsted, P. D. (2003b). Flow phase diagrams for concentration-coupled shear banding. *Eur. Phys. J. E.*, 11(1):65–83.

Fielding, S. M. and Wilson, H. J. (2010). Shear banding and interfacial instability in planar Poiseuille flow. *J. Non-Newt. Fluid Mech.*, 165(5):196–202.

Fitzgibbon, D. R. and McCullough, R. L. (1989). Influence of a neutral surface on polymer molecules in the vicinity of the surface. *J. Polym. Sci. Part B: Polym. Phys.*, 27(3):655–671.

Frank, M., Anderson, D., Weeks, E. R., and Morris, J. F. (2003). Particle migration in pressure-driven flow of a Brownian suspension. *J. Fluid Mech.*, 493:363–378.

Germann, N. (2019). Shear banding in semidilute entangled polymer solutions. *Curr. Opin. Colloid Interface Sci.*, 39:1 – 10.

Germann, N., Cook, L. P., and Beris, A. N. (2013). Nonequilibrium thermodynamic modeling of the structure and rheology of concentrated wormlike micellar solutions. *J. Non-Newt. Fluid Mech.*, 196:51–57.

Germann, N., Cook, L. P., and Beris, A. N. (2014). Investigation of the inhomogeneous shear flow of a wormlike micellar solution using a thermodynamically consistent model. *J. Non-Newt. Fluid Mech.*, 207:21–31.

Germann, N., Cook, L. P., and Beris, A. N. (2016). A differential velocities-based study of diffusion effects in shear-banding micellar solutions. *J. Non-Newt. Fluid Mech.*, 232:43–54.

Germann, N., Dressler, M., and Windhab, E. J. (2011). Numerical solution of an extended White–Metzner model for eccentric Taylor–Couette flow. *J. Comp. Phys.*, 230(21):7853–7866.

Ghanta, V. G., Riise, B. L., and Denn, M. M. (1999). Disappearance of extrusion instabilities in brass capillary dies. *J. Rheol.*, 43(2):435–442.

Giesekus, H. (1982). A simple constitutive equation for polymer fluids based on the concept of deformation-dependent tensorial mobility. *J. Non-Newt. Fluid Mech.*, 11(1-2):69–109.

Gordon, R. J. and Schowalter, W. R. (1972). Anisotropic fluid theory: a different approach to the dumbbell theory of dilute polymer solutions. *Trans. Soc. Rheol.*, 16(1):79–97.

Goudoulas, T. B. and Germann, N. (2018). Concentration effect on the nonlinear measures of dense polyethylene oxide solutions under large amplitude oscillatory shear. *J. Rheol.*, 62(5):1299–1317.

Goudoulas, T. B., Pan, S., and Germann, N. (2017). Nonlinearities and shear banding instability of polyacrylamide solutions under large amplitude oscillatory shear. *J. Rheol.*, 61(5):1061–1083.

Goudoulas, T. B., Pan, S., and Germann, N. (2018). Double-stranded and single-stranded well-entangled DNA solutions under LAOS: A comprehensive study. *Polym. J.*, 140:240–254.

Goveas, J. L. and Fredrickson, G. H. (1999). Curvature-driven shear banding in polymer melts. *J. Rheol.*, 43(5):1261–1277.

Graham, R. S., Likhtman, A. E., McLeish, T. C. B., and Milner, S. T. (2003). Microscopic theory of linear, entangled polymer chains under rapid deformation including chain stretch and convective constraint release. *J. Rheol.*, 47(5):1171–1200.

Grmela, M., Chinesta, F., and Ammar, A. (2010). Mesoscopic tube model of fluids composed of worm-like micelles. *Rheol. Acta*, 49:495–506.

Guo, X., Zou, S., Yang, X., Yuan, X., and Wang, M. (2014). Interface instabilities and chaotic rheological responses in binary polymer mixtures under shear flow. *RSC Adv.*, 4(105):61167–61177.

Harvey, M. and Waigh, T. (2011). Optical coherence tomography velocimetry in controlled shear flow. *Phys Rev E*, 83(3):031502.

Hatzikiriakos, S. G. and Dealy, J. M. (1992). Role of slip and fracture in the oscillating flow of HDPE in a capillary. *J. Rheol.*, 36(5):845–884.

Helfand, E. and Fredrickson, G. H. (1989). Large fluctuations in polymer solutions under shear. *Phys. Rev. Lett.*, 62(21):2468.

Hemminger, O. L., Boukany, P. E., Wang, S., and Lee, L. J. (2010). Flow pattern and molecular visualization of DNA solutions through a 4:1 planar micro-contraction. *J. Non-Newt. Fluid Mech.*, 165(23):1613–1624.

Hill, D. A., Hasegawa, T., and Denn, M. M. (1990). On the apparent relation between adhesive failure and melt fracture. *J. Rheol.*, 34(6):891–918.

Holroyd, G. A. J., Martin, S. J., and Graham, R. S. (2017). Analytic solutions of the Rolie Poly model in time-dependent shear. *J. Rheol.*, 61(5):859–870.

Hooshyar, S. and Germann, N. (2016). A thermodynamic study of shear banding in polymer solutions. *Phys. Fluids.*, 28(6):063104.

Hooshyar, S. and Germann, N. (2017). Shear banding of semidilute polymer solutions in pressure-driven channel flow. *J. Non-Newt. Fluid Mech.*, 242:1–10.

Hooshyar, S. and Germann, N. (2019a). Shear Banding in 4: 1 Planar Contraction. *Polymers*, 11(3):417.

Hooshyar, S. and Germann, N. (2019b). The investigation of shear banding polymer solutions in die extrusion geometry. *J. Non-Newt. Fluid Mech.*, 272.

Hu, Y. T. and Lips, A. (2005). Kinetics and mechanism of shear banding in an entangled micellar solution. *J. Rheol.*, 49(5):1001–1027.

Ianniruberto, G., Greco, F., and Marrucci, G. (1994). The two-fluid theory of polymer migration in slit flow. *Ind. Eng. Chem. Res.*, 33(10):2404–2411.

Inn, Y. W., Fischer, R. J., and Shaw, M. T. (1998). Visual observation of development of sharkskin melt fracture in polybutadiene extrusion. *Rheol. Acta*, 37(6):573–582.

Jahromi, H. R. T. and Webster, M. F. (2011). Transient behaviour of branched polymer melts through planar abrupt and rounded contractions using pom–pom models. *Mech. Time-Depend. Mat.*, 15(2):181–211.

Jaradat, S., Harvey, M., and Waigh, T. A. (2012). Shear-banding in polyacrylamide solutions revealed via optical coherence tomography velocimetry. *Soft Matter*, 8(46):11677–11686.

Karapetsas, G. and Tsamopoulos, J. (2008). Steady extrusion of viscoelastic materials from an annular die. *J. Non-Newt. Fluid Mech.*, 154(2-3):136–152.

Kim, J. M., Kim, C., Kim, J. H., Chung, C., Ahn, K. H., and Lee, S. J. (2005). High-resolution finite element simulation of 4: 1 planar contraction flow of viscoelastic fluid. *J. Non-Newt. Fluid Mech.*, 129(1):23–37.

Kim, Y., Adams, A., Hartt, W. H., Larson, R. G., and Solomon, M. J. (2016). Transient, near-wall shear-band dynamics in channel flow of wormlike micelle solutions. *J. Non-Newt. Fluid Mech.*, 232:77–87.

Konaganti, V. K., Ansari, M., Mitsoulis, E., and Hatzikiriakos, S. G. (2015). Extrudate swell of a high-density polyethylene melt: II. Modeling using integral and differential constitutive equations. *J. Non-Newt. Fluid Mech.*, 225:94–105.

Konaganti, V. K., Ansari, M., Mitsoulis, E., and Hatzikiriakos, S. G. (2016). The effect of damping function on extrudate swell. *J. Non-Newt. Fluid Mech.*, 236:73–82.

Koopmans, R. J. and Molenaar, J. (1998). The ”sharkskin effect” in polymer extrusion. *Polym. Eng. Sci.*, 38(1):101–107.

Leonov, A. I. (1976). Nonequilibrium thermodynamics and rheology of viscoelastic polymer media. *Rheol. Acta*, 15(2):85–98.

Leygue, A., Beris, A. N., and Keunings, R. (2001). A constitutive equation for entangled linear polymers inspired by reptation theory and consistent with non-equilibrium thermodynamics. *J. Non-Newt. Fluid Mech.*, 101(1):95–111.

Li, Y., Hu, M., McKenna, G. B., Dimitriou, C. J., McKinley, G. H., Mick, R. M., Venerus, D. C., and Archer, L. A. (2013). Flow field visualization of entangled polybutadiene solutions under nonlinear viscoelastic flow conditions. *J. Rheol.*, 57(5):1411–1428.

Likhtman, A. E. and Graham, R. S. (2003). Simple constitutive equation for linear polymer melts derived from molecular theory: Rolie–Poly equation. *J. Non-Newt. Fluid Mech.*, 114(1):1–12.

MacDonald, M. J. and Muller, S. J. (1996). Experimental study of shear-induced migration of polymers in dilute solutions. *J. Rheol.*, 40(2):259–283.

Mair, R. W. and Callaghan, P. T. (1996). Observation of shear banding in worm-like micelles by NMR velocity imaging. *EPL-Europhys. Lett.*, 36(9):719.

Manneville, S. (2008). Recent experimental probes of shear banding. *Rheol. Acta*, 47(3):301–318.

Marín-Santibáñez, B. M., Pérez-González, J., De Vargas, L., Rodríguez-González, F., and Huelsz, G. (2006). Rheometry-PIV of shear-thickening wormlike micelles. *Langmuir*, 22(9):4015–4026.

Mavrantzas, V. G. and Beris, A. N. (1992). Theoretical study of wall effects on the rheology of dilute polymer solutions. *J. Rheol.*, 36(1):175–213.

Maxwell, J. C. (1867). IV. On the dynamical theory of gases. *Philos. Trans. R. Soc. Lond.*, 157:49–88.

McLeish, T. C. B. and Ball, R. C. (1986). A molecular approach to the spurt effect in polymer melt flow. *J. Poly. Sci. B Poly. Phys.*, 24(8):1735–1745.

Méndez-Sánchez, A. F., Pérez-González, J., De Vargas, L., Castrejón-Pita, J. R., Castrejón-Pita, A. A., and Huelsz, G. (2003). Particle image velocimetry of the unstable capillary flow of a micellar solution. *J. Rheol.*, 47(6):1455–1466.

Metzner, A. B., Cohen, Y., and Rangel-Nafaile, C. (1979). Inhomogeneous flows of non-Newtonian fluids: generation of spatial concentration gradients. *J. Non-Newt. Fluid Mech.*, 5:449–462.

Migler, K. B., Son, Y., Qiao, F., and Flynn, K. (2002). Extensional deformation, cohesive failure, and boundary conditions during sharkskin melt fracture. *J. Rheol.*, 46(2):383–400.

Milner, S. T. (1991). Hydrodynamics of semidilute polymer solutions. *Phys. Rev. Lett.*, 66(11):1477.

Moorcroft, R. L. and Fielding, S. M. (2013). Criteria for shear banding in time-dependent flows of complex fluids. *Phys. Rev. Lett.*, 110(8):086001.

Moorcroft, R. L. and Fielding, S. M. (2014). Shear banding in time-dependent flows of polymers and wormlike micelles. *J. Rheol.*, 58(1):103–147.

Morrison, F. A. (2001). *Understanding Rheology, Topics in Chemical Engineering*. Oxford University Press, New York.

Nghe, P., Fielding, S. M., Tabeling, P., and Ajdari, A. (2010). Interfacially driven instability in the microchannel flow of a shear-banding fluid. *Phys. Rev. Lett.*, 104(24):248303.

Nigen, S. and Walters, K. (2002). Viscoelastic contraction flows: comparison of axisymmetric and planar configurations. *J. Non-Newt. Fluid Mech.*, 102(2):343–359.

Oliveira, P. J. and Pinho, F. T. (1999). Analytical solution for fully developed channel and pipe flow of Phan-Thien–Tanner fluids. *J. Fluid Mech.*, 387:271–280.

Olmsted, P. D. (2008). Perspectives on shear banding in complex fluids. *Rheol. Acta.*, 47(3):283–300.

Olson, D. J. and Fuller, G. G. (2000). Contraction and expansion flows of langmuir monolayers. *J. Non-Newt. Fluid Mech.*, 89(1):187–207.

Olsson, F. (1994). A solver for time-dependent viscoelastic fluid flows. *J. Non-Newt. Fluid Mech.*, 51(3):309–340.

Pettas, D., Karapetsas, G., Dimakopoulos, Y., and Tsamopoulos, J. (2015). On the origin of extrusion instabilities: Linear stability analysis of the viscoelastic die swell. *J. Non-Newt. Fluid Mech.*, 224:61–77.

Peyret, R. (2002). *Spectral methods for incompressible viscous flow*, volume 148. Springer Science & Business Media.

Phan-Thien, N. (1988). Influence of wall slip on extrudate swell: a boundary element investigation. *J. Non-Newt. Fluid Mech.*, 26(3):327–340.

Pimenta, F. and Alves, M. A. (2017). Stabilization of an open-source finite-volume solver for viscoelastic fluid flows. *J. Non-Newt. Fluid Mech.*, 239:85–104.

Pimenta, F. and Alves, M. A. (2018). rheotool. `https://github.com/fppimenta/rheoTool`.

Press, W. H., Teukolsky, S. A., Vetterling, W. T., and Flannery, B. P. (1992). Numerical Recipes (Cambridge).

Purnode, B. and Crochet, M. J. (1996). Flows of polymer solutions through contractions part 1: flows of polyacrylamide solutions through planar contractions. *J. Non-Newt. Fluid Mech.*, 65(2):269–289.

Radulescu, O. and Olmsted, P. D. (2000). Matched asymptotic solutions for the steady banded flow of the diffusive Johnson–Segalman model in various geometries. *J. Non-Newt. Fluid Mech.*, 91(2):143–164.

Ramamurthy, A. V. (1986). Wall slip in viscous fluids and influence of materials of construction. *J. Rheol.*, 30(2):337–357.

Ravindranath, S. and Wang, S. Q. (2008b). Steady state measurements in stress plateau region of entangled polymer solutions: Controlled-rate and controlled-stress modes. *J. Rheol.*, 52(4):957–980.

Ravindranath, S., Wang, S. Q., Olechnowicz, M., and Quirk, R. P. (2008). Banding in simple steady shear of entangled polymer solutions. *Macromolecules*, 41(7):2663–2670.

Richardson, S. (1970). The die swell phenomenon. *Rheol. Acta*, 9(2):193–199.

Richtmyer, R. D. and Morton, K. W. (1967). Difference methods for initial value problems. *Interscience Tracts in Pure and Applied Mathematics*.

Robertson, B., Thompson, R. L., McLeish, T. C. B., and Robinson, I. (2017). Theoretical prediction and experimental measurement of isothermal extrudate swell of monodisperse and bidisperse polystyrenes. *J. Rheol.*, 61(5):931–945.

Robertson, B., Thompson, R. L., McLeish, T. C. B., and Robinson, I. (2019). Polymer extrudate-swell: From monodisperse melts to polydispersity and flow-induced reduction in monomer friction. *J. Rheol.*, 63(2):319–333.

Russo, G. and Phillips, T. N. (2011). Spectral element predictions of die-swell for Oldroyd-B fluids. *Comput. Fluids*, 43(1):107–118.

Salipante, P. F., Little, C. A. E., and Hudson, S. D. (2017). Jetting of a shear banding fluid in rectangular ducts. *Phys. Rev. Fluids*, 2(3):033302.

Schleiniger, G. and Weinacht, R. J. (1991). Steady poiseuille flows for a Giesekus fluid. *J. Non.-Newt. Fluid Mech.*, 40(1):79–102.

Schmitt, V., Lequeux, F., Pousse, A., and Roux, D. (1994). Flow behavior and shear induced transition near an isotropic/nematic transition in equilibrium polymers. *Langmuir*, 10(3):955–961.

Schroeder, C. (2017). Single polymer dynamics in semi-dilute unentangled and entangled solutions: from molecular conformation to normal stress. In *APS Meeting Abstracts*.

Sornberger, G., Quantin, J. C., Fajolle, R., Vergnes, B., and Agassant, J. F. (1987). Experimental study of the sharkskin defect in linear low density polyethylene. *J. Non-Newt. Fluid Mech.*, 23:123–135.

Tanner, R. I. (1970). A theory of die-swell. *J. Polym. Sci. Pol. Phys.*, 8(12):2067–2078.

Tanner, R. I. (1980). The swelling of plane extrudates at low Weissenberg numbers. *J. Non-Newt. Fluid Mech.*, 7(2-3):265–267.

Tapadia, P., Ravindranath, S., and Wang, S. (2006). Banding in entangled polymer fluids under oscillatory shearing. *Phys. Rev. Lett.*, 96(19):196001.

Teraoka, I. (2002). *Polymer solutions: an introduction to physical properties*. John Wiley & Sons.

Thompson, R. L., Mendes, P. R. S., and Naccache, M. F. (1999). A new constitutive equation and its performance in contraction flows. *J. Non-Newt. Fluid Mech.*, 86(3):375–388.

van Egmond, J. W. and Fuller, G. G. (1993). Concentration fluctuation enhancement in polymer solutions by extensional flow. *Macromolecules*, 26(26):7182–7188.

Van Os, R. G. M. and Phillips, T. N. (2004). Spectral element methods for transient viscoelastic flow problems. *J. Comp. Phys.*, 201(1):286–314.

Van Schaftingen, J. J. and Crochet, M. J. (1985). Analytical and numerical solution of the Poiseuille flow of a Johnson-Segalman fluid. *J. Non-Newt. Fluid Mech.*, 18(3):335–351.

Vasquez, P. A., McKinley, G. H., and Cook, L. P. (2007). A network scission model for wormlike micellar solutions: I. Model formulation and viscometric flow predictions. *J. Non.-Newt. Fluid Mech.*, 144(2–3):122 –139.

Venet, C. and Vergnes, B. (2000). Stress distribution around capillary die exit: an interpretation of the onset of sharkskin defect. *J. Non-Newt. Fluid Mech.*, 93(1):117–132.

Vergnes, B. (2015). Extrusion defects and flow instabilities of molten polymers. *Int. Polym. Process.*, 30(1):3–28.

Voigt, R. G., Gottlieb, D., and Hussaini, M. Y. (1994). Spectral Methods for Partial Differential Equations. 1984. *SIAM, Philadelphia*.

Walters, K. and Webster, M. F. (2002). Contraction flows of Highly-Elastic Liquids: Experiment and Simulation. *Comput. Sci. Rep. Ser.*, page 6.

Wang, S. (2018). *Nonlinear Polymer Rheology: Macroscopic Phenomenology and Molecular Foundation*. John Wiley & Sons.

Wang, S., Ravindranath, S., and Boukany, P. E. (2011). Homogeneous shear, wall slip, and shear banding of entangled polymeric liquids in simple-shear rheometry: A roadmap of nonlinear rheology. *Macromolecules*, 44(2):183–190.

Wang, S. Q., Ravindranath, S., Boukany, P., Olechnowicz, M., Quirk, R. P., Halasa, A., and Mays, J. (2006). Nonquiescent relaxation in entangled polymer liquids after step shear. *Phys. Rev. Lett.*, 97(18):187801.

Waters, N. D. and King, M. J. (1970). Unsteady flow of an elastico-viscous liquid. *Rheol. Acta*, 9(3):345–355.

Wesson, R. D. and Papanastasiou, T. C. (1988). Flow singularity and slip velocity in plane extrudate swell computations. *J. Non-Newt. Fluid Mech.*, 26(3):277–295.

White, S. A. and Baird, D. G. (1986). The importance of extensional flow properties on planar entry flow patterns of polymer melts. *J. Non-Newt. Fluid Mech.*, 20:93–101.

White, S. A. and Baird, D. G. (1988a). Flow visualization and birefringence studies on planar entry flow behavior of polymer melts. *J. Non-Newt. Fluid Mech.*, 29:245–267.

White, S. A. and Baird, D. G. (1988b). Numerical simulation studies of the planar entry flow of polymer melts. *J. Non-Newt. Fluid Mech.*, 30(1):47–71.

Xue, S. C., Tanner, R. I., and Phan-Thien, N. (2004). Numerical modelling of transient viscoelastic flows. *J. Non-Newt. Fluid Mech.*, 123(1):33–58.

Yamamoto, T., Hashimoto, T., and Yamashita, A. (2008). Flow analysis for wormlike micellar solutions in an axisymmetric capillary channel. *Rheol. Acta*, 47(9):963–974.

Yoo, J. Y. and Choi, H. C. (1989). On the steady simple shear flows of the one-mode Giesekus fluid. *Rheol. Acta*, 28(1):13–24.

Zettl, U., Hoffmann, S. T., Koberling, F., Krausch, G., Enderlein, J., Harnau, L., and Ballauff, M. (2009). Self-diffusion and cooperative diffusion in semidilute polymer solutions as measured by fluorescence correlation spectroscopy. *Macromolecules*, 42(24):9537–9547.

Zhou, L., Cook, L. P., and McKinley, G. H. (2010). Probing shear-banding transitions of the VCM model for entangled wormlike micellar solutions using large amplitude oscillatory shear (LAOS) deformations. *J. Non-Newt. Fluid Mech.*, 165(21):1462–1472.

Zhou, L., Cook, L. P., and McKinley, G. H. (2012). Multiple shear-banding transitions for a model of wormlike micellar solutions. *SIAM Appl. Math.*, 72(4):1192–1212.

Zhou, L., Vasquez, P. A., Cook, L. P., and McKinley, G. H. (2008). Modeling the inhomogeneous response and formation of shear bands in steady and transient flows of entangled liquids. *J. Rheol.*, 52(2):591–623.

Declaration

I hereby declare that this Ph.D. thesis has been composed solely by myself. The contents of this dissertation are my own work, otherwise, the corresponding reference is cited or acknowledged. This work is original and has not been submitted for any other degree or to any other university.

Soroush Hooshyar